UNIVERSITY OF SOUTHAMPTON

Two dimensional materials synthesis for electronic and optoelectronic applications

by

Nikolaos Aspiotis

Thesis submitted for the degree of Doctor of Philosophy

in the

Faculty of Engineering and Physical Sciences

Optoelectronics Research Centre

November 2019

1

Declaration of Authorship

I, Nikolaos Aspiotis, declare that this thesis titled, 'Two dimensional materials synthesis for electronic and optoelectronic applications' and the work presented in it are my own. I confirm that:

- This work was done wholly or mainly while in candidature for a research degree at this University.
- Where any part of this thesis has previously been submitted for a degree or any other qualification at this University or any other institution, this has been clearly stated.
- Where I have consulted the published work of others, this is always clearly attributed.
- Where I have quoted from the work of others, the source is always given. With the exception of such quotations, this thesis is entirely my own work.
- I have acknowledged all main sources of help.
- Where the thesis is based on work done by myself jointly with others, I have made clear exactly what was done by others and what I have contributed myself.
- Parts of this work have been published as shown in Appendix B.

Signed: _____

Date: _____

UNIVERSITY OF SOUTHAMPTON

Abstract

Faculty of Engineering and Physical Sciences
Optoelectronics Research Centre

Doctor of Philosophy

by Nikolaos Aspiotis

Atomically thin materials offer unique optical, electronic and physical properties due to quantum confinement effects. Graphene has been the material that has primed the extensive research interest in the field. The lack of an energy bandgap in graphene helped to expand the research of 2D materials beyond graphene, in search for application tailored properties. The strongest overall candidate for electronic applications has since been Transition Metal Dichalcogenides (TMDCs). The metal-chalcogen bonds are strong covalent bonds that form stacked layers together by weak Van der Waals forces and can hence be easily separated to form individual layers. The significance of this ability lies in the fact that although TMDCs have an indirect bandgap in their bulk form, they transition to a direct bandgap in single layer form. This property is important for optoelectronic applications as it results in an enhanced photoluminescence quantum yield. A monolayer of such a material offers very high effective mobility that would otherwise require three times thicker single crystal silicon layer to reach. Transistors made of TMDCs have also been shown to reach the thermal transport limit achieving a subthreshold swing of as low as 60 mV/dec and on/off ratios of 10^8. Those attributes make TMDCs an ideal candidate for next generation electronic and optoelectronic applications potentially replacing current material technologies. Due to the weak Van der Waals forces between layers one of the first methods explored to obtain single layers of graphene and TMDCs has been exfoliation and transfer techniques involving tape, chemical or mechanical methods. Those techniques

have been providing very high quality single crystal layers with excellent electronic and optoelectronic properties. A direct drawback of these methods is the lack of scalability. For this reason, there has been a collective research effort in the community towards the development of direct growth methods for TMDCs that are scalable and can be used in traditional top-down fabrication processes. Scalable techniques have recently included RF sputtering, CVD and ALD techniques that use solid, metal halide or organic precursors. Most of those studies rely on the transfer of the TMDC after it has been grown in order to form electronic devices such as field effect transistors. The main reason for this is that during the growth process the dielectric integrity of the underlying SiO_2, on which the films are commonly grown, is compromised. This work aims to tackle the scalability of 2D materials by devising methods directly applicable to wafer scale production. In particular, for TMDCs a combination of Atomic Layer deposition and Thermal reaction is used to form a few layer MoS2 on a SiO_2 substrate without the need for transfer to perform as an FET device. Using ALD, a thin layer of MoO3 is first formed on the SiO_2 and then annealed in a CVD reactor in presence of $H2_S$. As the wafers are already coated with MoO_3 during the high temperature anneal in H_2S the SiO_2 quality is preserved removing the need to transfer to a fresh substrate and therefore enabling the practical upscale of the technology. This thesis discusses the methods developed by the author for growing 2D films of graphene, MoS_2 and HfS_2. The results from the characterization of the films at a variety of growing conditions provide a comprehensive guide to optimizing the film growth for optoelectronic and electronic applications. Moreover new fabrication protocols have been designed in order to accommodate the fragile nature of 2D materials while making high performance devices.This work provides an array of devices as performance demonstrators such as FET, fiber modulator, mechanochromic metamaterial and graphene photodetector. The most significant achievement of this work is the design of the full fabrication protocol for high performance FET devices and the resulting performance of these devices. It was demonstrated that a subthreshold slope of under 180 mV/dec and an on/off ratio of more than 10^4 can be achieved with directly grown transistors in a readily scalable process.

Acknowledgements

First of all I would like to thank my supervisor Dan Hewak for giving me the opportunity to work on an exciting project and for his continuous support throughout the course of this PhD, making it as smooth as possible. I am thankful that I was given the opportunity to be a part of a leading group in Chalcogenide materials. I would also like to thank Dr. Kevin Chung-Che Huang for introducing me to the CVD experimental procedures by sharing his knowledge and technical know how. Finally I would like to thank Dr Ioannis Zeimpekis for the numerous technical and scientific skills I have acquired working under his guidance which without, this work would not have been possible. I thank for the technical support Neil Sessions, as well as the Novel glass Group technicians Christopher Craig and Ed Weatherby for giving a positive tone in the novel glass cleanroom environment. I would like to thank Dr Pier Sazio and Dr Sakelaris Mailis for sharing their ideas and knowledge, it was a pleasure. I feel obliged to thank a couple of the new friends I' ve made during my PhD studies. Dr Ioannis Katis thank you for all the help and company. Dr Maria Papaioannou, thank you for the numerous phone calls that remained unanswered and not giving up on me. I would like to thank and express my gratitude to my family for their support throughout my life who never stopped giving or caring. Last but not least, my greatest thank you goes to Cleopatra for always being there, her unconditional love and her profound tenacity.

Contents

List of Figures

List of Tables

Abbreviations

2D	Two dimensional
ALD	Atomic Layer Deposition
ANOVA	Analysis of Variance
APCVD	Atmospheric Pressure Chemical Vapor Deposition
Ar	Argon
Au	Gold
CBM	Conduction Band Minimum
CH_4	Methane
Cu	Copper
CVD	Chemical Vapour Deposition
DOE	Design of Experiments
DUV	Deep ultraviolet
EBL	Electron Beam Lithography
EC	Ethylene carbonate
EUV	Extreme Ultraviolet
$FeCl_3$	Iron(III) chloride
FEM	Finite Element Method
FET	Field Effect Transistor
FIB	Focused Ion Beam
FWHM	Full Width Half Maximum
Ge	Germanium
H_2	Hydrogen
HF	Hydrogen Fluoride
$HfCl_4$	Hafnium tetrachloride

HfS_2	Hafnium disulfide
HOPG	Highly Oriented Pyrolytic Graphite
LPCVD	Low Pressure Chemical Vapour Deposition
MoO_3	Molybdenum Trioxide
MoS_2	Molybdenum disuldide
MOSFET	Metal Oxide Semiconductor Field-Effect Transistor
N_2	Nitrogen
NbS_2	Niobium disulfide
Ni	Nickel
NMP	N-Methyl-2-pyrrolidone
Pd	Palladium
PS	Polystyrene
PTAS	Perylene-3,4,9,10-Tetracarboxylic Acid Tetrapotassium Salt
PTCDA	Perylene-Tetracarboxylic Dianhydride
rGO	Reduced Graphene Oxide
RIE	Reactive Ion Etching
sccm	Standard Cubic Centimeters per Minute
Si	Silicon
SiC	Silicon Crabide
SiO_2	Silicon Dioxide
SS	Subthreshold Slope
STM	Scanning Tunneling Microscope
TaS_2	Tantalum disulfide
TMDC	Transition Metal Dichalcogenide
TVS	Thermal Vapour Sulfurization
UHV	Ultra High Vacuum
UV	Ultraviolet
VBM	Valence Band Maximum
WS_2	Tungsten disulfide
XPS	X-ray Photoelectron Spectroscopy
$ZrSe_2$	Zirconium diselenide

Chapter 1

Introduction

1.1 History of semiconductor technology

The idea of the field effect transistor was conceived and patented by E. Lilienfeld in 1930 by presenting schematics of a three electrode structure for controlling electric currents although no device was presented [1]. The first transistors fabricated were developed in late 1947 by Bell labs and William Shockley. This was a semiconductor amplifier based on n − type Germanium that was contacted by two gold contacts named base and emitter, when voltage was applied on the base the current flowing through the emitter was modulated with an amplified output signal [2]. For the next ten years research was focused on achieving higher purity, uniform semiconductor materials and advancing doping techniques. In late 50's Germanium was replaced by Silicon because Ge was exhibiting currents at the off state (leakage current) which was increasing the total power consumed by the device. The first FET device was fabricated by Bell labs in 1963 almost 40 years after the Lilienfeld patent. The architecture of the device was a sandwich structure using silicon as the semiconducting material a thermally grown silicon dioxide layer and a metal on top of the oxide the well known today metal − oxide − semiconductor (MOS). Since then silicon is the key material for electronic devices as it offers high performance, it is relatively cost effective and offers a high

level of integration constituting silicon based metal oxide semiconductor field effect transistors (MOSFETs) as the main building block of most integrated electronics.

The down scaling of silicon transistors to achieve a higher level of integration follows Moores law which states that the number of transistors on a chip is doubling approximately once every 2 years, this has recently become a technological challenge due to physical limitations of the material itself and of the MOSFET fabrication process. We are now at the 7nm node and the prediction is that by 2020 we will be at the 5 nm node [3]. At these sizes the channel lengths of the transistors are just a few atoms giving rise to short channel effects reducing their reliability and performance. It is therefore apparent that to keep up with the increasing demand for higher performance logic and memory an improvement of the physical properties is required. A change of material is therefore imminent. The new materials are required to demonstrate properties such as higher carrier mobilities, high thermal conductivity without increasing cost.

1.2 The rise of two dimensional materials

The realization of two dimensional materials was predicted by Landau not to be viable due to thermodynamical instability that would lead to segregation of islands or total decomposition.[4] That was until 2004 when the first two dimensional material, graphene, was isolated by Novoselov and Geim by using the scotch tape exfoliating technique[5]. This led to a boom of new two dimensional materials such as TMDCs and a plethora of new applications driven by the properties of these materials [6]. Graphene drew the attention because of its intrinsic properties such as high carrier mobility up to 20000 $cm^2 \cdot V^{-1} \cdot s^{-1}$ an ambipolar nature and a remarkable absorption of broadband light for a 2D thick material that is 2.3 %, saturable absorption at low light intensities that also can be tuned by applying a gate voltage, making graphene a candidate material as a future optical element for the generation of ultrashort laser pulses etc.[5] Altough graphene exhibits a remarkable mobility which is esential for logic operation it also exhibits an inherent

drawback. As it is a semimetal it has no energy band gap making it challenging to fabricate switching devices such as FETs. There has been a series of studies where the engineering of a bandgap was explored but as this is not an inherent property of the material and is challenging to achieve its implementation in logic chips is hindered. Fortunately, the solution to the bandgap issue came with another member of the 2D family, TMDCs. TMDCs at their bulk form are indirect semiconductors that when scaled down to 2D crystals due to quantum confinement they exhibit a direct band gap that can be tunable, according to the number of their layers [6]. FET TMDCs have been fabricated exhibiting large mobilities high $on-off$ ratios and close to excite $sub-threshold$ slopes (SS), these properties are constituting TMDCs promising materials for field effect transistors. Furthermore TMDCs having a large variety of bandgaps affected by their number of layers and elemental composition within the visible electromagnetic spectrum has made them candidates for a number of optoelectronic applications such as phototransistors, photodiodes flexible electronics and biosensors all of which can be integrated to already existing optoelectronic and electronic technologies [7].

1.3 Synopsis

2D materials is a very young research topic offering the attraction and excitement of the new to any material scientist. They have immensely interesting physics to explore and engineering hurdles to solve. The real challenge after their isolation from their bulk counterparts lies into chemically synthesizing not just as small experimental samples, but in large scales while preserving the characteristics of their ore forms. This is so that they can be assimilated into commercial processes that could disrupt the semiconductor industry. This is the challenge, motivation and goal of this work. To develop reliable protocols for growing wafer scale two dimensional materials with electrical and optical performance as close as possible to their single crystal form. To achieve this goal this study concentrated in the fundamentals of material composition and their growth using chemical vapor deposition, atomic layer deposition and thermal vapour sulfurization techniques.

The development of reliable protocols for growing wafer scale two − dimensional materials through chemical vapor deposition (CVD) techniques and atomic layered deposition for electronic and optoelectronic applications was the main motivation of this research work. The first part of this thesis which includes Chapters 2 and 3, presents the physical properties of graphene and MoS_2 including its different crystal structures its Raman characteristics and electron transport properties. Chapter 3 presents the main routes of isolating 2D materials via different methods that have been presented in the literature including the chemical exfoliation of MoS_2 flakes to its growth in larger scales and transfer to fresh substrates for fabrication of functional devices. Following, the basic growth techniques for graphene are presented, namely the epitaxial growth and CVD growth. A closer examination of the graphene CVD parameters is presented in order to use this knowledge for the experimental chemical vapor depositing of graphene. Finally the devices from the aforementioned growth techniques for MoS_2 and graphene are presented and compared. Chapter 4 presents the experimental growth of graphene by employing low pressure chemical vapor deposition (LPCVD) and the Raman characteristics of the different protocols used. The deposition of the TMDC HfS_2 is also presented by using HfCl4 as the hafnium precursor by LPCVD using H_2S as the sulphurizing agent followed by the characterization of the films grown. Finally the growth of wafer scale MoS_2 by sulphurization of atomic layer deposited MoO_3 in H_2S enviroment is presented. A design of experiments of the sulphurization process was used in order to grow wafer scale MoS_2 in order to have a first insight of the sulphurizing process. Chapter 5 presents the protocols developed for fabricating the grown materials into field effect transistors and hetero - structures. Finally the DC characteristics of as grown MoS_2 bottom gated and ionic liquid top gated FETs are presented. Chapter 6 contains collaborative work with Dr Artemios Karvounis on the direct CVD growth of MoO_3-MoS_2 stack on a metamaterial surface towards mechanochromic devices. Finally Appendix A presents two different works I was a part of, resulting to a fiber modulator and a photodetector employing wafer scale CVD grown graphene.

Chapter 2

Physical properties of 2D materials

2.1 Introduction

Two dimensional materials such as graphene and TMDCs present a plethora of physical properties that arise from their crystal and electron configurations. In this chapter we are underlining the basic properties of graphene and an insight on its Raman properties. A short introduction to the TMDC family is presented followed by the basic physical characteristics of MoS_2, including the evolution of its band structure from bulk to monolayer, the different crystal structures that can be obtained, the Raman fingerprint and finally its limitations presented through its electron transfer properties.

2.2 Graphene properties

Carbon atoms contain six electrons in an $(1s)^2(2s)^2(2p)^2$ electronic configuration. Although carbon has just two unpaired electrons in the outer shell (2p) in the ground state, it can form bonds with more than two atoms. Due to the small energy difference between 2s and 2p it is easy for an electron in the 2s state to appear in

2p and therefore it is possible to create hybrid orbital between the two states (sp2 hybrization). Figure 2.1 gives a spatial 3D representation where the carbon atoms are connected through sp2 hybrization resulting from the combination of one s - orbital with two p - orbitals, with three other carbon atoms in a 120 degree angle configuration forming a honeycomb crystal structure with two carbon atoms in each unit cell.One s orbital in combination with 2p orbitals of an atom combine to a planar assembly with 120 degree angle between hybrid orbitals forming a σ bond. The length of these bonds is 1.42 Angstroms and they are responsible for the mechanical properties of graphene. The remaining electron is in a p orbital state in the perpendicular direction of the sp2 and forms a π bond with adjacent p - orbitals. This combination of pi orbitals creates a huge orbital which allows the easy movement of electrons across the plane of graphene and therefore giving it its exceptional conductivity.

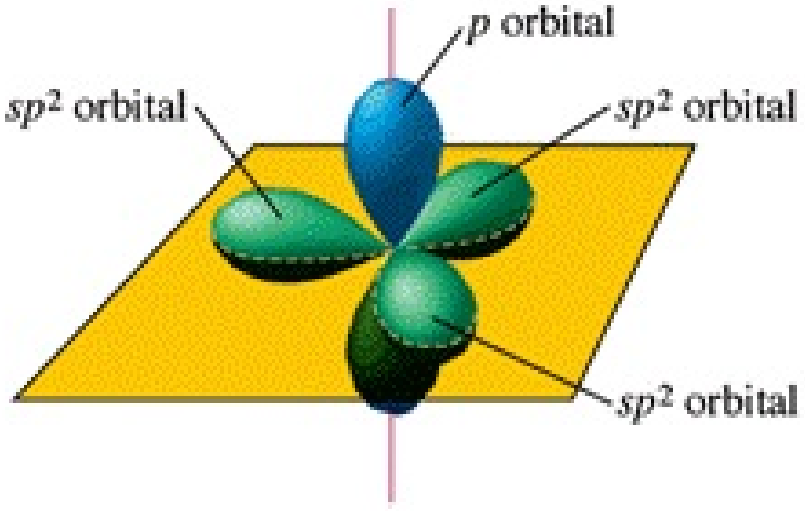

FIGURE 2.1: Graphene orbitals [8].

Graphene is a zero band gap semiconductor (otherwise known as a semimetal) where the top energy of the valence band is the same as the bottom energy of the conduction band. This point is where the Fermi level lies. An electric potential can be used to move the Fermi level to higher or lower energies, which explains graphene's ambipolar behaviour in the presence of an electric field. This behaviour is governed by the Dirac equation [9]. The charge carriers can therefore be tuned

between electrons and holes in concentrations as high as cm^2 and their mobilities can exceed 15,000 $cm^2 \cdot V^{-1} \cdot s^{-1}$, by applying an electric field. The electric field is effectively changing the Fermi level inducing holes or electrons[10]. Figure 2.2 is a representation of the position of the Fermi level of a graphene layer when applying different gate voltages. The rapid decrease of resistivity is apparent when positive or negative gate voltage is applied, which is a result of the high carrier mobility. For negative gate voltages the Fermi level lies within the valence band of the energy spectrum and therefore holes are the majority carrier, while for the positive gate voltages Fermi level shifts to the conduction band where electrons are the majority carriers. When no gating is applied the Fermi level rests at the Dirac point where the valence and conduction bands meet exhibiting its higher resistivity. Graphene can therefore be tuned to be an excellent conductor.

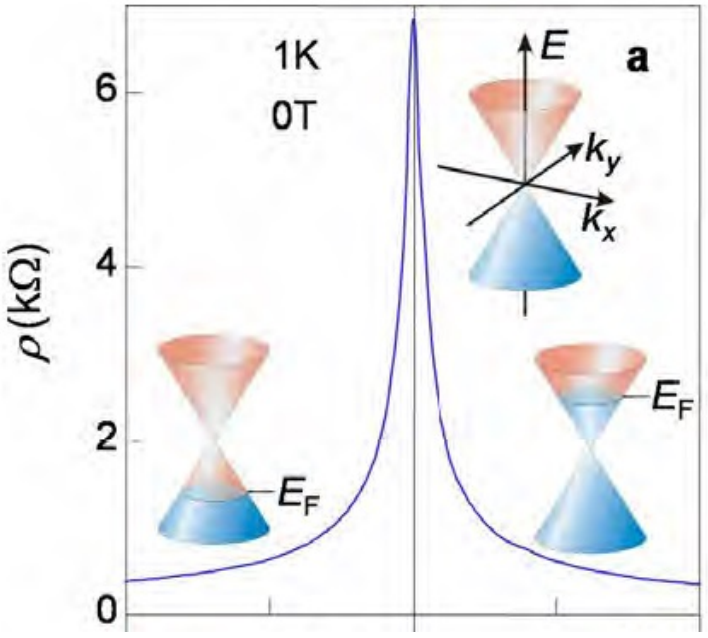

FIGURE 2.2: Graphene ambipolar effect, positive gating induces electron and negative induces holes [11].

Graphene being a semimetal exhibits no energy bandgap and therefore it cannot be used as a semiconductor in its standard form. Nevertheless engineering of a band gap can be achieved in two ways. The first way to open a bandgap is by stacking two layers of graphene with Bernal stacking orientation in which where half of the

carbon atoms of the upper layer are located in the empty centers of the first layer graphene hexagons and applying a double electric field. The stacked graphene layers exhibit two parallel conduction bands above the two valence bands where the lowest conduction band and the highest valence band are in touch resulting in a zero bandgap. When a top and a bottom gating field is applied two effects are induced. First the difference of the fields cause a shift of the Fermi level resulting to a carrier doping and second the average of the two fields applied that lead to the breaking of the bilayer inversion symmetry leading to the opening of a bandgap of 250 meV [12] [13]. Figure 2.3 repsesents the bangap opening in bilayer graphene. The second route is by fabricating graphene nanoribbons in which case the lateral confinement of the charge carriers leads to a bangap opening. With this method nanoribbons down to 15 nm widths have been fabricated exhibiting a band gap opening of approximately 200 meV [14]. The on - off ratios achieved by this method are very poor restricting the use of graphene as a field effect transistor. The fabrication of such structures leads to unwanted and unpredictable effects due to the existence of armchair and zigzag edge states, with the armchair configuration exhibiting semiconducting properties while the zigzag present a metallic nature. This mixture of states is leading to areas that are becoming semiconducting and others staying metallic. These mixed states are connected in series and it has been shown that the transport characteristics are dominated by the semiconducting segments of the nanoribbons.[15] .

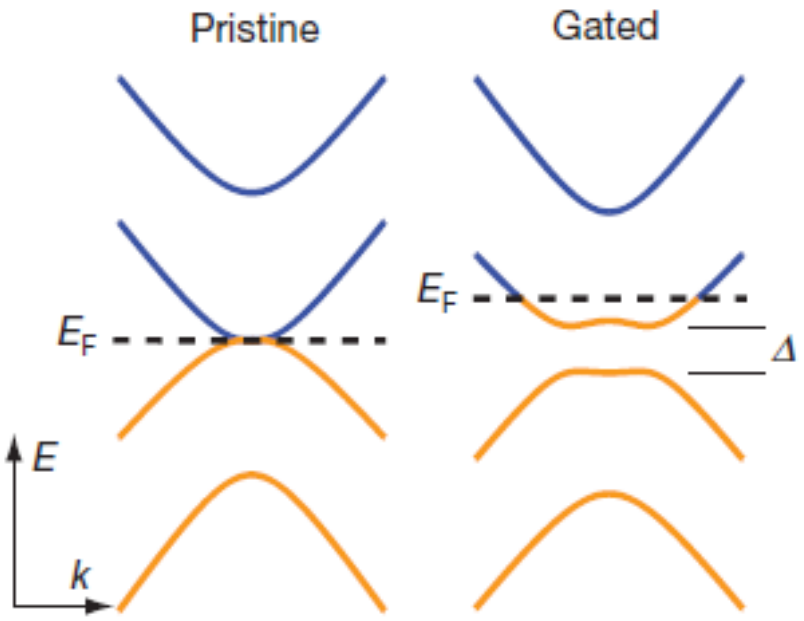

FIGURE 2.3: Representation of the bandgap opening in bilayer graphene [15].

2.2.1 The Raman signature of graphene

Raman spectroscopy is a method where laser irradiation is shone on the material to be characterized, then the scattered light by the material is measured. The incident light interacts with the vibrations in the material and the scattered light returned to the sensor. Figure 2.4 gives an energy representation of the two main scattering mechanisms in Raman spectroscopy. Most of the light is an elastical scattering result of Rayleigh scattering where incident photons excite an electron in the ground state to a virtual state and falls back to its original energy state radiating scattered light with the same energy as the excitation photons. Raman scattering is classified into two inelastic scattering processes, Stokes Raman scattering and anti-Stokes Raman scattering. In Stokes Raman scattering the scattered light has less energy (longer wavelength) than the incident light since the excited electron falls back to a vibrational state rather than its ground state. In the case of anti - Stokes scattering an electron is excited from a vibrational state and falls back to the ground state resulting in scattered light with higher energy (shorter

wavelength) from the incident photons. Wavelengths that are very close to the initial wavelength of the laser are filtered out, as they are likely just reflections off of the material.

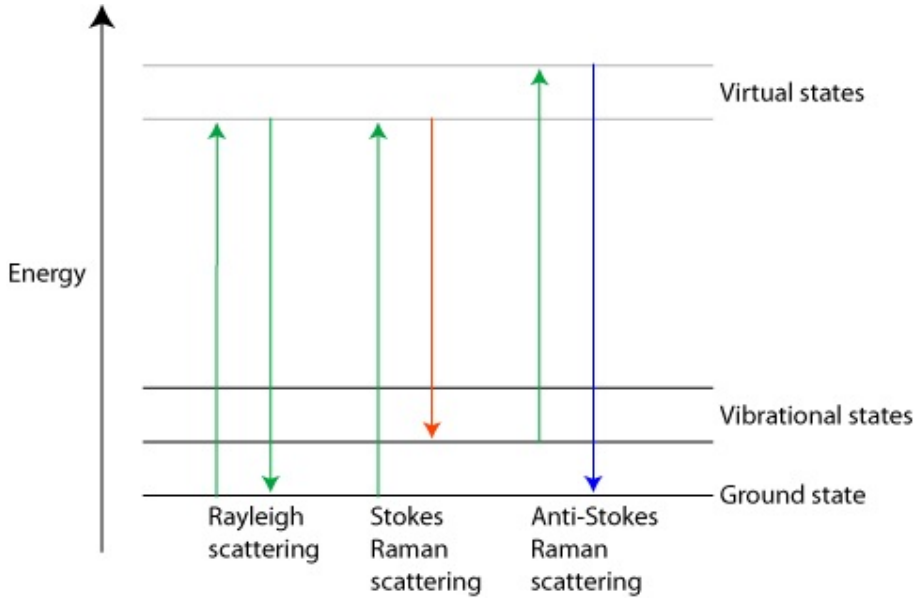

FIGURE 2.4: Raman excitations.

One of the challenges with graphene is observing its actual successful formation and determining its quality. Raman spectroscopy is an effective technique that can provide information in a nondestructive manner about the number of layers the density of defects and the presence of doping. Figure 2.5 depicts the Stokes phonon energy shift caused by laser excitation,two main peaks are present in the Raman spectrum: G (1580 cm^{-1}), a primary in plane vibrational E_2g phonon mode at the Brillouin zone centre , and 2D (2690 cm^{-1}), a second order overtone of a different in plane vibration. D (1350 cm^{-1}) is a third peak resulting from the breathing modes of the six atom rings and it comes from transverse optical (TO) phonons around the K or K' points in the first Brillouin zone. The D and 2D peak positions are dispersive (laser excitation energy dependent) [16].

Figure 2.6 shows that as the number of graphene layers increases from one layer to bulk, because of added forces from the interactions between layers, the spectrum changes from that of a single layer graphene, to one giving a wider, shorter and higher frequency peak. The G peak also experiences a smaller red shift from

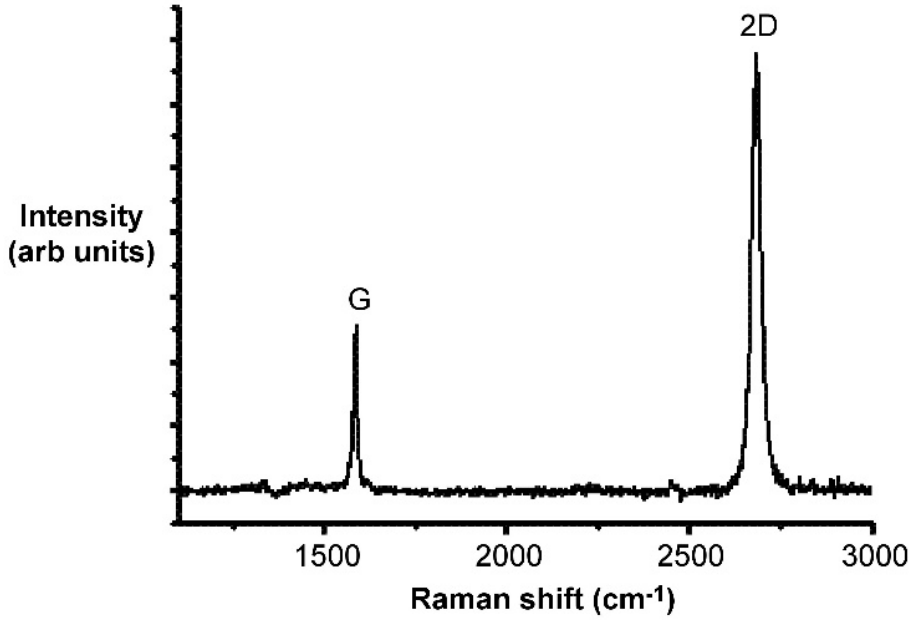

FIGURE 2.5: Typical monolayer exfoliated graphene Raman spectrum [16].

increased number of layers. In that way, the number of layers can be derived from the peak intensity ratio I2D/IG, as well as the position and shape of these peaks. For one layer graphene experiments have shown that this intensity ratio must be at least two. Doping in graphene is known to shift the Fermi level from the Dirac point, decreasing the probability of excited charge carrier recombination. This reduced recombination sharpens the G peak, decreasing its FWHM. Doping graphene also decreases the intensity of the 2D peak [17] [18]. Besides the thickness and doping of graphene the Raman modes can be used in order to extract information on the quality of the graphene sheet by quantifying the amount of defects through the analysis of the D and G peaks. For large perturbations the peak intensity ratio of these peaks (ID/IG) has been shown to provide good quantification of the crystal disorder while for small ones the frequency integrated intensity ratio has been used[19].

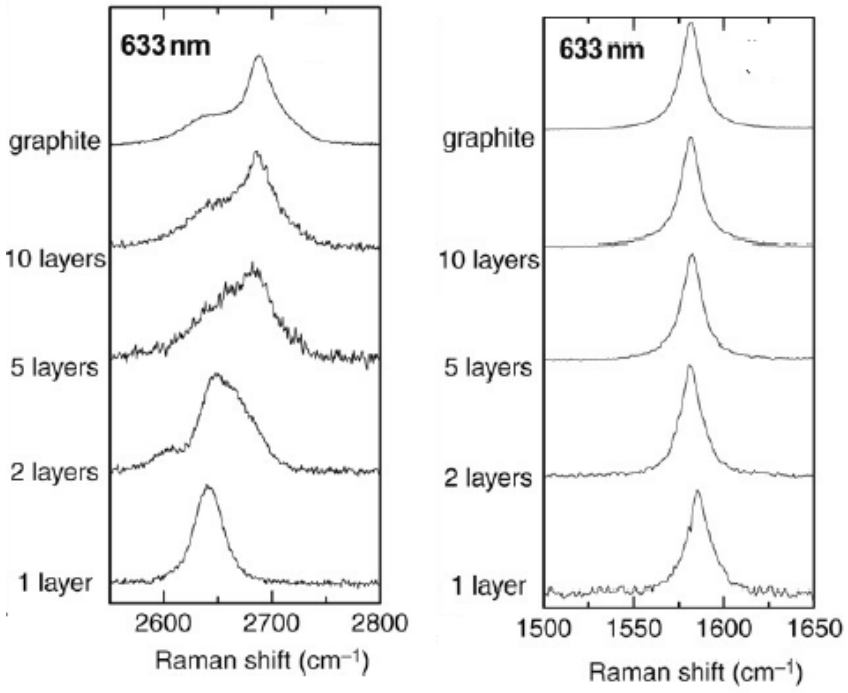

FIGURE 2.6: The evolution of graphene Raman peaks [16].

2.3 Transition metal dichalcogenides

TMDCs are binary compounds with the generalized formula of MX_2 where M is a trantition metal from the groups IV, V, VI, VII, IX and X is an element of group 16, namely a chalcogen connected to the metal. Figure 2.7 is a representation of the TMDCs on the periodic table with some of the transition metals being partially coloured indicating that not all dichalcogenides can form layered structures. TMDCs consist of two planes of hexagonally arranged chalcogen atoms (S, Se, Te) linked to a hexagonal plane of transition metal atoms via covalent bonds while in their bulk form each layer is held together by weak van der Waals forces. This lack of out of plane bonds results in a material capable of ideal interfaces.

The lack of out of plane bonds and weak interlayer bonding has been utilized over the years in lubrication technology because of the low friction and unreactive nature of bulk molybdenite and now is exploited in order to isolate monoatomic sheets of this family of materials. TMDCs exhibit a wide range of physical properties that

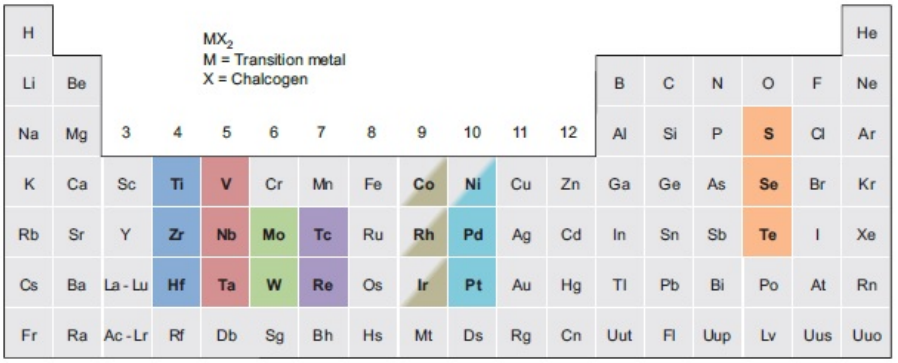

FIGURE 2.7: The possible combinations of Transtion metal dichalcogenides [20].

differ for different element combinations. These include semiconductors as MoS_2, metals as NbS_2,semimetals as $TiSe_2$ and superconductors as TaS_2 [21][22][23].

2.3.1 The MoS_2 case

MoS_2 in its bulk form is an indirect semiconductor with a bandgap of 1.2 eV. In its two dimensional form with the one layer thickness at 0.65 nm, perpendicular quantum confinement arises restricting the carrier movement in only two dimensions leading to a substantially different band structure from that of the bulk state, corresponding to a wider bandgap of 1.8 eV. This bandgap transition is depicted in figure 2.8 where it can be observed that the indirect band gap consists of a valence band maximum (VBM) at the γ - point and a conduction band minimum (CBM) at a midpoint along γ - K symmetry lines. When the number of layers is reduced to one atomic layer, the VBM and the CBM move toward the K-point and a direct band gap is obtained [24]. This direct electronic structure results in an enhancement of the photoluminescence quantum yield that is not existent for the thicker counterparts. Figure 2.8(b) shows typical photoluminesence of MoS_2 upon excitation with 532 nm laser irradiation where two strong resonances emerge at 677nm and 627 nm, these resonances are denoted as A1 and B1 excitons and are the direct excitonic transitions at the Brillouin zone K point between the split valence band maxima and the conduction band minimum.[25] [26]

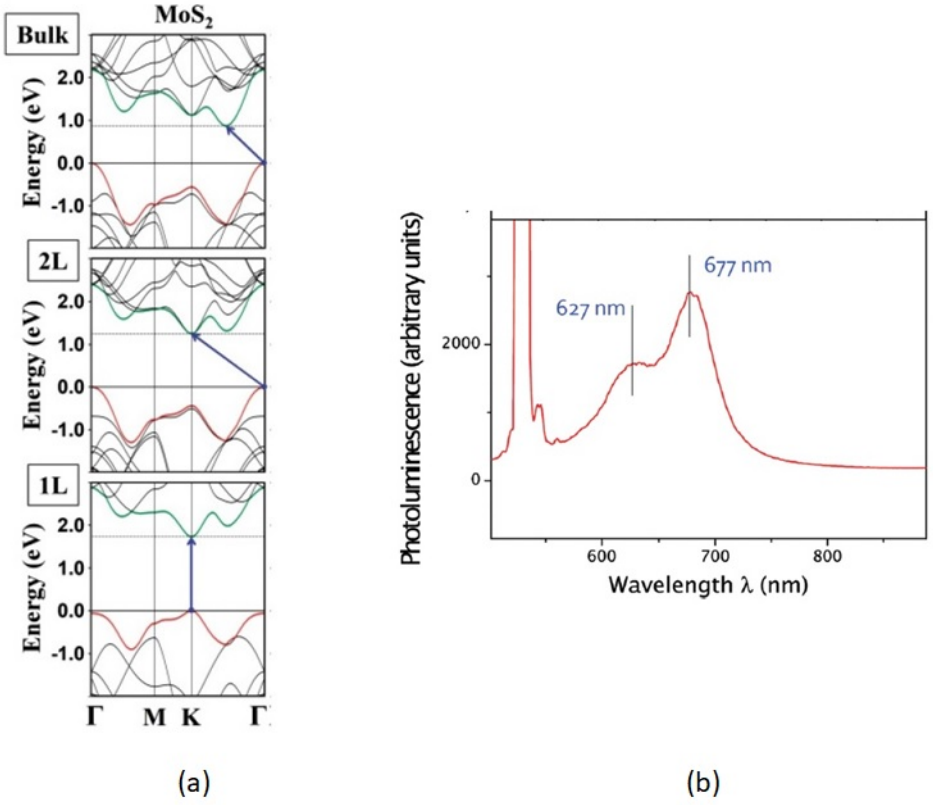

FIGURE 2.8: a)The band structure of MoS_2 from bulk to monolayer b)Excitonic transitions of monolayer MoS_2 [24][25].

2.3.1.1 The MoS_2 crystal

Dickinson and Pauling were the first to report on the crystal structure of MoS_2 in 1923 by characterizing the material with XRD. These were the first experiments confirming the hexagonal lattice of the material. It was found that each molybdenum atom is surrounded by six sulphur atoms that are located at the corners of a small triangular prism.[27]

MoS_2 being a layered material where each layer comprises a monolayer sheet of molybdenum atoms sandwiched between two layers of sulphur atoms. This results in a layer thickness of 6.5 Angstroms that is the sum of the Van der Waals gap and the sulphur - molybdenum - sulphur covalent bond thickness, can have multiple stacking orders of its layers resulting in differentiated polymorphs. Single layer MoS_2 exists in two types of polymorphs, the trigonal prism (1H-MoS_2) and the octahedral coordination (1T-MoS_2). Although the crystal structure of each layer

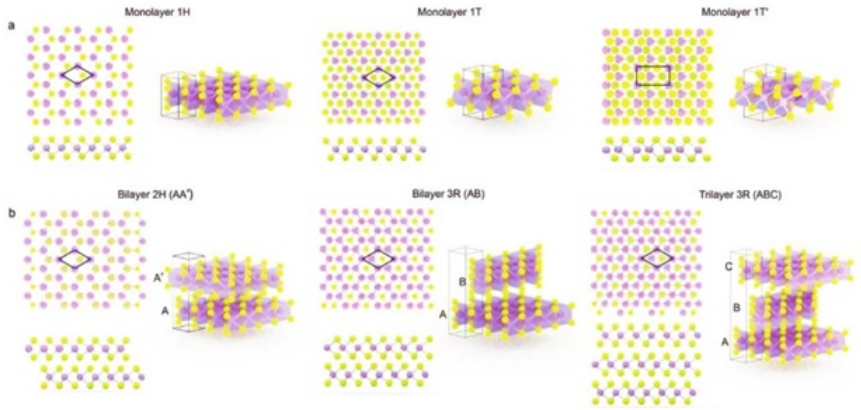

FIGURE 2.9: The various polymorphs of MoS_2 a)Monolayer 1H, 1T, 1T' b)bilayer 2H, 3R and trilayer 3R- stacking [28].

is identical for few layer MoS_2 the 1H stacking results into the hexagonal 2H and the rhombohedral 3R polymorphs where more than one layer is present. Each of these polytypes are presenting unique properties. Most studies are focused on 2H and 1T polymorphs since 2H is an intrinsic indirect semiconductor and natural occurring, while 1T being metastable with a metallic nature that can be synthesized by intercalating 2H sheets with lithium ions that cause the gliding of one of the sulphur planes resulting in the 1T - phase. The different polymorphs of MoS_2 are shown in 2.9 while their different properties are shown in 2.10.

Polytype	Space group	Stacking order	Lattice parameters	Properties and remarks
1T	*P3m1*	AbC	a = 5.60 Å and c = 5.99 Å (ref. 37)	Paramagnetic. Metallic. Metastable structure (spontaneous distortion forms superstructures)
2H	$P6_3/mmc$	AbA BaB	a = 3.15 Å and c = 12.30 Å (ref. 35)	Diamagnetic. Indirect band dap semiconductor (1.29 eV). The most abundant polytype in the Earth's crust
3R	*R3m*	AbA BcB CaC	a = 3.17 Å and c = 18.38 Å (ref. 36)	Diamagnetic. Indirect bandgap semiconductor (*ca.* 1.29 eV). Its properties are similar to those of the 2H polytype (ref. 57)

FIGURE 2.10: The different properties of MoS_2 polytypes [29].

2.3.1.2 MoS_2 Raman fingerprint

The Raman spectrum of bulk MoS_2 exhibits four modes that can be seen in figure 2.11, an in plane optical vibration of the rigid atomic bond, denoted as E^2_2g, an in plane optical vibration of S atoms denoted as E_1g , E^1_2g an inplane optical vibration of the Mo+S atoms in the basal plane and A_{1g} an out of plane optical vibration of S atoms along the c axis [30].

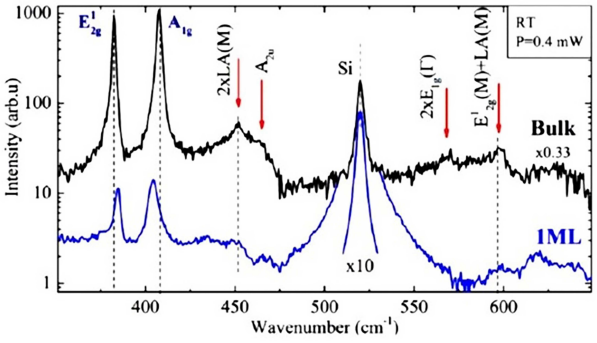

FIGURE 2.11: Raman modes of bulk MoS_2 under 532nm laser excitation [30].

Upon thinning this spectrum changes substantially as it reaches monolayer thickness. The energy difference between the Raman frequencies of E_2g and A_1g peaks, varies monotonously with the layer number of ultrathin MoS_2 and can therefore be used as a reliable method to identify the number of layers. When the layer number increases, the interlayer Van der Waals force in MoS_2 suppresses atom vibration, resulting in higher force constants. This should lead to a blue shift for both E_{2g} and A_{1g} modes. This blue shift of the A_1g peak with increasing layer number is consistent with the predicted stiffening. On the contrary, E_{2g} peak exhibits a red shift, instead of a blueshift, suggesting that increased interlayer Van der Waals force plays a minor role, while stacking induced structure changes or long range Coulombic interlayer interactions in multilayer MoS_2 may dominate the change of atomic vibration.[31]. Furthermore the full width at half maximum (FWHM) of the in plane vibrational mode E_2g can be used as an reliable indication of lattice

distortions and overall crystalline quality of the film, the smallest FWHM of the E_{2g} Raman mode appears with a monolayer single crystal at 3.7cm^1 [32][33]. Figure 2.12 typical Raman spectra for different number of layers for exfoliated MoS_2 excited by a a 532 nm laser where the A_{1g} and E_{2g} blue and red shifts can be clearly observed. Figure 2.13 lists the peak frequencies for different thicknesses and different laser excitations.

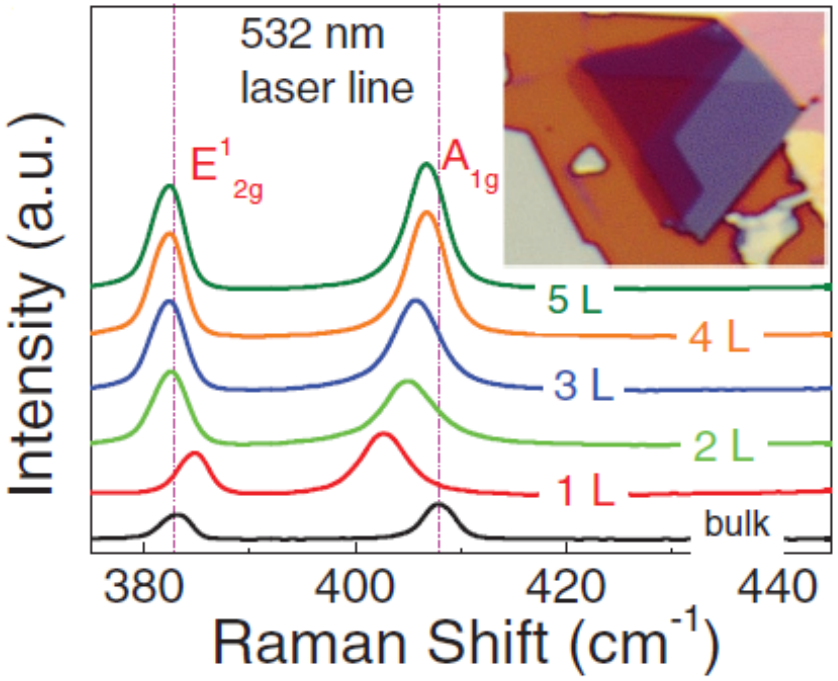

FIGURE 2.12: MoS_2 A_{1g} and E_{2g} Raman modes for different numner of layers under 532nm laser excitation [34].

Laser lines [nm]	E^1_{2g} peak frequency [cm^{-1}]					A_{1g} peak frequency [cm^{-1}]				
	1 L	2 L	3 L	4 L	bulk	1 L	2 L	3 L	4 L	bulk
325	384.2	382.8	382.8	382.7	382.5	404.9	405.5	406.3	407	407.8
488	384.7	383.3	383.2	382.9	383	402.8	405.5	406.5	407.4	408
514.5[15]	384.3	383.2	382.7	382.3	382	403	404.8	405.8	406.7	407.5
532	384.7	382.5	382.4	382.4	383	402.7	404.9	405.7	406.7	407.8
632.8	385	383.8	383.3	382.9	381.5	403.8	404.8	405	406	406.6

FIGURE 2.13: Evolution of Raman peaks in MoS_2 and the Raman peaks for different number of layers for different excitation energies [34].

2.3.1.3 The MoS_2 XPS signature

X - Ray photoelectron spectroscopy (XPS) is the most widely used method for analyzing the surface of solid samples. Its operation is based on the photoelectric effect that was first described by A. Einstein. A typical XPS spectrometer is presented in the following figure and as it can be seen it's consisted by three elements a light source, an electron energy analyzer and an electron detector.

The light sources are usually Mg or Al cathode X - Ray tubes providing X - ray radiation with energy of a few thousand eV. Upon radiation with this energy of a solid sample the electrons of the inner core shells of the material are excited and emitted. Although the high energy X - Rays can penetrate the film the first 3 nm - 4nm of the material's electrons are excited. The number of the electrons emitted and their kinetic energy can by quantified upon detection but most importantly the binding energy of the emitted electrons being sensitive to their chemical environment results in shifts of the binding energy that are called chemical shifts and can be employed to obtain information on the chemical status of the elements present in the material. The binding energy of a core level electron can be easily calculated by the formula [35]

$$E_B = hv - E_{kin} - \Phi$$

where hv is the light source excitation energy E_{kin} the kinetic energy of the electron and Φ the work function.

XPS is a powerful technique for evaluating the stoichiometry of MoS_2 the main Mo3d peaks (IV oxidation states) $3d_{5/2}$ and $3d_{5/2}$ spin orbit peaks at binding energies of 229 eV and 232 eV respectively, with conjuction of the s2p spin orbit splited peaks S $2p_{3/2}$ and $2p_{1/2}$ at binding energies of 161.9 eV and 163 eV. Furthermore peaks at 236 eV and 234.5 eV are associated to the oxidation of molybdenum while peaks at 164.1 eV and 169 eV are elemental unbound sulphur oxidized sulphur atoms respectively. Nevertheless shifts of up to 0.8 eV to lower binding energies have been attributed to the shift of the Fermi level closer to the

valence band than to a chemical state rendering MoS_2 p type. Mcdonell et al. have come to this conclusion supported STM imaging and stoichiometry results that correlated oversulphurized MoS_2 to p type characteristics and sulphur defficient MoS_2 down to 1.8:1 to n type characteristics[36].

2.3.1.4 MoS_2 electron scattering mechanisms

The transport of carriers in single layer MoS_2 is confined in one plane. In that way the scattering and transport properties are affected by four mechanisms: i) Coulomb scattering ii) surface interface phonon scattering iii) acoustic and optical phonon scaterring and iv) roughness scattering. These mechanisms are affected by the layer thickness,effectives carrier masses, temperature, carrier density and the phonon band structure.

For two dimensional MoS_2 the Coulomb scattering mechanism increases because of the intimate proximity of the carriers and charged impurities such as chemical residues, absorbents, surface dangling bonds and crystal imperfections present in the interface between the semiconductor and the dielectric material the semiconductor is deposited or transferred to. Furthermore the carrier concentration in MoS_2 is a function of ionic impurities such as sulphur deficiencies that give rise to its intrinsic n - type nature, making the Coulombic effects even stronger and reducing the carrier mobility. For thicker films t $>$ 1L the inter-facial impurities contribute to the scattering of the carriers but the lattice phonon vibrations is the main scattering mechanism. The surface interface phonon scattering is induced by the physical roughness of the dielectric material in contact with the semiconducting material or by the ripples and wrinkles in the material itself created by the transfer methods. As shown in figure 2.14(a) at low temperatures (T = 100 K) the carrier mobility is dominated by acoustic phonon scattering, whereas at room temperatures the carriers are dominated by optical phonon scattering mechanisms.

The transition of the band gap from indirect to direct for a single layer and the shift of the band structure results in a change in the electron - phonon interactions for 2D and thicker films. Phonon - electron Coulombic and roughness suppression

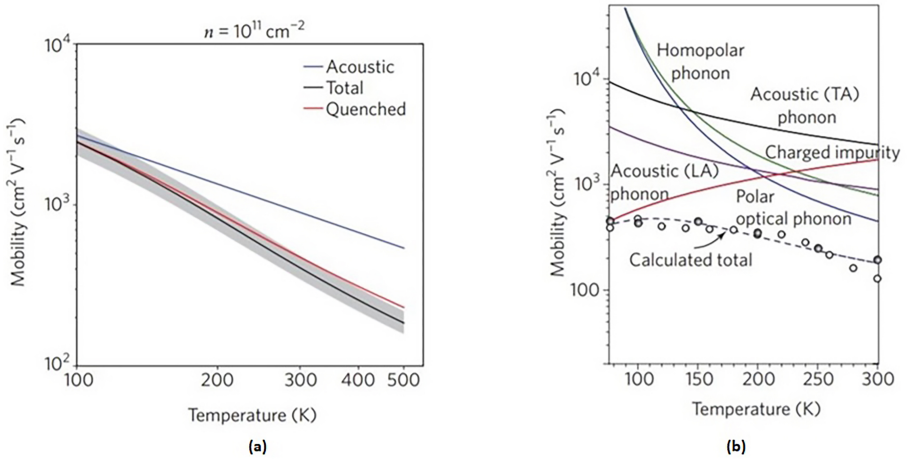

FIGURE 2.14: a) Single layer MoS_2 carrier mobility as a function of T b) carrier mobility for multilayer MoS_2 (dashed line) and the scattering mechanisms versus temperature [37][38].

can be realized by employing high k dielectric materials by substantially increasing the limited by these effects carrier mobilty. [39] [40] [38]

Chapter 3

2D materials, synthesis routes and state of the art devices

3.1 Bottom up and top down synthesis

There are two general approaches to produce ultra-thin materials (nanomaterials), top-down and bottom-up. In the bottom-up approach, nanomaterials are synthesized by the interaction of atoms or molecules through chemical reactions. The precursors (starting chemicals) used in the synthesis of materials are substances usually in liquid, vapour or gaseous form that chemically react, sublimate, evaporate or dissociate to form a material. This route produces nanomaterials with low contamination, chemical homogeneity and minimum defect sites. In the top-down approach the nanomaterial to be synthesized is isolated from the same material at its bulk form. The bulk material is broken into smaller fragments provided sufficient energy. The energy delivery can be applied by different routes. For TMDCs and graphene the most important synthesizing approach is CVD because of its high yield and scalable capabilities[41] [42].For graphene epitaxial growth on silicon carbide is an important technique for its synthesis as well but the cost is much higher than CVD because silicon carbide that is used is a high cost material and because the technique itself is power consuming [43]. On the other hand the lowest

yield and not scalable technique is micromechanical cleavage, the also known as the scotch tape technique, the technique first used to isolate a two dimensional material [10]. Table 3.1 presents categorized the basic top down and bottom up techniques for graphene synthesis.

TABLE 3.1: Top down and bottom up techniques for graphene synthesis

TOP DOWN	BOTTOM UP
Micromechanical cleavage	Chemical vapor deposition (CVD)
Thermal exfoliation and reduction	Epitaxial growth on SiC
Electrolytic exfoliation	Reduction of CO
Chemical synthesis through oxidation of graphite	Unzipping carbon nanotubes

3.2 Micromechanical cleavage

The first isolation of a 2D material, graphene, was achieved by using micromechanical cleavage of graphite. The technique as presented in figure 3.1 is as simple as repeatedly peeling graphite until a single layer is isolated. The drawback in this technique is that monolayers of graphite, graphene, are only a few micrometers wide and are amongst a haystack of numerous multilayers and graphitic flakes. Furthermore observing the monolayers on arbitrary substrates is impossible, only on a silicon wafer with specific thickness of silicon dioxide can graphene be observed due to interference contrast. Nowadays instead of plain graphite, highly oriented pyrolytic graphite (HOPG) is being used to mechanically exfoliate graphene. HOPG exfoliation results in high quality graphene samples that are used as benchmarks for graphene samples created with other techniques [10].

3.2.1 Chemical Vapour Deposition

Chemical vapor deposition is a technique used for solid thin film deposition on substrates by using vapor precursors that chemically react to produce the desired film. Typical components of a CVD system presented in figure 3.2 are a vacuum

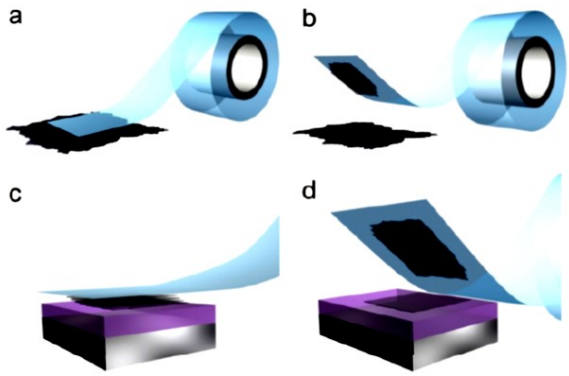

FIGURE 3.1: Representation of the micromechanical cleavage technique: aadhesive tape pressed on 2D crystal)b)the tape detaches few layer of the crystals c)the tape comes in contact with the substrate of choice d) peeling off the bottom layers are left on the substrate [44]

.

pump if the reaction is to take place in vacuum , the delivery system that is a set of mass flow controllers and valves that feed in the reaction chamber the reaction gases, where the chemical reaction in order to produce the film takes place. The gases reach the reaction chamber after the mixing unit where the gases are uniformly mixed. Finally if needed, the energy required for the reaction to take place is provided by a furnace that encloses the reaction chamber providing energy in the form of heat [41]. CVD of graphene is a low cost, scalable and high yield technique that provides control of the number of layers deposited as well as means to dope graphene by introducing the suitable gases in the reaction chamber. The main components of graphene deposition via CVD are the substrates used to promote graphene synthesis, the gases fed in the reaction chamber, the pressure used and the temperature [45] [46] [47]. This technique was employed for depositing large area single layer graphene films, in the next chapters the fundamentals of graphene CVD are being introduced.

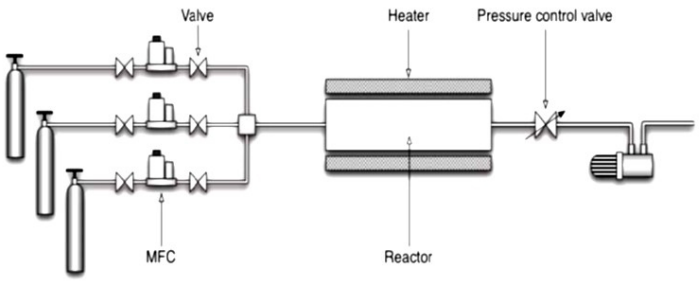

FIGURE 3.2: Typical CVD system [48]

.

3.2.1.1 Substrate effect

The right choice of substrate for graphene CVD is crucial. That is because the substrate dictates the route of the graphene formation. The first substrate that successful graphene deposition was achieved was nickel. The formation route in this case is carbon segregation. Using this route of synthesis has proven to be difficult in terms of controlling the number of layers deposited. That is because Ni has a high solubility of carbon and furthermore carbon precipitates out at the grain boundaries of polycrystalline Ni substrate resulting to more layers of graphene at the boundaries and non−homogeneous films. Copper is known to have low solubility of carbon, that is why it is more preferred for graphene CVD. Furthermore copper acts as a catalyst in order to reduce the decomposition temperature of the carbon carrier gas. Due to its low carbon solubility the formation of graphene takes place at the surface of the metal resulting to a single layer homogeneous film. Nevertheless there are drawbacks by using copper as well. The main drawback is that graphene grows in a polycrystalline way adapting the polycrystalline nature of the substrate making the film inferior compared to mechanical exfoliation [49] [50].

3.2.1.2 Gasses effect Role of Hydrogen

In order to synthesize graphene via CVD there is a need for a carbon carrier gas. Methane is commonly used as a carrier gas but surprisingly when used by itself there is no graphene deposition. The carrier gas is used synergistically with hydrogen which acts in a dual manner as well. It acts as an activator of surface−bound carbon that leads to the monolayer growth and as an etching reagent that controls the size and morphology of the resulting graphene domains. In that context we understand that hydrogen methane partial pressures can be tuned in order to achieve graphene layers with larger domains enhancing the properties of the grown graphene [46][51][52].

3.2.1.3 Pressure effect

Synthesis of graphene can be achieved either using low pressure CVD (LPCVD) or atmospheric pressure CVD (APCVD). The major difference between these two techniques is the activation energy for graphene nucleation. In LPCVD the activation energy is 4 eV while in APCVD it is 9 eV. In LPCVD the sublimation of copper leads to a lower nucleation density while in APCVD copper sublimation is suppressed leading to a higher nucleation density. Lower nucleation density results in graphene with bigger domains and better properties resembling single crystal graphene. The final difference between APCVD and LPCVD is that in the case of LPCVD the formation of graphene is self terminating, meaning that when the copper foil is covered with a monolayer it is difficult to deposit a second layer, when in APCVD the multilayer deposition is more prominent, though the effect is not fully yet understood [47][53].

3.2.1.4 Temperature effect

Graphene films can be obtained by using temperatures as low as 850 °C. Even at this temperature at low pressure there is apparent copper sublimation that acts as stated in the previous section. Below 850°C the graphene films deposited exhibit

a high level of defects that may be a result of low graphitization at these scale of temperatures. The higher the temperature used during deposition the more efficient the decomposition of the carrier gas which leads to more carbon reactive species to be deposited on the substrate. Furthermore the copper films are pre − annealed before the deposition stage in order to increase the Cu grain size and clean the surface [45][54].

Summarizing the above effects we can now describe the graphene CVD mechanism. Exposure of Cu to hydrogen in order to clean the material and enlarge its grains in order to synthesize graphene with bigger domains. Introduction of catalytic carbon carrier gas and its decomposition at high temperatures in order to form carbon reactive species. Depending on the temperature used, carrier gas pressure − flow and hydrogen partial pressure, the Cu surface is saturated under saturated, or supersaturated with carbon species. Finally the formation of nuclei takes place on the copper foil as a result of supersaturation. The nuclei growth forms graphene islands that expand until the whole substrate surface is covered.

3.2.2 Epitaxial growth on Silicon Carbide

Thermal decomposition of SiC presented in figure 3.3 is an alternative way to CVD for obtaining large area graphene sheets. The main advantage of this method is that the insulating SiC substrates can be used for fabrication of electronic devices. Epitaxial growth has been demonstrated by using UHV and atmospheric pressure processes. C. Berger etal. produced ultrathin epitaxial graphite on Si terminated (0001) face of single−crystal 6H−SiC by thermal desorption of Si. The samples were first H_2 etched, in order to remove the oxide. After the removal of the oxide samples were heated to temperatures ranging from 1250 °C to 1450 °C in UHV, under these conditions, the vapour pressure of C is orders of magnitude smaller compared to that of Si as a result desorption of Si atoms leave on the top surface of the substrate a few layer graphene film [55]. K.V. Emtsev et al. have grown graphene on Si terminated SiC by annealing at higher temperatures (1650 °C) at atmospheric pressure in Ar atmosphere. By annealing in an Ar environment at

atmospheric pressure the evaporation rate of Si is reduced and only commences at much higher temperatures than that of the UHV protocol. That high temperature resulted in an improved surface morphology of the grown film whereas the higher pressure resulted in thinner graphene films [56]. The effects of the of C terminated and Si terminated SiC have also been explored. Experiments have shown that Si terminated SiC leads to small domains up to 100 nm in diameter, whereas the C terminated SiC can grow larger domains up to 200 nm but the grown material is multilayered disordered graphene. Finally the epitaxial growth of graphene is not a self - limiting process producing inhomogeneous films making the process curently unreliable for fabrication of large scale device production [57] [58] [59]. A modified process for wafer scale of up to two layer epitaxial graphene was presented by C. Dimitrakopoulos et al. by fabricating high frequency transistors. For the growth 6H SiC wafers were used. First the wafers were cleaned from the oxide contamination by annealing at 810^0C under silane flow, subsequently an annealing step at 1140^0C and $8*10^{-7}$ Torr was employed for the surface reconstruction of the SiC wafer. Finally the wafers were annealed at 1450^0C at a pressure of $3.5*10^{-4}$ Torr for the epitaxial growth of graphene. This process flow resulted in high mobility up to 4000 $cm^2 \cdot V^{-1} \cdot s^{-1}$ and cutoff frequencies up to 100 GHZ [60].

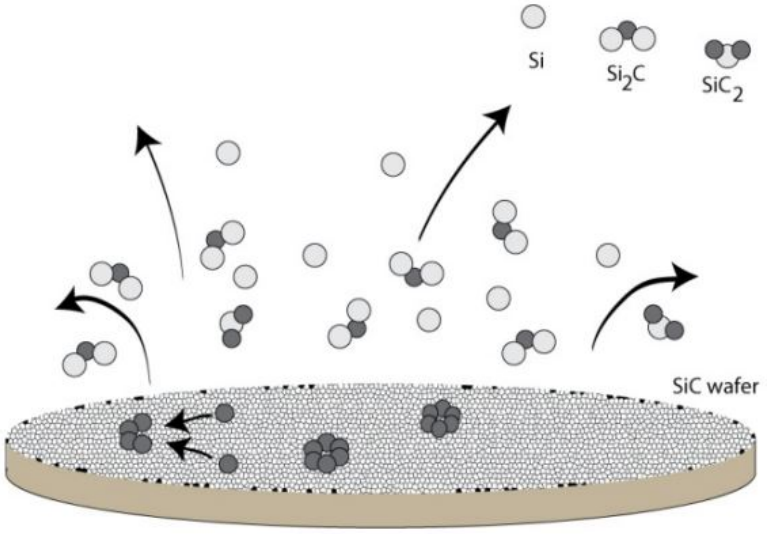

FIGURE 3.3: Epitaxial growth of graphene on SiC [61].

3.2.3 Transfer methods

After the deposition of graphene on a copper substarte the material must be transferred to the suitable substrate for further fabrication. This step is crucial because it is very easy to inflict defects to the material due to its atomic nature, by wrinkling or tearing. The basic concept for transferring 2D materials presented in figure 3.4 is using a sacrificial polymer layer. The copper substrate is spin coated with a polymer resulting in a thin sacrificial layer, then the substrate is etched in a suitable solution leaving the polymer graphene stack floating in the solution. The graphene etching treatments use iron chloride ($FeCl_3$) or ammonium persulfate ($(NH_4)_2S_2O_8$). The stack is cleaned by rinsing and then transferred to the desired substrate. Last step is the removal of the polymer by immersing it to the suitable solvent. Removal of polymer from graphene is quite challenging and residues can be removed by further annealing of the sample[62].

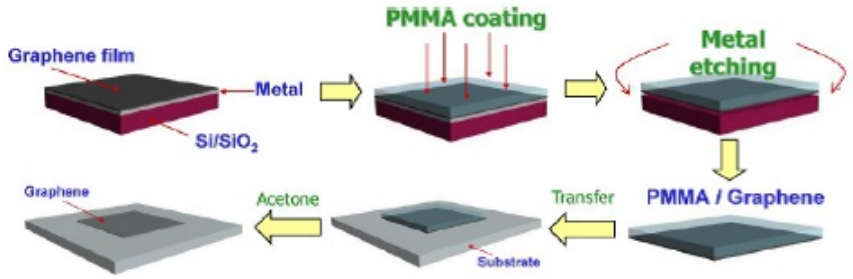

FIGURE 3.4: Etching protocol for graphene transfer [62]

.

Figure 3.5 shows a different approach of transferring that involves the electrochemical delamination of graphene instead of etching. In this technique the copper graphene sample is spin coated with a sacrificial polymer as well and then the copper is used as a cathode and a glassy carbon rod as anode. An aqueous solution of $K_2S_2O_8$ is used as an electrolyte. The Cu electrode is then polarized with DC voltage resulting to hydrogen bubbles at the graphene copper interface gently delaminating the graphene film [63].

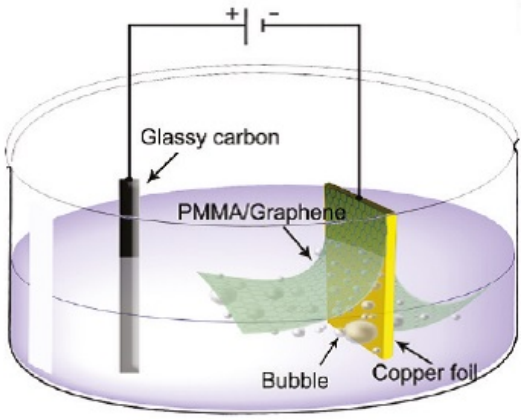

FIGURE 3.5: Electrochemical delamination of graphene [63]

.

3.3 2D MoS_2 exfoliation and synthesis routes

MoS_2 and all the TMDCs, as graphene, can be exfoliated due to the weak interlayer bonds [55] [45] and can be synthesized by various protocols from the top - down bottom - up routes. There are many techniques for the growth of single layer and multilayer films yielding different results when fabricated as electronic or photonic devices mainly because of the different stoichiometries and their deposited configuration of isolated flakes or pollycrystaline films. The most commonly used techniques of exfoliation, CVD techniques employing different precursors and thermal vapour sulphurization of molybdenum and molybdenum oxide deposited thin films will be presented. As this thesis is mainly concentrated on 2D materials for electronic applications we will compare different synthesis methods by looking at the performance of field effect transistors made by each process were these are presented.

3.3.1 Exfoliation

As in graphene single and few layer MoS_2 flakes were first isolated by mechanical exfoliation [64]. The exfoliation process is using a bulk crystal that is repeatedly peeled off by a Scotch tape until single layer thin crystals are produced. Those

crystals are typically a few tenths of micrometers wide in their lateral dimensions. Those thin cleaved crystals are subsequently brought into contact with a substrate. This is usually a Silicon substrate with a SiO_2 layer on the top surface, as it can provide the basis of a bottom - gated transistor. Typically SiO_2 thicknesses used are 100 nm and 280 nm as the red violet colours creates a sufficient optical contrast due to interference with the thin layers of MoS_2, which is imperative for locating the crystals and performing processing such as optical lithography [65]. A modified technique for exfoliating larger crystals with approximately 200 μm lateral sizes has been presented by GZ Magda et al. The exfoliated crystals, were exfoliated using a thermal release tape and first transferred onto epitaxially grown Au instead of Si/ SiO_2 in order to exploit the chemical affinity of sulphur to gold. After the transfer to the gold substrate the thermal tape was heated up and removed leaving the flakes on the gold substrate. Short ultrasonic treatment was used for detaching the top thicker flakes transferred. This technique resulted in flakes of lateral sizes up to hundreds of microns. Initially, the exfoliated flakes were transferred onto a Si/ SiO_2 substrate. To achieve this, thermal release tape was used to create a sacrificial substrate while gold was etched to release the MoS_2 flakes before transferring to the new Si /SiO_2 substrate. The AFM analysis revealed heavy contamination that was attributed to gold contamination that most probably was originated during the chemical etching step [66].

Liquid exfoliation is a solution processing approach where either the bulk material is submerged in a solvent and undergoes an ultrasound treatment exfoliating the weakly coupled layers or ion interacalation is used to decouple layers from the bulk [67] [68]. Electrochemical exfoliation was proposed by Liu et al as a method for liquid exfoliation of mono and few layer nanosheets. In this method a bulk MoS_2 is used as the anode a Pt wire as the cathode, and 0.5 M Na_2SO_2 solution is used as the electrolyte. A DC bias is applied between the anode and the cathode in order for the exfoliation to take place. The steps that are used are, firstly applying a low positive bias in order to wet the bulk MoS_2 crystal and then a higher bias voltage for approximately two hours is applied in order to exfoliate the crystal. After this process the surface of the solution is occupied by a large number of MoS_2 flakes.

Those flakes are collected by vacuum filtration and redispersed in $N-methyl-2-$ pyrrolidone in order to achieve a uniform distribution of 2D containing solution. The mechanism of electrochemical exfoliation of bulk MoS_2 crystals involves the application of a positive bias to the working electrode, in order for the oxidation of water to take place and produce OH and O radicals assembled around the bulk MoS_2 crystal. The OH and O radicals and/or anions insert themselves between the MoS_2 layers and weaken the van der Waals interactions between the layers. Second, oxidation of the radicals and/or anions leads to a release of O_2 and/or SO_2, which causes the MoS_2 interlayers to greatly expand. Finally, MoS_2 flakes are detached from the bulk MoS_2 crystal by the erupting gas and are then suspended in the solution. The surface of the bulk MoS_2 crystal is oxidized during electrochemical exfoliation, as the XPS analysis revealed with the oxide atomic percentage of the exfoliated flake at 15.6 % revealing the quality and degree of oxidation of the exfoliated MoS_2 nanosheets. This technique provides MoS_2 where 7 % is monolayer and 70 % 2 - 5 layers [69]. From figure 3.6 the different results of the techniques introduced are presented, in figure 3.6(a) the scotch tape exfoliated monolayer as seen is of a few microns size and multilayer flakes are apparent either isolated or on the monolayer flake itself. The gold mediated efoliation is presented in figure 3.6(b) where it can be seen that the monolayer is drastically bigger in size but multiple multilayer regions can be seen in the field of view of the microscope. An electrochimacally exfoliated film is presented in figure 3.6(c) via SEM imaging where the arbitrary distribution flakes is apparent.

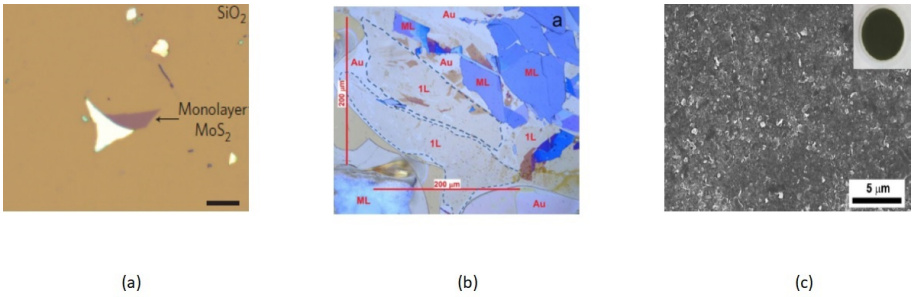

FIGURE 3.6: a) Exfoliated MoS_2 flake by Scotch tape b) chemical adhesion assisted to gold exfoliation C)SEM image ofelectrochemically exfoliated thin film [70] [66] [69]

3.3.2 CVD of MoS_2

The chemical vapour deposition technique has been employed for the synthesis of MoS_2 as well. There are two main approaches, that both use precursors in vapour or gaseous form. The first method is based on the use of two precursors,a solid precursor that contains Mo and the second precursor that is either sulfur at a high temperature for achieving sufficient vapour pressure or H_2S gas. The second method starts with Mo or MoO_3 in a solid form either already deposited on a wafer or melted in a crucible. The sulphurization sources are as the first method. The first one is using precursors in gaseous forms that are reacting in the gaseous form and precipitating and the second one is employing a deposited transition metal or transition metal oxide film that is subsequently inserted into a CVD chamber for the sulphurization process. The later techniques is mentioned as thermal vapour sulphurization (TVS).[71] [72] [73] The transition metal oxides are preferred for the CVD process due to their low melting point of 795^oC providing sufficient vapour pressure. The reaction of H_2S or sulphur mixed with hydrogen is a step reaction, by first producing MoO_{3-x} subsequently a mixture of $MoOS_2$ which is a mixture of MoS_2 and MoO_{3-x} until the final synthesis of MoS_2.

The first step for depositing MoS_2 via CVD is to choose a substrate for the deposition. MoS_2 can be deposited on amorphous Si / SiO_2 substrates and fabricated as bottom gated FET devices where the Si acts as the global back gate electrode and SiO_2 as the gate dielectric. Nevertheless the material grown suffers from small domains and the annealing in high temperature sulphur enviroment may cause diffusion of sulphur atoms in the oxide detiorating its characteristics [74][75].The epitaxial growth results in better crystallinity of the deposited material as larger crystals can be grown. For epitaxial growth the substrate must be crystalline and atomically smooth having similar lattice constants to MoS_2. MoS_2 forms a hexagonal crystal structure with lattice constants of a=3.15 Angstroms and c=12.3 Angstroms. Substrates with similar structures that can be used for epitaxial growth are c−plane sapphire, GaN, SiC and mica [76] [77] [78]. Figure 3.7 shows the MoS_2 unit cell on that of sapphires being rotated by 30^o where seven

unit cells of MoS_2 equals to eight unit cells of sapphire. This rotation is resulting in 13% of lattice mismatch for the epitaxial grown of MoS_2 on sapphire. The drawback of epitaxial growth is that the as grown film has to be transferred to Si / SiO_2 a process that induces wrinkles and dicontinuities to the 2D material [79] [80] [81].

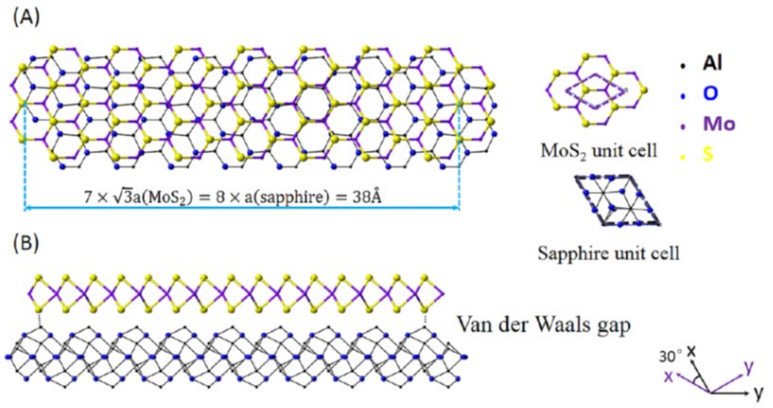

FIGURE 3.7: a) Top view and b) side view of in - plane orientation of MoS_2 on sapphire [82]

An analysis of the CVD sulphurization process by using the precursors MoO_3 and sulphur on Si / SiO_2 was presented by V. Senthilkumar et al. In this experiment different ammounts of MoO_3 were used under different sulphur concentrations giving an insight on the different stoichiometries and different shapes of deposited domains. The molybdenum precursor was placed in a quartz tube at atmospheric pressure with N_2 flow of 10 sccm with the temperature set to 830^{o}C while Sulphur was placed upstream at lower temperature. The temperature was held for 5 minutes for the deposition to take place and then it was naturally cooled down. When 3 mg of MoO_3 and low content of sulphur was used rectangular shaped molybdenum oxy sulfide was deposited. By increasing the sulphur content triangular and hexagonal shaped domains of $MoOS_2$ and MoS_2 were deposited, upon further

increasing of the sulphur content a partially continuous film by the merging of the nucletaed domains was observed with numerous domains deposited on top of them. Next the MoO_3 content was examined by keeping a high content of sulphur. When low content of the metal oxide precursor was used (0.26 mg) triangle domains were deposited with sizes around 5 μm, upon increasing the content of the metal precursor(0.5 mg flakes grew bigger with sizes between 40 - 100 μm. A final increase of the moly precursor (1.9 mg) led to large grain boundaties except at the edges of the substarte covering an area of 0.8 cm^2. Further increase in the moly precursor resulted in thick films with observable grains and isolated flakes deposited on top. [71]

Lee et al. employed the typical CVD procedure by placing MoO_3 powder in a ceramic boat and a Si/SiO_2 substrate facing down and mounted on the top of the boat. A separate ceramic boat with sulfur powder was placed next to the MoO3 powder. Prior to the growth, a droplet of aqueous reduced graphene oxide (rGO), perylene-3,4,9,10-tetracarboxylic acid tetrapotassium salt (PTAS) or perylene-tetracarboxylic dianhydride(PTCDA) solution, is spun on the substrate surface followed by drying at 50 °C. These are acting as seeding sites. During the synthesis of MoS_2 sheets, the reaction chamber is heated to 650 °C in a nitrogen environment. At that high temperature, MoO3 powder is deposited on the substrate and further react with sulfur vapor to grow MoS_2 films. This technique provides MoS_2 films that are consisted of monolayer, bilayer and other few−layer MoS_2. The device mobilities where measured to be up to 0.02 $cm^2 \cdot V^{-1} \cdot s^{-1}$ [83]. Table 4.1 lists a number of the various protocols for CVD of MoS_2 that have been presented over the years employing MoO_3 and sulfur precursors with varying temperatures and amount of precursor masses.

In a third approach shown in figure 3.8 by C.C. Huang et al. the precursors are introduced in their gaseous form and no seeding sites are used, making the procedure straightforward. The deposited films cover areas >1000 cm^2. The protocol is based on APCVD at ambient temperatures and a two step annealing process. Solid $MoCl_5$ precursor which has a relatively high pressure at room temperature is kept in a bubbler and delivered at the reaction tube without heating in the form

TABLE 3.2: CVD of MoS_2 using as precursors MoO_3 and sulfur

MoO3 (grams)	S (grams)	T (^{0}C)	Time (min)	Carrier gas flow	Ref.
0.005	0.35	700	10	10 sccm Ar	[84]
0.01	0.2	850	20	100 sccm Ar	[42]
0.018	0.016	650	3	5 sccm Ar	[85]
0.025	0.5	850	180	150 sccm Ar	[86]
0.03	0.01	650	5	10 sccm Ar	[87]
0.4	0.8	650	15	1 sccm N2	[88]

of vapor by argon carrier gas, then H_2S is introduced in the reaction tube resulting in the deposition of an amorphous MoS film. The actual composition of the thin film deposited is $Mo_26S_61Cl_{13}$ for that reason the first annealing step is used to remove Cl atoms in an environment of H_2 - H_2S at 500°C followed by the second annealing step at 900°C at H_2S environment in order to convert the amorphous phase of MoS_3 (grown after the reduction step at 500°C) to MoS_2.[89]

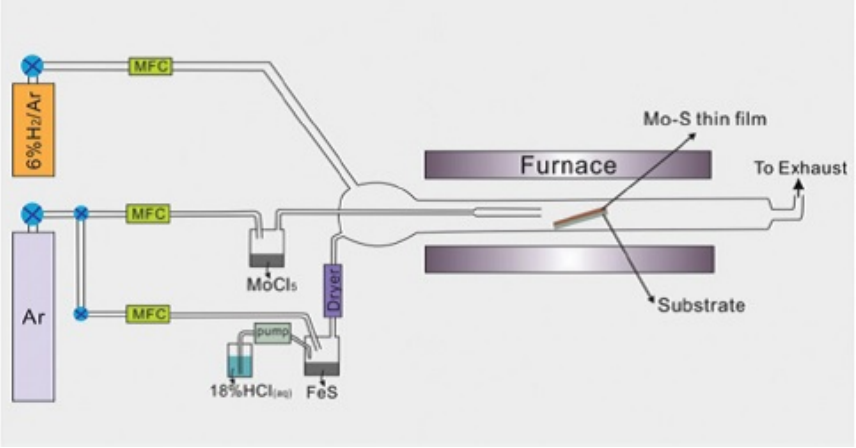

FIGURE 3.8: Representation of the gaseous precursors CVD protocol [89]

.

3.3.3 Transfer of TMDCs

In order to fabricate back gated FET devices after growth, TMDCs are transferred from the as grown substrate.[80][62] As in graphene the first protocols for transferring TMDCs involved a sacrificial polymer layer on top of the material and etching of the substrate. But in the case of TMDCs in order to etch the insulating

substrates harsher alkali or HF is being used. These highly corrosive substances deteriorate the properties of TMDCs. For that reason less aggressive protocols with high yield must be used for the transfer to suitable substrates. We will review two different approaches that are friendlier to the material and preserve the growth substrate for further depositions after transfer of the material. The first technique is based on ultrasonic delamination. The TMDC is spin coated with a polymer solution that is cured in order to remove the solvent. Then the sample is immersed in a H_2O ultrasonic bath. The delamination of the material begins to happen within a minute and then is ready for transfer to the desired substrate. Finally the polymer is removed with the suitable solvent. The mechanism of delamination is presented in figure 3.9. During ultrasonication millions of cavitation bubbles are generated at the initial of the negative pressure period of the ultrasonic wave, these bubbles rapidly expand into larger bubbles until the pressure suddenly switches from negative to positive. In a short time, these bubbles are compressed and collapse at the rising of the positive pressure period, releasing an enormous amount of energy, which produces enough force in the interface between Polymer/MoS_2 stack and the insulating substrate. Within many cycles, the bubbling forces steadily delaminates the PMMA/TMDC stack from the growth substrate [81].

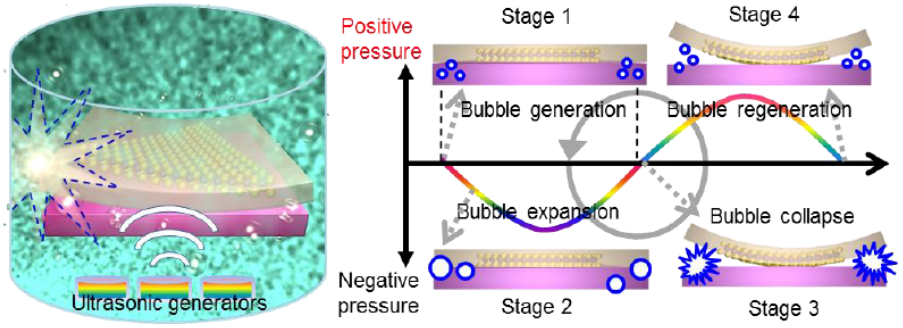

FIGURE 3.9: Mechanism of action of the ultrasonic delamination [81]

.

The second technique presented in figure 3.10 is using the hydrophobic nature of TMDCs and the hydrophilic nature of c−plane sapphire in order to delaminate the material with H_2O. A thin layer of polystyrene (PS) is spin−coated on the as grown MoS_2 films on sapphire substrates followed by a baking process at 80

°C − 90 °C for 15 min. Then a water droplet is dropped on the PS layer. The water is expected to penetrate between the TMDC film and the substrate due to different surface energies but the penetration actually cannot start by itself. This is because the intimate adhesion of the synthesized film with the substrate blocks the penetration. A gentle poking at the edge of the polymer/TMDC assembly with a sharp object, that create cracks at the edge, starts the water penetration. The polymer/TMDC assembly is then lifted off instantly and floats on top of the water droplet. The detached polymer TMDC assembly is dried by sucking the water droplet away with a paper towel. Then the material is transferred on the desired substrate. The final step is the baking of the transferred assembly at 80°C for 1 h to remove water residues and then at 150°C for 30 min to spread the polymer for the elimination of possible wrinkles. Finally polystyrene is dissolved in toluene bath [90].

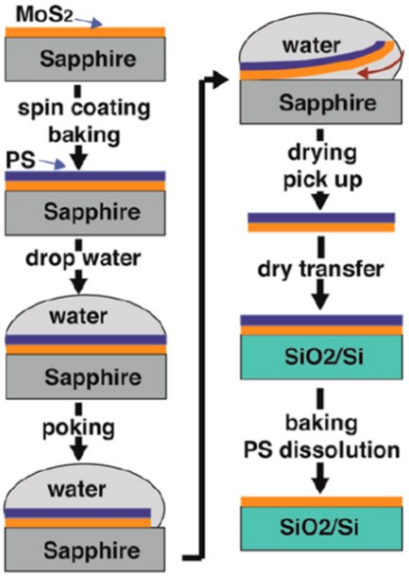

FIGURE 3.10: Water assisted transfer[90]

.

3.4 Graphene and MoS_2 devices

With the isolation of two dimensional graphene crystals the employment of graphene and TMDCs as the active materials in field effect transistors became a common approach. Nevertheless the amazing properties of 2D materials has led to applications beyond typical FETs such as p−n diodes, memristors, electrical biosensors etc.[91][92][93]

Figure 3.11 depicts a typical field effect transistor that is consisted of a gate, a channel region, between a source, a drain electrode and an insulating layer that separates the channel region active material from the gate electrode. The principle of operation of a typical FET is the control of the channels conductivity, thus the output drain current, by a voltage that is applied perpendicular to the channel between the source and the gate, Vgs. The ideal FET material should have four requirements. The material must be able to switch off for use in digital logical so it must have a sizeable bandgap. The current output should saturate with increasing source drain voltage in order to obtain high power gain. Short channel effects, a detrimental issue for devices nowadays, should be suppressed, otherwise the intrinsic properties of the material and thus the device are deteriorated. And finally high carrier mobility of the material is needed for the FETs to respond quickly to the variations of Vgs. Graphene fulfills these requirements except the bandgap, though there are reports of a graphene bandgap through epitaxial growth, or by biasing double layer graphene and finally by the fabrication of nanoribbons.

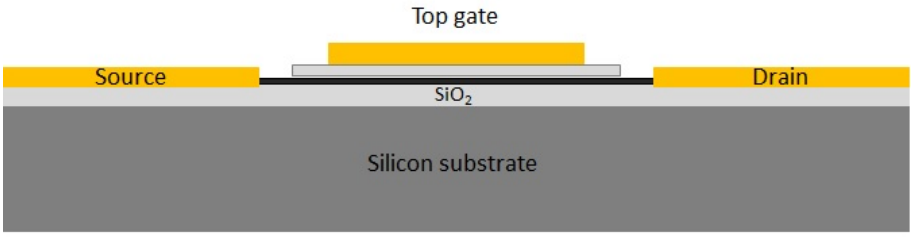

FIGURE 3.11: Typical top gated FET configuration

.

A typical graphene FET consists of a highly doped silicon that acts as the back gate with a silicon oxide grown on top of it. Then 2D graphene is transferred to the oxide and by EBL or photolithography patterning source and drain electrodes are being defined and deposited. This kind of device is easier to fabricate since the substrate acts as a universal back gate for multiple devices. Nevertheless, this architecture has major drawbacks such as large parasitic capacitances and degradation of the intrinsic high mobilities of the graphene carriers, due to charged impurities[94]. The alternative approach to this device architecture is that, of a the top gated devices, by employing alternative high k dielectrics such as HfO_2 and Al_2O_3, which is more demanding during the fabrication but reduces the parasitic capacitances and the degradation of the carriers mobilities [95] [96]. The carrier type and density in the graphene channel are governed by the potential difference between the gate and the channel. If positive gating is applied, electron accumulation is promoted, and if negative gate is applied, a p−type channel is created. This ambipolar behavior can be observed in the transfer curve with two branches, one for hole, and one for electron conduction. The minimum point between those two branches is the Dirac point. The position of the Dirac point is dependent on the type of doping, the difference between the work functions of the gate and the graphene and the density of the charges at the interface of the channel [95] [97] [98]. Typical output characteristics of a CVD grown graphene FET is presented in 3.12 where the p − branch is shown for negative gate voltages due to hole conduction and the n − type branch for posive voltages due to electron conduction.

TMDCs being the 2D analogue of graphene are also employed as field effect transistors. The most studied TMDC MoS_2, like most of these materials, has a bandgap when isolated down to one atomic layer. From the knowledge achieved by the graphene FETs, MoS_2 back gated and top gated devices have been presented in the literature, their respective configurations are presented in figure 3.13. The back gated devices on top of Si SiO_2 present low mobility in the order of 0.1 10 cm^2 V^{-1} s^{-1}. The dominant cause for these low room−temperature mobilities

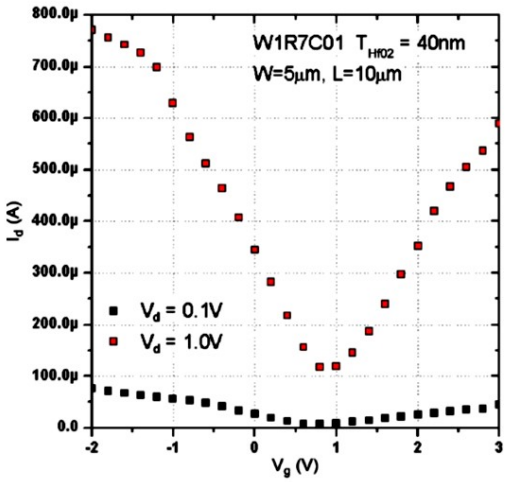

FIGURE 3.12: Typical CVD grown graphene FET transfer curve [99]

in MoS_2 devices are inflicted by charge traps present at the interface between the substrate and the MoS_2 layer. The deposition of high−k dielectrics show an improvement of mobility due to suppression of Coulomb scattering due to the high k dielectric environment and the modification of phonon dispersion in MoS_2 [100]. Furthermore by using a top gate a stronger electrostatic doping of the MoS_2 can be achieved due to the higher dielectric constant and the smaller thickness of the high k dielectric layer compared to that of the bottom−gate SiO_2 .

Another key parameter of MoS_2 FETs is the metal semiconductor contact. A common issue in 2D TMDCs is the Fermi level pinning of the TMDC and the metal. This leads to the formation of a Schottky barrier . Although small Schottky barriers with different metals like Titanium have been achieved between few−layer or multilayer MoS_2 and contact metals, even these small Schottky barriers still influence the output characteristics of the device [101] [102]. A number of different metals with different work functions shown in figure 3.14 such as Au, Ni, Pd have been used in order to achieve a pure Ohmic contact between MoS_2 and the metal pads.[103]

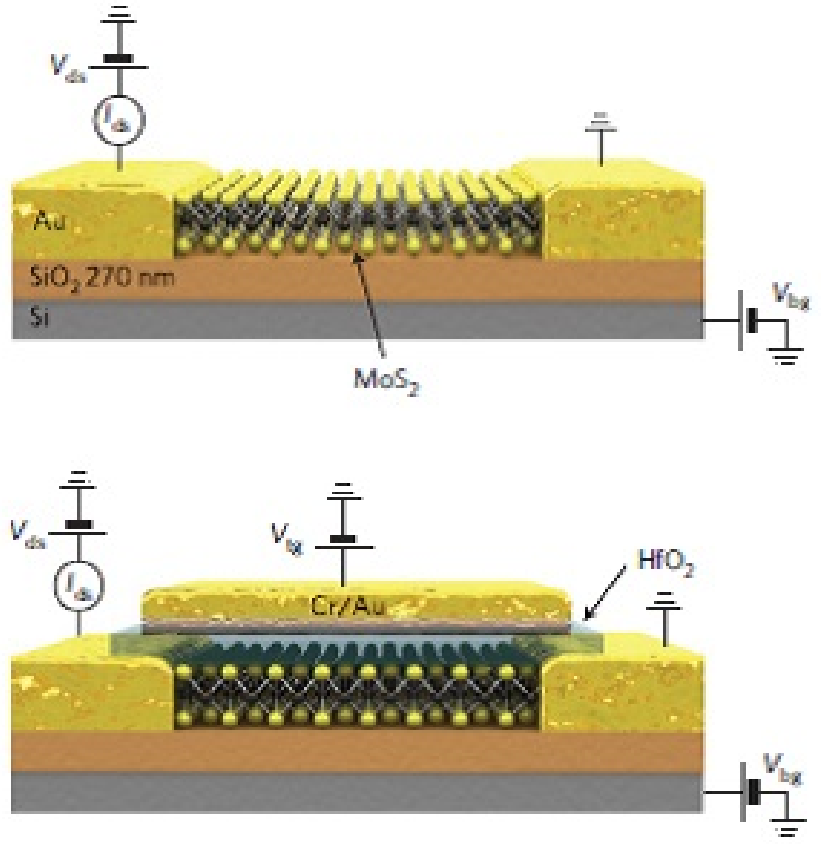

FIGURE 3.13: Typical MoS_2 configurations of Si / SiO_2 back and top gated FETs [100]

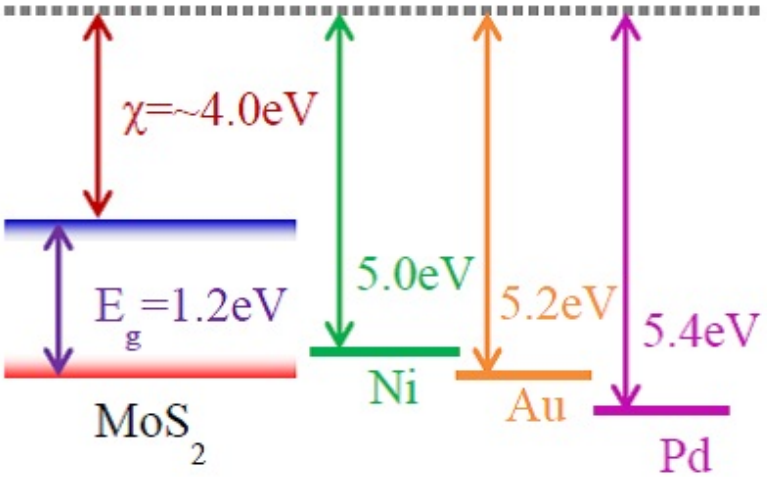

FIGURE 3.14: Work functions of MoS_2 and typical metal contacts[[103].

The lowest Schottky barrier that has been reported has been achieved by using Scandium contacts. MoS_2 FET with scandium contacts and high k dielectric has presented the highest mobility as well, reaching 700 $cm^2 \cdot V^{-1} \cdot s^{-1}$. [104] The following curves are characteristic curves of mechanically exfoliated MoS_2 FETs depicting a clear saturation region, in contrast to graphene as stated before. In figure 3.15 we observe a steep subthreshold slope at 60 mV per decade. At negative gate voltages, the drain current rises again indicating the formation of an inversion channel. Figure 3.16 shows the MoS_2 characteristic curves by electrochemical exfoliation exhibiting lower on off ratio and a higher subthershold slope when compared to the mechanically exfoliated MoS_2.

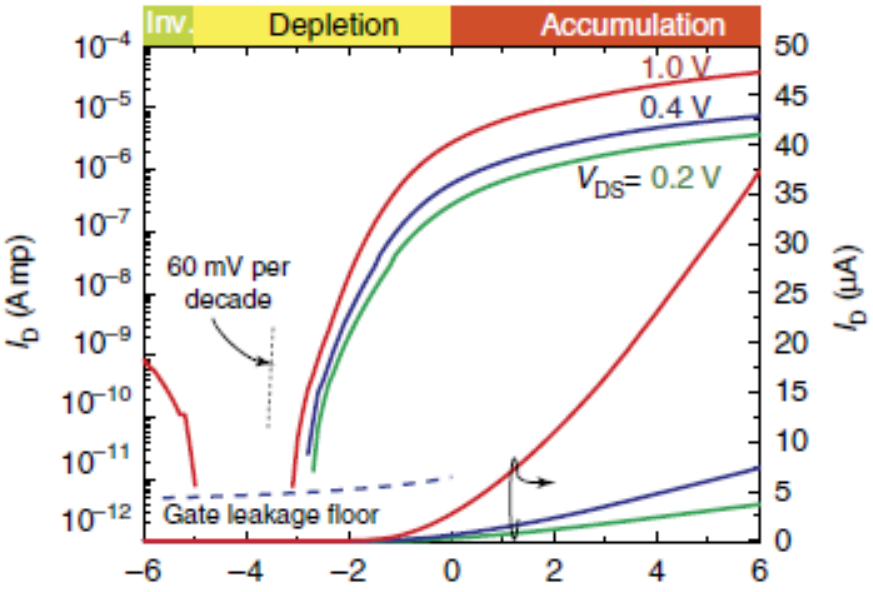

FIGURE 3.15: Tranfer curve of a MoS_2 FET [105]

The electronic properties of monolayer measured by fabricating transistor devices is about 1.2 $cm^2 \cdot V^{-1} \cdot s^{-1}$ [69].

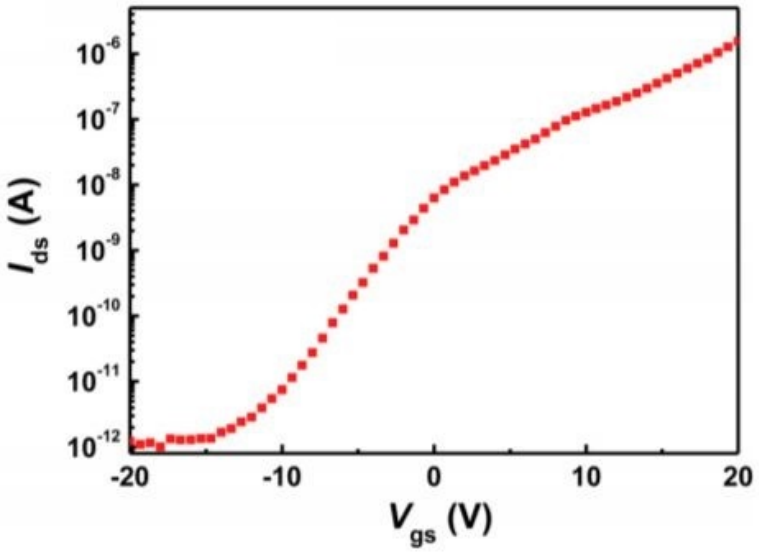

FIGURE 3.16: IdVg of electrochemically exfoliated MoS_2 [69]

Following the successful exfoliation of two dimensional MoS_2 flakes and their fabrication into FETs a number of techniques have been pursued for the wafer scale deposition towards electronic applications, including CVD, thermal vapour sulfurization and ALD. Table 3.3 summarizes the aforementioned techniques and the electrical properties of the grown films.

TABLE 3.3: FETs fabricated by syntesized MoS_2

Growth method	Gate	Dielectric	On/Off	Ref.
CVD	Back	SiO_2	10^3	[83]
CVD	Top	HfO_2	10^5	[106]
TVS	Back	SiO_2	-	[107]
TVS	Back	SiO_2	10^4	[108]
TVS	Back	SiO_2	10^5	[109]
ALD	Top	Al_2O_3	10^3	[110]

Chapter 4

Experimental synthesis of 2D materials

4.1 Introduction

This chapter contains the experimental techniques developed for depositing and growing 2D materials through CVD for graphene where the effects of pressure temperature and the ratio of H_2 to CH_4 were evaluated towards high quality monolayer graphene. CVD of HfS_2 was investigated for wafer scale deposition using $HfCl_4$ and H_2S, while ALD - TVS techniques were used for the growth of MoS_2. ALD was selected due to its high uniformity deposition yield of stoichiometric thin films, a condition of high importance for few layer atomically thin films such as MoS_2 on a wafer scale.

4.2 Graphene LPCVD

The first step for the graphene CVD was the temperature calibration of our CVD system presented in figure 4.1 ,so we have a good knowledge of the actual area that has the predefined temperature we have selected while the CVD system setup

is presented in Figure 4.2 . The callibration measurements gives as the maximum copper foil that can be used in order to deposit homogeneous graphene samples.

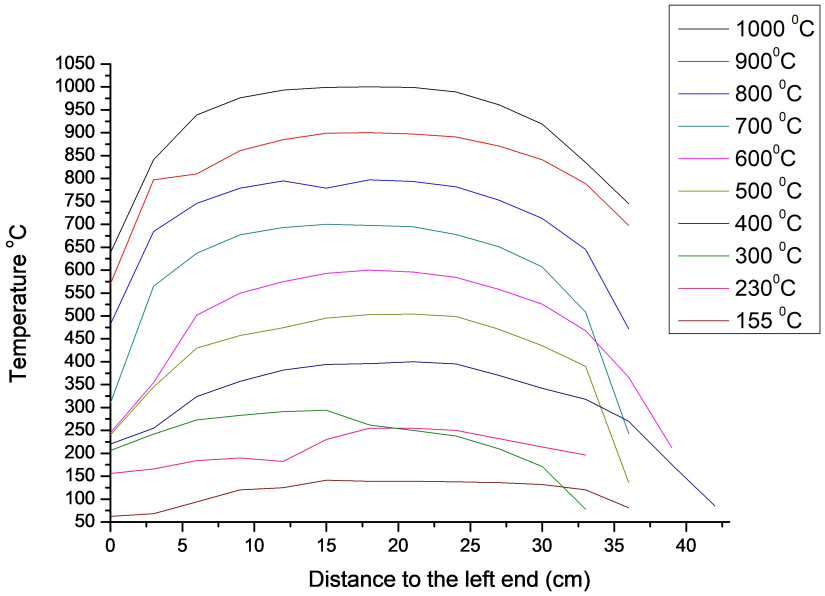

FIGURE 4.1: Tube furnace calibration

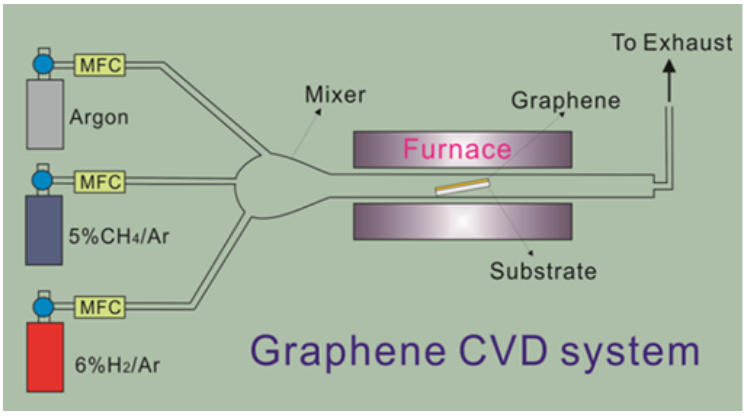

FIGURE 4.2: CVD system [89]

For the gas delivery gas flow meters were used controling a gas line with a mixture of 5% CH_4 diluted in high purity Ar as a carrier gas a second gas line of 6% H_2 diluted in high purity Ar and Ar as a carrier gas. A single zone furnace that can reach up to 1200 ^{0}C was used. The CVD reactor seen in figure 4.3 consisted of a 50 mm OD guartz tube were a a 40 mm OD tube was inserted carrying a Cu foil

with dimensions of 10 cm $*$ 10 cm wrapped on the inner tube. The copper foil used for these experiments were 25 μm 99.8% purity from Alfa Aesar.

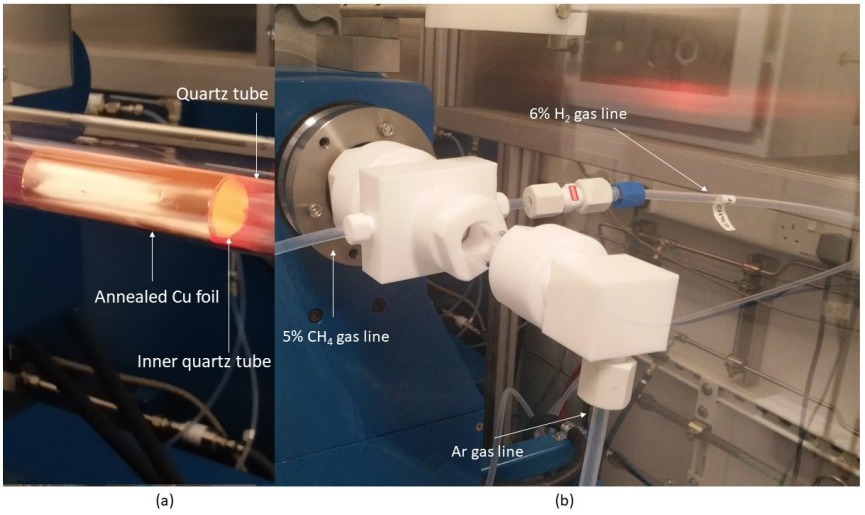

FIGURE 4.3: (a) CVD reactor for graphene deposition (b) CVD tube fitting for mixed 5% CH_4, 6% H_2 and gas delivery of pure Argon

Before the CVD protocol the copper foil was cut to the appropriate size and cleaned with acetone , isopropanol and dried with nitrogen gas. The next step was immersing the foil in an acetic bath for 10 min. to remove the native oxide of the copper foil that can hinder the deposition of graphene and reduce its average roughness. Then the 10 cm x10 cm Cu foil is carefully wrapped around the inner tube, by being extremely cautious not to structurally damage it. Then finally the reactor was cycled five times from 1013 mbar to 3 mbar with Argon flow at 500 sccm in order to remove the oxygen. Upon the elimination of oxygen from the CVD reactor the temperature was set to the deposition temperature with a ramping rate of 20^0C / min solely with Ar flow. H_2 gas was inserted at 900 ^{0}C for 30 min. in order to eliminate the copper's native oxide. Finally the methane was injected in the CVD system for the appropriate time and pressure for the graphene deposition. After the deposition the furnace is moved away from the copper foil in order to rapidly cool down the system, the overall heating profile of the CVD process is presented in figure 4.4. This has no physical or chemical aspect as it would have in Nickel based graphene CVD and is just implemented for minimizing the overall CVD procedure time.

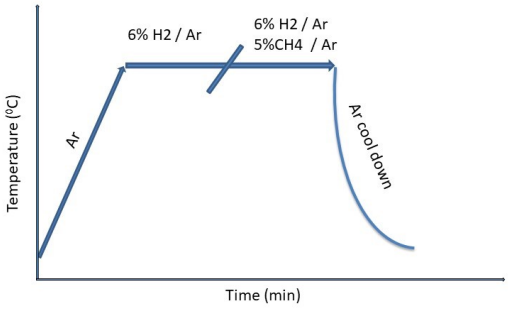

FIGURE 4.4: Typical heating profile of graphene CVD

4.2.1 Graphene CVD process optimisation

Graphene CVD was examined in wide optimisation windows at varied pressures, gas ratios and temperatures in order to extrapolate safe results of the optimum parameters of the protocol. All samples were analyzed by Raman spectroscopy. For the analysis of the graphene Raman peaks all graphs were corrected by subtracting the baseline of the plots in order to eliminate the fluorescence from the copper foil and analyzed by Lorentzian fitting. For the quality of the CVD grown graphene the ratio of the D/G was examined while for the successful monolayer deposition the ratio of the 2D/G.

For the graphene optimisation process first the pressure parameter was investigated. The deposition temperature (850 ^{0}C) and gas flows (100 sccm /210 sccm for 6% H_2 and CH_4 respectively) were held constant while the pressure was varied at 20 mbar, 250 mbar and 500 mbar. Figure 4.5(a) shows the annealing at 20 mbar resulted in monolayer deposition giving a ratio of 2.7 for the 2D/G peaks and a ratio of 0.15 for the D/G. In Figure 4.5(b) the results for the 250 mbar deposition show an increase of the D/G ratio at 0.22 while the 2D/G peaks revealed a monolayer ratio of 3.05. Finally deposition at 500 mbar Raman results in 4.5(c) revealed bilayer deposition of graphene with a significant increase at the defect ratio at 0.7.

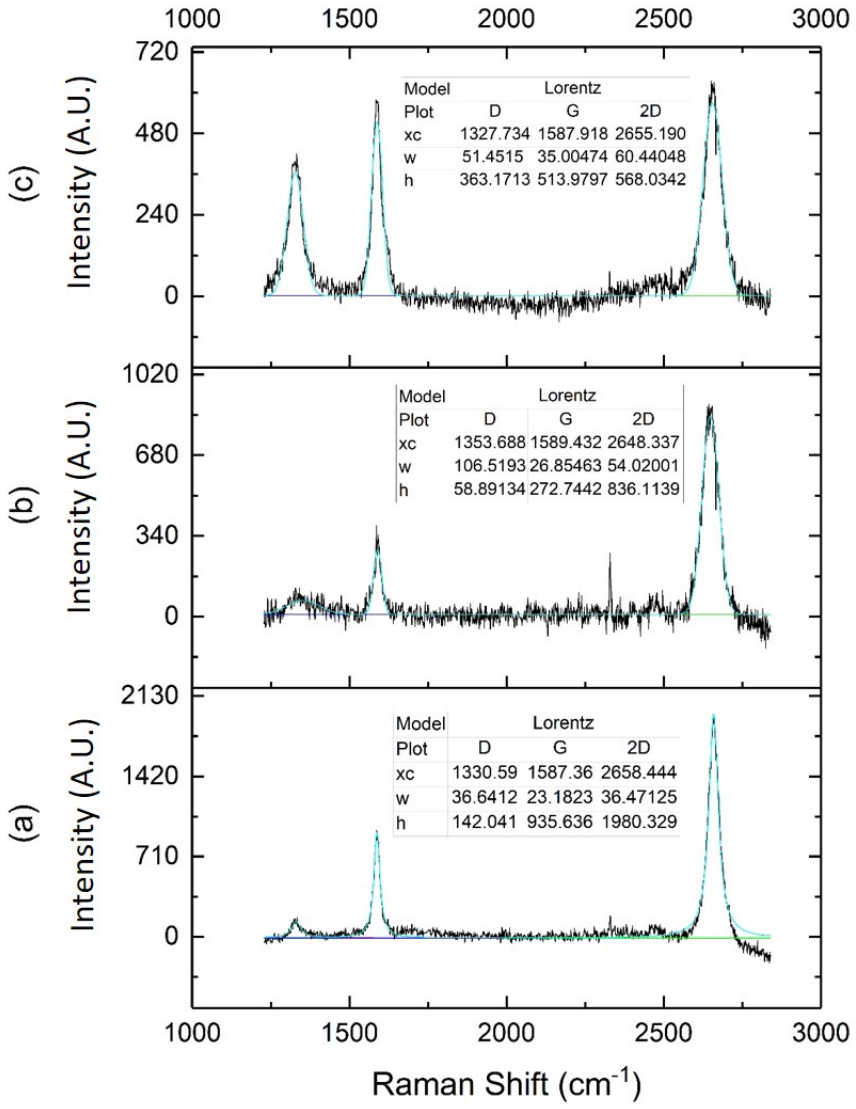

FIGURE 4.5: Raman characterization of graphene CVD growth at different pressures of a)20mbar b)250 mbar c)500 mbar

Next the gas ratios of methane and H_2 were varied at 100 sccm /210 sccm, 210 sccm / 100 sccm and 100 sccm /100 sccm for 6% H_2 and 5%CH_4 respectively while maintaining the deposition temperature at 900 ^{0}C and pressure at 20 mbar. Figure 4.6(a) shows the annealing at 100 sccm /210 sccm at 950^{0}C presented a small D peak unresolved by the Lorentz fitting while introducing a gas ratio of 210 sccm /100 sccm seen in 4.6(b) resulted in the emergence of the defect peak with ratio of the D/G at 0.2. For the 100 sccm / 100 sccm gas flows results shown in

4.6(c) the defect ratio dropped at 0.18 highlighting the need of excessive H_2 during the deposition. For these paramaters of gas ratios all the depositions resulted in monolayer graphene with 2D/G peak ratios between three and four.

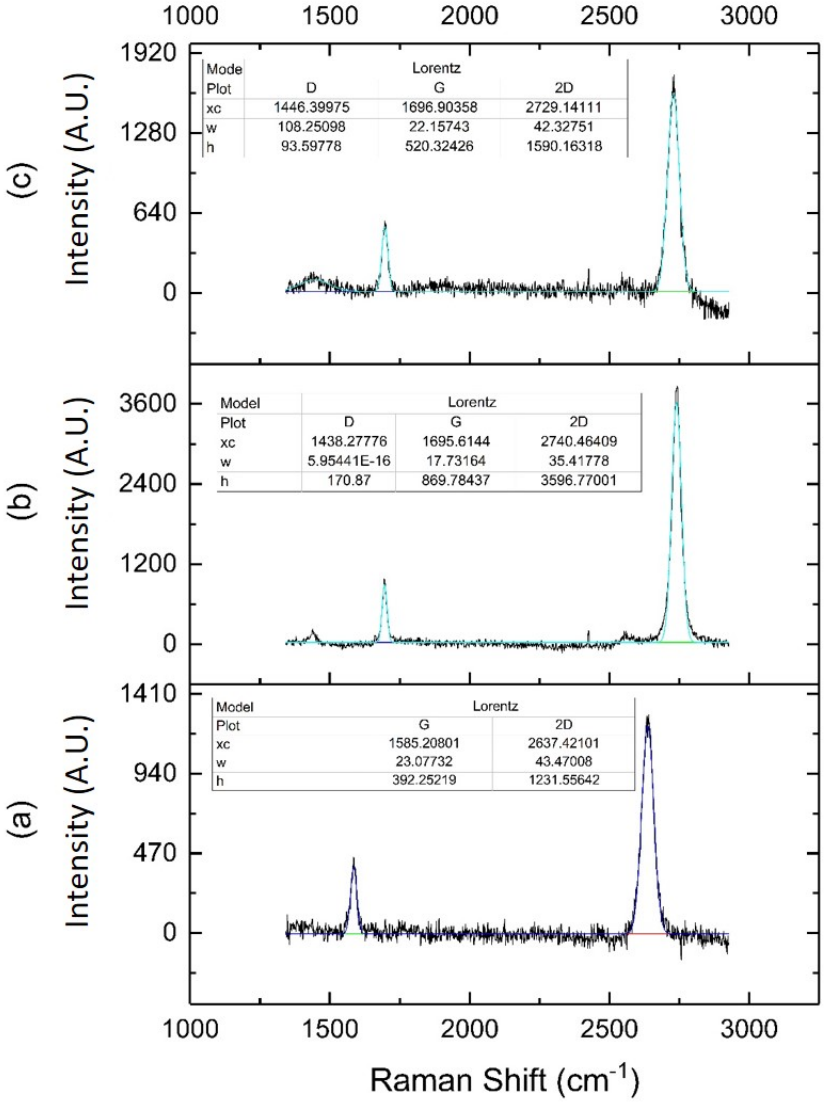

FIGURE 4.6: Raman characterization of graphene CVD growth at different gas ratios of 6% H_2 / 5%CH_4 a)100 sccm /210 sccm b)210 sccm / 100 sccm c)100 sccm /100 sccm

Finally the temperature effect was examined with depositions at 825^0C, 925^0C and 1025^0C, the gas ratio was kept at 210 sccm / 100 sccm and the pressure at 20 mbar. The deposition temperature was limited at this upper limit to avoid copper evaporation with copper having a melting point at 1085^0C. All the depositions

in this experiment resulted in monolayer depositions with the ratio of the 2D/G between three and four. The defect ratio for the 825^0C deposition showed in figure 4.7(a) was found at 0.2 while increasing the temperature at 925^0C shown in figure 4.7(b) reduced the defect ratio at 0.18 while further increase of the temperature presented in figure 4.7(c) resulted in higher defect ratio at 0.32.

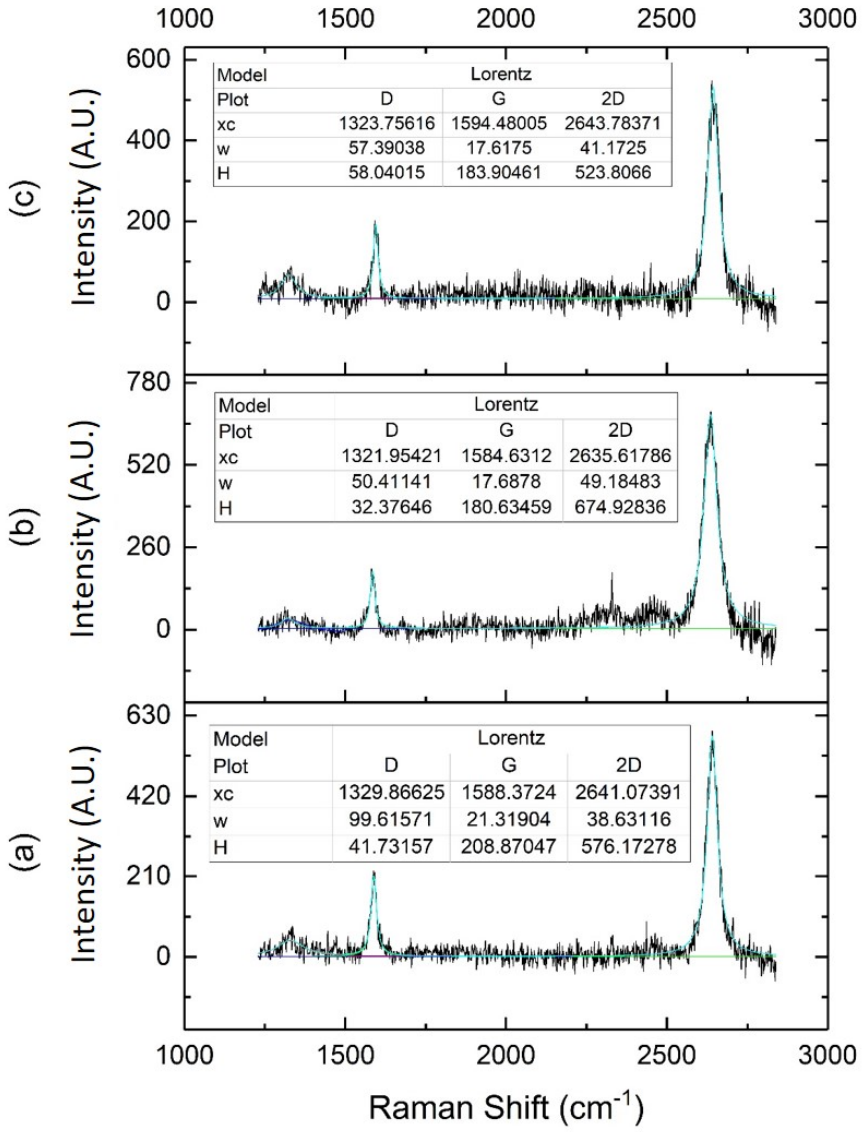

FIGURE 4.7: Raman characterization of graphene CVD growth at different deposition temperatures at a)825^0C b)925^0C c)1025^0C

Overall the minimum defect density was found for a gas ratio of 100 sccm / 210 sccm for H_2 / CH_4 at 20mbar and temperature of 900^0C. Reducing the temperature

resulted in higher defect densities that can be attributed to the non complete decomposition of the methane gas while the defect increase at higher temperatures can be explained by the slow vaporization of copper at high temperatures close to its melting point.

4.3 HfS_2 growth via $HfCl_4$ LPCVD

Up to now in the literature there has been presented a number of TMDCs exhibiting a band gap sufficient for optoelectronic applications. Nevertheless TMDCs lack the high mobility graphene exhibits for implementation in applications. A number of TMDCs shown in figure 4.8 with sizeable bandgap has been predicted and mobilities compared to that of silicon or even higher[111]

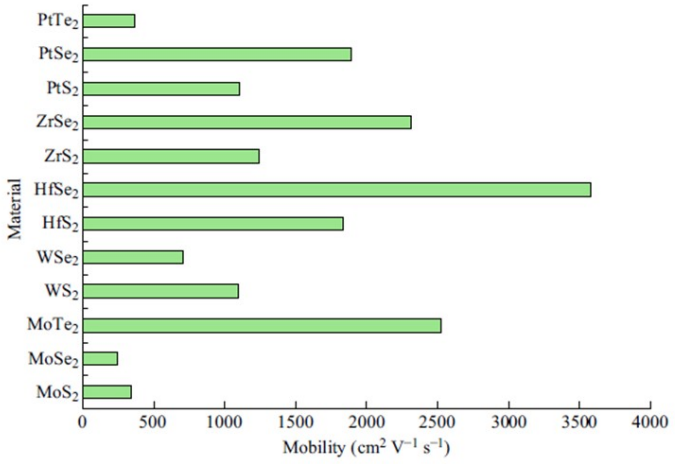

FIGURE 4.8: High mobility TMDCs [112]

In the previous chart we can observe five TMDCs with high carrier mobilities from which up to today none of them, excluding ZrSe2 [113], has been deposited via CVD whereas some of them have been deposited by other means [114]. We have chosen as material of interest HfS_2 disregarding the disambiguate information of

its bandgap [115]. Recently an exfoliated few layered phototransistor by K. Xu etal. was presented exhibiting high photoresponsivity [116].

In order to deposit HfS_2 we have chosen as hafnium containing precursor the metal halide $HfCl_4$. The software Factsage was used in order to validate the thermodynamical feasibility of the reaction of the precursor with H_2S. The chosen parameters for the synthesis was pressure of 20 mbar and temperature of 850^0C. Figure 4.9 shows that the reaction of the precursor with H_2S for the chosen parameters is complete providing pure H_2S with no apparent byproducts such as amorphous HfS_3 or unreacted chlorides.

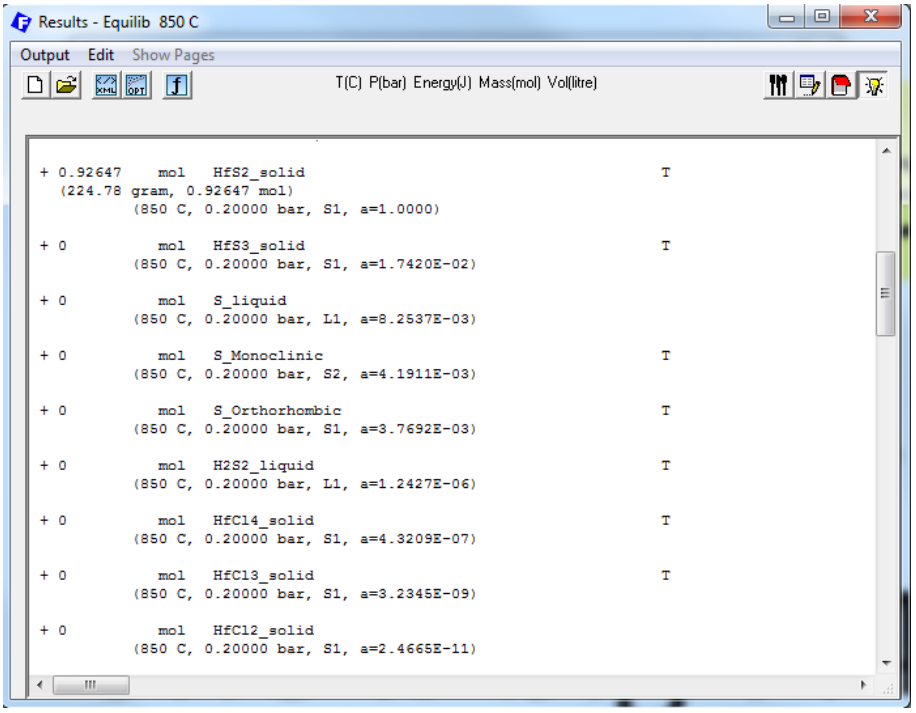

FIGURE 4.9: Factsage software screenshot where the CVD parameters chosen resulted in HfS_2 with no byproducts present

The experiment was carried out in order to establish the deposition feasibility on Si/SiO_2 and sapphire substrates. The substrates were treated with piranha solution for 2 minutes in order to remove any organic contaminants and in order to promote the surface hydrophilicity. The CVD deposition took place in a three zone furnace. The first zone was heated at 175^oC for the precursor to reach the desired vapor pressure and the third zone used for the deposition was heated to 850^oC. Figure 4.10 the precursor placed in a quartz injection tube inserted in a

bigger CVD tube. When the desired temperature is reached the precursor zone is heated and when the setpoint temperature is reached flow of H_2 (50 sccm) through the injection tube is initiated. In order to reduce the transfer of the solid precursor to the substrates before the deposition step the system is kept at 900 mbar while Argon (200 sccm) is flowing through the main CVD tube and no gas is flowing through the injection tube. When the deposition step is initiated the system is pumped to 20 mbar.

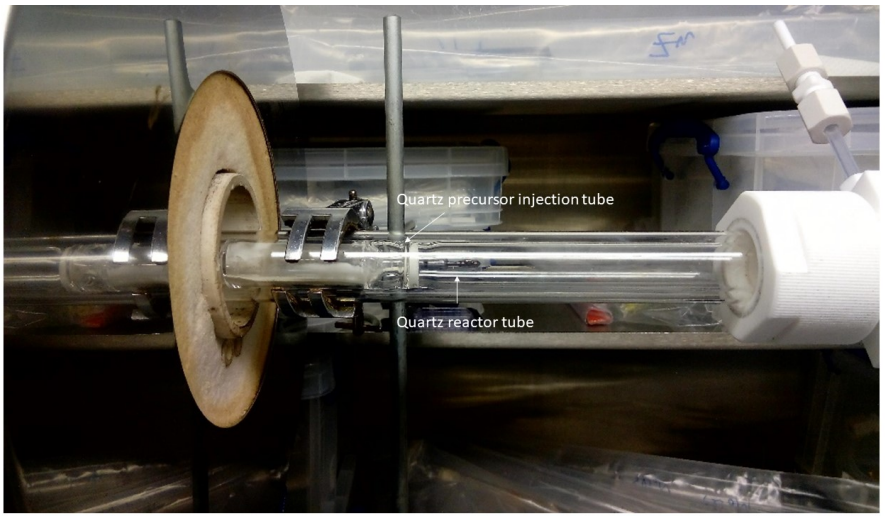

FIGURE 4.10: The injection tube containing the precursor and the CVD tube

After the deposition all the samples were characterized using Raman spectroscopy using 532 nm laser irradiation. Bulk HfS_2 exhibits two prominent peaks, one at 337 cm$^-$1 and one at 260 cm$^-$1, where the first one is the out of plane vibration mode A_1g and the second one is the in plane vibration mode E_g. [117] [118] Our samples presented the aforementioned peaks seen in figure 4.12 with the A1g mode exhibiting a consistent red shift of 1 cm^{-1} and the E_g exhibiting large blue shifts. These E_g shifts could be attributed to chemical, strain effects or different film thicknesses. Since the shifts of the E_g mode are correlated with the in plane vibrations we can hypothesize that these shifts are attributed either to strain effects due to non−uniform deposition and or thickness variations.

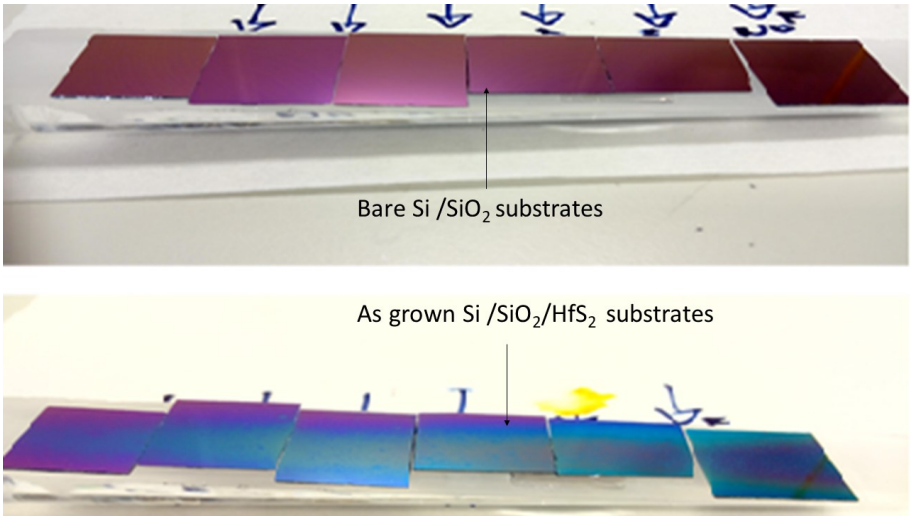

FIGURE 4.11: Si / SiO_2 before and the after the deposition

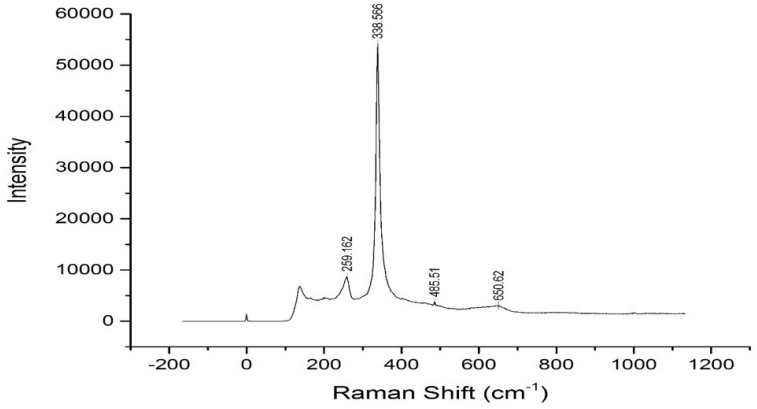

(a)

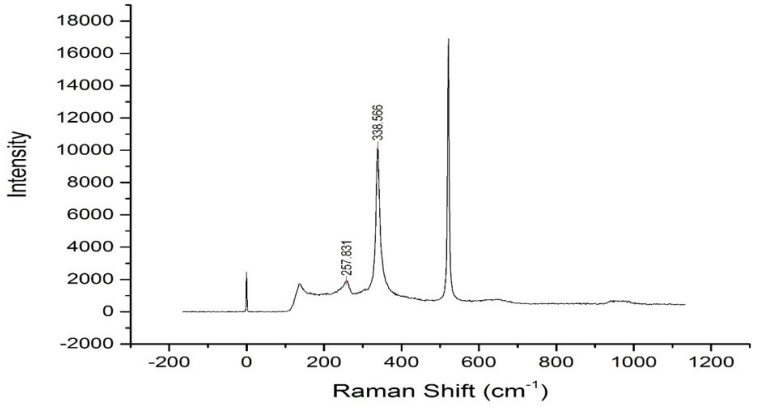

(b)

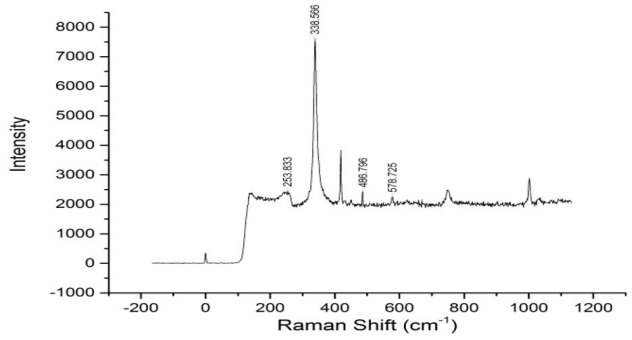

FIGURE 4.12: Raman measurements of HfS_2 exhibiting large E_2g Raman Shifts at a) 259.1 cm^{-1} b)257.8 cm^{-1} and finally c)at 253.8 cm^{-1}

To elucidate the observed Raman shifts of the HfS_2 films, material grown epitaxially on a sapphire substrate was examined by SEM. Figure 4.13 showed the successful deposition of HfS_2 exhibiting micron scale domains with numerous cracks that explain the aforementioned Raman shifts. This can be attributed to the inherent limit of the mass flow controllers of the setup that were calibrated of a minimum flow of 50 sccm, resulting in a supersaturated sulphur enviroment that can lead to a high reaction rate inducing numerous nucleation sites resulting in stress and the formation of cracks. Furthermore figure 4.14 photoluminescence measurements has provided information about the materials energy bandgap. These results come in contrast with the paper published by C. Kreis etal where it is claimed that HfS_2 is an insulator with an energy bandgap of 3.6 eV regardless the number of layers [115]. Our findings are in agreement though with K. Xu etal where an exfoliated few layer HfS_2 phototransistor responding to 633 nm laser was presented [116].

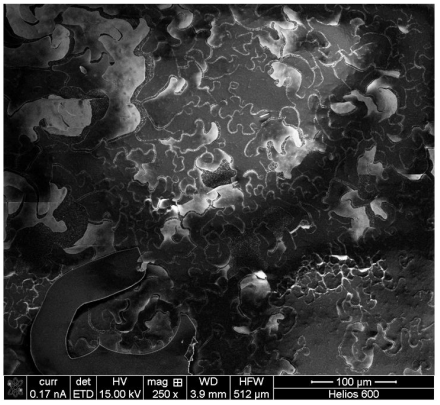

FIGURE 4.13: SEM of HfS_2 film grown epitaxially on sapphire substrate

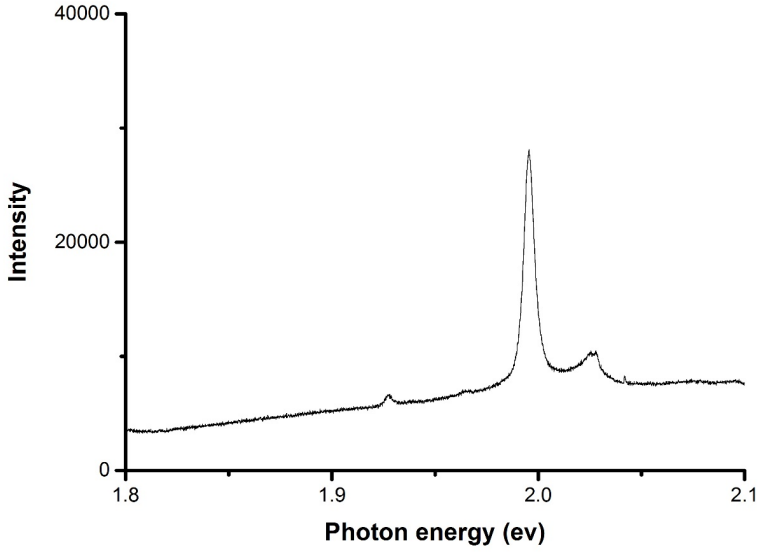

FIGURE 4.14: Phtotoluminescence of CVD grown HfS_2

4.4 MoS_2 growth via TVS of ALD grown MoO_3

4.4.1 ALD growth of MoO_3

For the wafer scale growth of MoS_2, ALD was employed in order to deposit ultrathin films of MoO_3 on Si/SiO_2 wafers. The substrates used were 6-inch p-type silicon wafers. The wafers provided in a new sealed box from IBD who had ran an RCA clean as the last step. The results from the particle counter showed that the

wafers were coming out more contaminated after the RCA clean in the Nanofab labs. This was eventually resolved but as the wafers received from IBD were virtually contamination free, they were used as received. As a first step, a high quality 100 nm of thermal SiO_2 was grown at 1000^{o}C in a tube furnace in 53 minutes 35 seconds . The wafers were then put into a UV / O_3 reactor for 10 minutes to improve the termination of the surface oxide. The next step was to grow the MoO_3 using a thermal ALD process in the Cambridge Nanotech Savannah S200 system. A process using the precursor bis(tert-butylimido)bis(dimethylamido) molybdenum as a molybdenum source and ozone for the oxidation were used. First 100 cycles of ALD was carried out at 300^{o}C in order to examine the deposition rate of the ALD process. The as deposited oxide was characterized by ellipsometry in order to measure the thickness and estimate the deposition rate. Figure 4.15 showed a thickness of 11 nm grown oxide. The next step was to carry out the ALD process for 15 cycles. The ellipsometry mapping presented in figure 4.16 resulted in a film of 1.2 nm of MoO_3 with the thickest regions found at the edges of the wafer at 1.395 nm while the central area exhibiting the thinnest deposited film with a thickness of 1.227 nm resulting in an average thickness of 1.29833 nm and a standard deviation of 0.04697. The grown film was also characterized by XPS in order to calculate the stoichiometry.

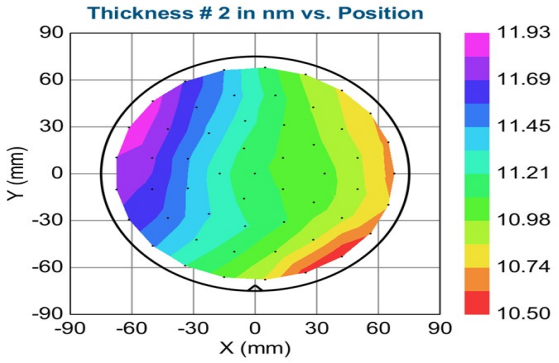

FIGURE 4.15: Wafer uniformity in nm of 100 ALD cycles grown MoO_3

For the curve fitting Shirley backgrounds where applied for all spectra. The Mo3d spectrum was fitted by applying a spin orbit doublet with a Lorentzian Gaussian

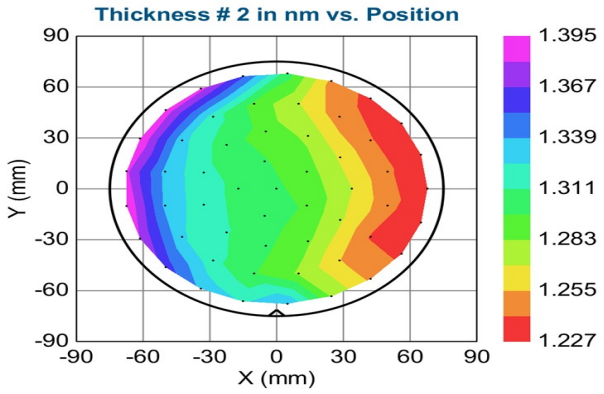

FIGURE 4.16: Wafer uniformity in nm of 15 ALD cycles grown MoO_3 thin film

mix of 30/70 and a fixed separation of 3.1 eV. In Figure 4.17(a)the $3d_{5/2}$ was found at 232.49 and the $3d_{3/2}$ at 235.66 eV . This doublet values correspond to the Mo^{6+} oxidation state of MoO_3. No further peaks were deconvoluted at lower binding energies corresponding to the lower oxidation states of Mo^{5+} and Mo^{4+} of reduced molybdenum oxides.Figure 4.17(b) shows the S_{2p} scan which is usually collected in order to find the S_{2p} peaks corresponding to sulphur atoms bound to Molybdenum, since this scan was performed on as deposited molybdenum trioxide no sulphur peaks are present. The oxygen spectrum is presented in Figure 4.17(c), this spectrum revealed two peaks with the most prominent one located at 531.22 eV, a signature of M - O and the second one at 533 eV assigned to the SiO_2 substrate. The carbon spectrum shown in Figure 4.17(d) upon deconvolution revealed the adventitious carbon peak at 284.8 eV and two more peaks at higher binding energies, one at 286.51 eV and the second one at 288.79 eV corresponding to C - O and C = O. These results confirmed the existence of MoO_3 and the presence of carbon oxides.

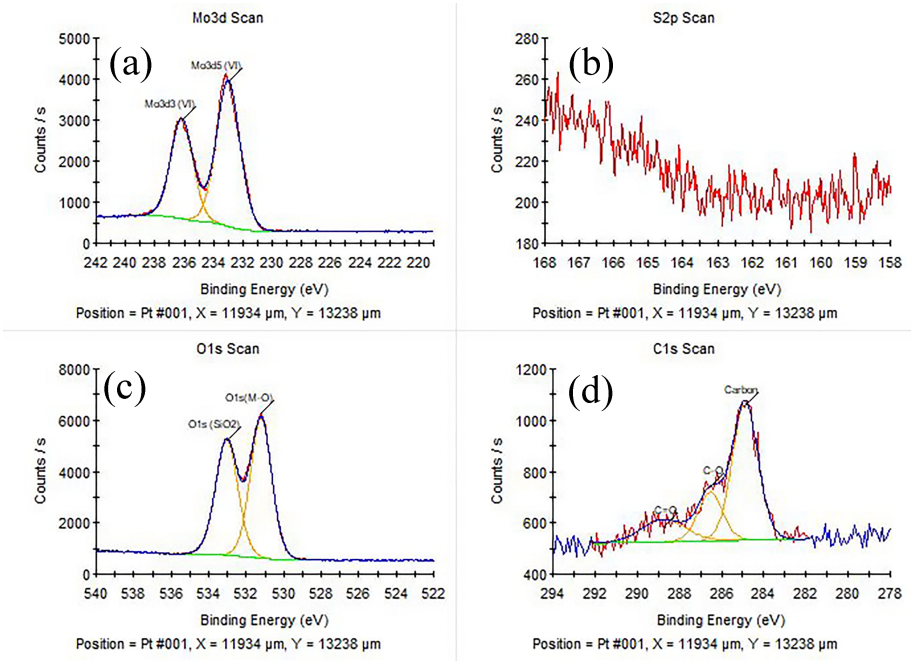

FIGURE 4.17: XPS analysis of the a)Mo3d spectrum for evaluating the oxidation state of molybdenum b) S2p spectrum c) O1s spectrum showing the Si_2 peak molybdenym oxide peak d) C1s spectrum rvealing the adventitious carbon CC-O and C=O peaks

4.4.2 One step sulphurization of MoO_3

The first experiment for the synthesis of MoS_2 was attempted by using a single step sulphurization process using H_2S as the sulphurizing agent. The ALD grown Si / SiO_2 / MoO_3 wafers were diced in 2.5*2.5 cm samples in order to fit a 30 mm quartz tube used for the annealing procedure as the reaction tube. Then for the annealing process the quartz tube was placed in a three zone furnace with the samples positioned at the middle zone. In order to minimize any residual oxygen gas the quartz tube was pumped down to 20 mbar with a 500 sccm flow of pure Argon and brought up to atmospheric pressure by filling it with Argon and pumped down to 3 mbars three times; followed by one hour of Argon purge. The flow of the gases was controlled by mass flow controllers calibrated with a flow rate range of 50 sccm - 500 sccm. After the purging of the tube the temperature controller of the furnace was set to 900 ^{0}C with a 20 ^{0}C / min ramping rate with an Ar flow rate of 200 sccm resulting in a base pressure of 7 mbar. The sulphurization of the thin film started at 700 ^{0}C with the H_2S MFC set at 50 sccm resulting in a total

pressure of 7.7 mbar. In order to fully sulphurize and achieve a high crystallinity order, upon reaching the set temperature a dwell time of 60 min was employed, followed by a natural cooling down in H_2S / Ar environment until the temperature reaching 600^0C when the H_2S flow was stopped. Upon examination of the grown material it became obvious that the film suffered discontinuities. This can be attributed to the sulphurization start temperature where the vapor pressure of MoO_3 (0.1 Torr) resulted in the evaporation of large areas of the deposited film before the sulphurization.The discontinuities can also be explaned by the fact that a byproduct of MoO_3 sulphurization is H_2O that would diffuse thorough the top layers of MoS_2. A second approach shown in Figure 4.18 , by reducing the ramping rate to 10 ^{0}C / min exhibited a smoother film appearance under its examination by optical microscopy but gaps were revealed when characterized by AFM. The third approach implemented was by lowering the onset of the sulphurization temperature at 650 ^{0}C and maintaining the ramping rate at 20^0C min. The lower onset temperature of H_2S gas prevented the MoO_3 thin film from evaporating and produced a continuous thin film, as observed by optical microscopy and AFM measurements.

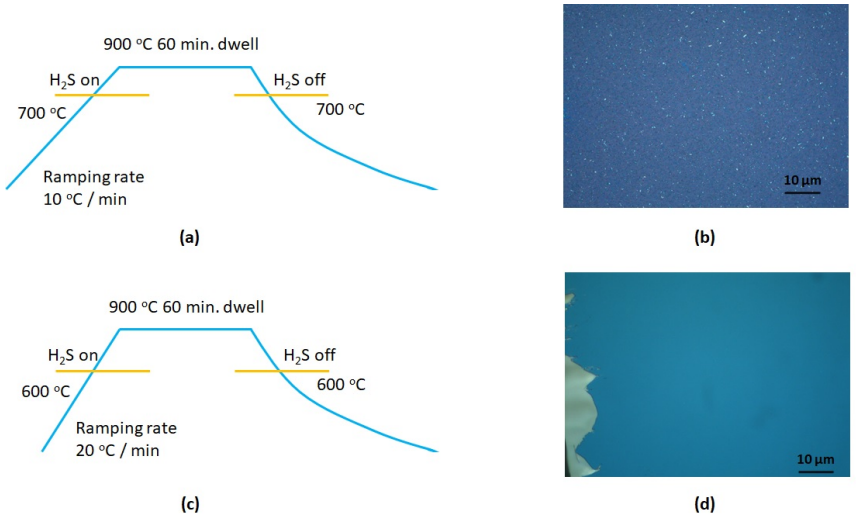

FIGURE 4.18: a)Temperature profile of the second H_2S annealing experiment b) optical microscopy of the annealed film exhibiting discontinuities c) Temperature profile of the third H_2S annealing experiment d) optical microscopy of the annealed film exhibiting a smooth continuus film

The XPS characterization of the film showed minimum oxide content but the drawback was that the stoichiometric ratio of sulphide to molybdenum was 2.1, a result that could possibly hamper the n - type behaviour of MoS_2. The overstoichiometry of the produced film can be attributed to the total amount of the H_2S feed during the annealing protocol which was 5500 sccm corresponding to approximately 7 grams of sulphur. This was a huge ammount of sulphur especially when compared to other CVD techniques where sulphur powder used as precursor is in the range of a few milligrams [71] [72].

4.4.3 Design of experiment for low temperature sulphurization of MoO_3

Design of experiments (DOE) is an experimental approach where in contrast to One Factor At a Time (OFAT), where one experimental factor is tested in one experimental run while the rest are constrained, more than one the factors are changed in order to observe the change to the variables examined. A common DOE design is the full factorial two level design. In this design the experimental factors are set at a high and low level each, producing all the possible combinations of the experimental factors and the high - low set points. The total runs of such a design is 2^k where k are the factors examined.The analysis of the DOE results is executed by the Analysis of Variance (ANOVA) method. This procedure can yield information on the main effects of the experimental factors to the variables as well the interaction of the main effects to the dependent variable.

From the knowledge acquired from the first annealing experiments it became obvious that the total amount of H_2S had to be reduced in order to grow stoichiometric films. A two step annealing protocol had to be devised that would consist of a low temperature H_2S annealing in order to convert the deposited oxide to substoichiometric MoS_2 that would prevent it from evaporating when annealed at higher temperature for further sulphurization and crystallization. A design of experiments (DOE) was implemented in order to evaluate the sulphurization of MoO_3 at low temperatures towards the two step annealing protocol.We chose a three

factor two level half factorial DOE which results in four experimental runs (2^{k-1}). The factors of the experiment were the temperature, the H_2S / Ar flow and time duration of the annealing procedure where the levels used were 550^0C and 650^0C, 50 sccm and 100 sccm, 10 min and 20 min respectively. The design of experiment parameters are listed in Table 4.1. In order to characterize the stoichiometry of the materials grown and the oxidation states present, XPS was used.

TABLE 4.1: DOE generated in Minitab

Run	T (^{0}C)	t (min)	H $_2$S flow (sccm)
1	550	10	100
2	650	10	50
3	650	20	100
4	550	20	50

After placing the samples in the quartz tube and purging as described earlier, when the desired temperature was reached the H_2S flow was started with flow and duration set by the DOE. Finally the system was naturally cooled down to room temperature.After the MoS_2 growth the samples were measured and analyzed by XPS. All the following graphs were charge corrected to 284.8 eV corresponding to the adventitious carbon peak.

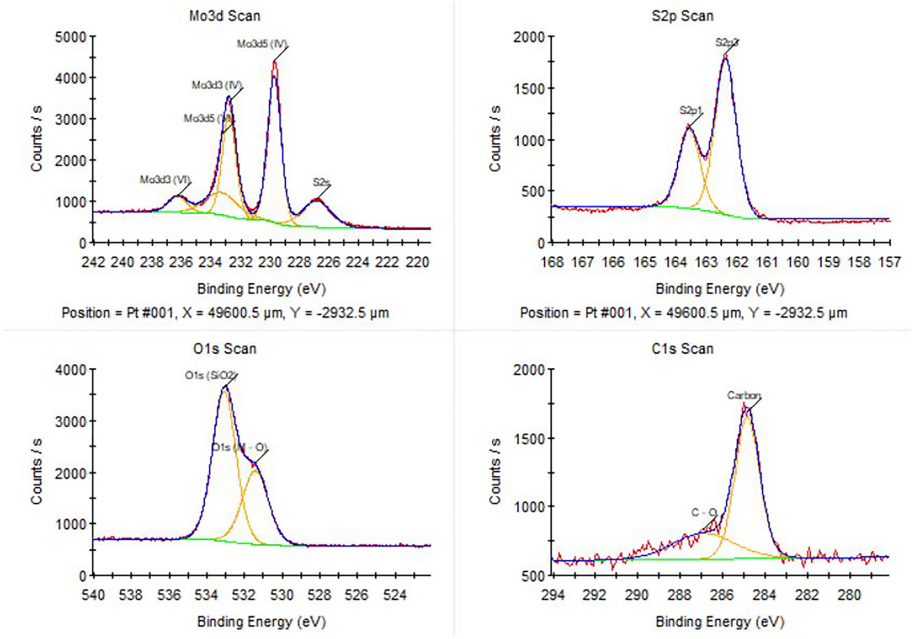

FIGURE 4.19: XPS characterization of MoO_3 annealed at 550^oC for 10 with a 100sccm flow of H_2S

For the first DOE run the sulphurization temperature was set at 550^{o}C with a flow of 100 sccm for H_2S and sulphurization time 10 minutes. The XPS results as shown figure 4.19 upon fitting of the Mo peak revealed the characteristic spin orbit doublet of MoS_2 corresponding to the Mo^{4+} oxidation state at 229.73 eV for the $3d_{5/2}$ and at 232.8 eV for the $3d_3/2$. The S2s peak that is considered as sulphur connected to Mo was found at 226.83 eV. More importantly the Mo3d scan revealed a significant contribution of the Mo^{6+} oxidation state that is ascribed to the existence of MoO_3 in the MoS_2 film. The $3d_{5/2}$ of the Mo^{6+} state was found at 233.31 eV and the $3d_{3/2}$ at 236.31 eV. Next the S2p components where deconvoluted in two peaks, the $S2p_{3/2}$ found at 162.36 eV and the $S2p_{1/2}$ at 163.55 eV. These peaks are of high importance for the determination of the stoichiometric ratio of molybdenum to sulphur by calculating the ratio of these peak areas to the peak areas of the Mo^{4+} oxidation state doublet. In that way the produced film exhibited a substoichiometric ratio of S:Mo = 1.66. It should be noted that the same procedure could be followed by using the S2s peak instead of the S2p and the $3d_{5/2}$ but this was avoided due to their overlapping, resulting in an overestimation of the stoichiometry that in this case was found to be S:Mo = 1.98. As expected from the high content of oxide in the Mo3d spectrum, oxide peaks were also found in the oxygen and carbon spectra. For the O1s spectrum the most intense peak was found at 533 eV corresponding to SiO_2. After deconvolution a shoulder peak at 531.4 eV was found that confirms the existence of M - O. The C1s peak also revealed, after the deconvolution, the existence of C - O at 286.9 eV beside the adventicious carbon at 284.8 eV. Summarizing for this run substoichiometric MoS_2 was grown with high MoO_3 content but more importantly the existence of C - O in both the oxygen and carbon spectra revealed the partial reduction of the deposited oxide film. Appendix A.1 is presenting the rest of the DOE XPS deconvolutions. Table 4.2 represents the stoichiometry ratios of molybdenum to sulphur, oxygen to sulphur, the binding energy of the Mo3d(5/2) and its FWHM for all the DOE runs.

All the annealing experiments resulted in stoichiometries ranging from $1.618 - 1.662$ making obvious that the flow rate is of no significance but the total amount

TABLE 4.2: DOE XPS results

Run	S : Mo	Mo(VI) : S2p (%)	B.E. (ev)	Mo3d(5/2) FWHM (ev)
1	1.62	15.19	229.73	1.08
2	1.66	12.4	229.77	1.04
3	1.67	9.94	229.78	0.98
4	1.62	17.44	229.59	1.07

of the H_2S provided during the annealing. Nevertheless the lower S:Mo ratios were exhibited by the samples annealed at lower temperatures, namely Run 1 and Run 4 a result that implies that the reaction is slower for lower temperatures within the window of parameters used for the DOE. The molybdenum oxide content of the films was estimated by calculating the ratio of the MO(VI) doublet peak area to the S2p doublet peak area. The oxide content was found to be between 9.94% - 17.44% with the lowest concentrations for the samples annealed at high temperature. The binding energy of Run 4 sample exhibited a large shift to a lower binding energy at 229.59 eV. This shift can be attributed to the Fermi level moving towards the valence band due to hole doping of the MoS_2 from the MoO_3. The Fermi level is the reference for the core levels found in XPS, so $n-$ type MoS_2 core peaks appears in higher binding energies than $p-$ type [36]. Lastly the third sample that showed the highest S: Mo ratio and the lowest oxide content as expected exhibited the smallest FWHM of the $Mo3d_{5/2}$ indicating a low degree of crystal disorder. Figure 4.20 shows the contour plot of of the S : Mo to Temperature where it can be seen that the stoichiometry increases upon temperature increase with no significant contribution from the H_2S / Ar flow. Figure 4.21 represents the reduction of the molybdenum oxide in MoS_2 with the main effect being the increase of temperature but unlike the stoichiometry results H_2S / Ar flow has an effect as it can be observed that for higher ratios of H_2S flows at the same temperature the MoO_3 percentage is lower.

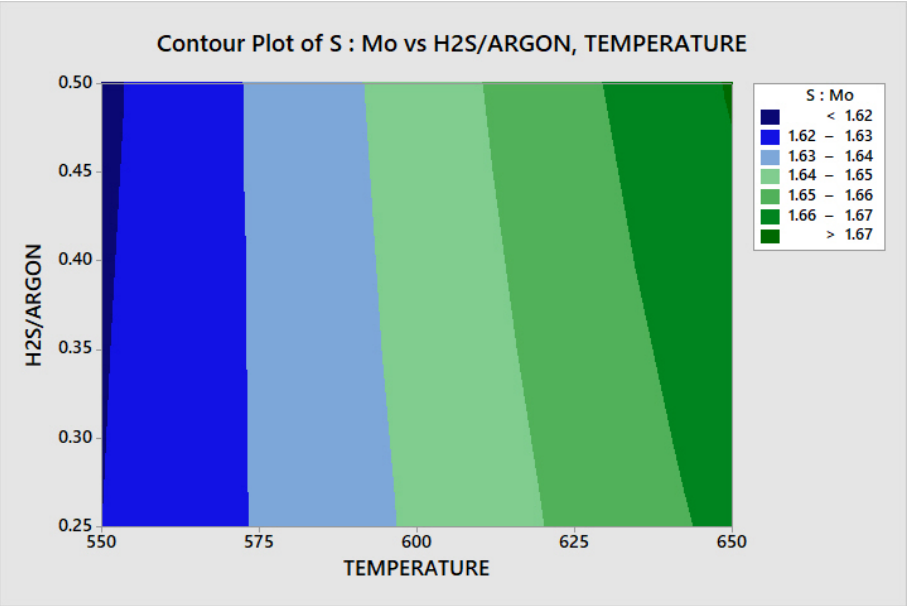

FIGURE 4.20: Contour plot of S : Mo

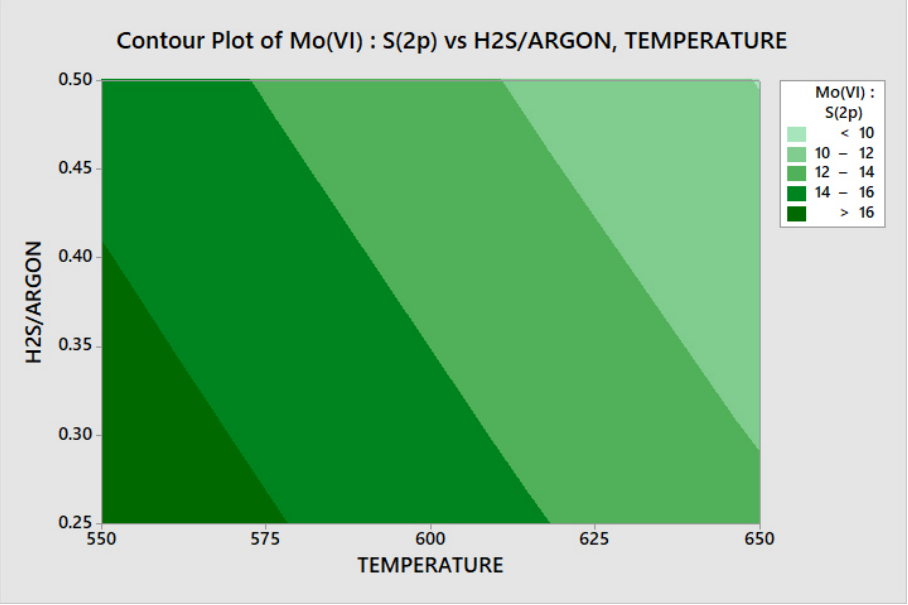

FIGURE 4.21: Contour plot of Mo(VI) : S2p

Finally all the DOE samples were characterized by Raman spectroscopy with typical in plane and out of plane vibration modes resolved but more interestingly two more intense peaks appeared, one at 189 cm^{-1} and one at 228 cm^{-1} making obvious the high content of molybdenum oxide in the film [71].

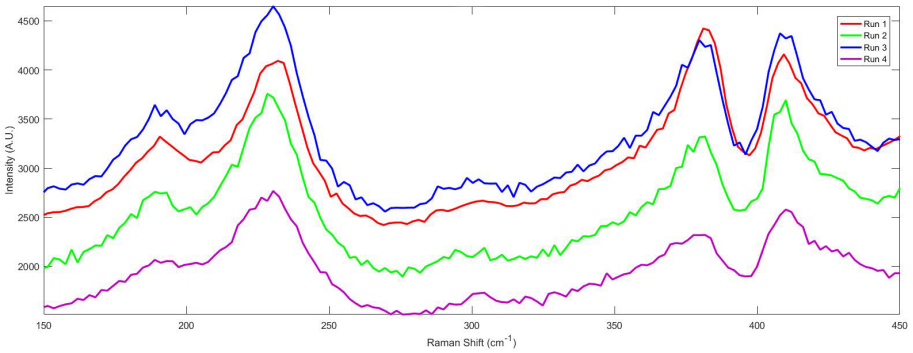

FIGURE 4.22: DOE Raman characterization

4.4.4 Multistep annealing of MoO_3

The DOE for eliminating the molybdenum oxide content in MoS_2 at low temperatures proved to be insufficient while the S : Mo stayed at low values within the parameters used. For that reason a new set of experiments was conducted at lower H_2S and Ar flows controlled by a flow meter at 10 sccm for H_2S .

The first round of annealing experiments was held in order to evaluate the molybdenum oxide content in the grown films at 600 ^oC at 6, 10 and 19 min.The samples were inserted as in the quartz tube and the tube was purge with Ar as described before. After purging, the argon flow was set at 70 sccm resulting in base pressure of 3.6 mbar. Upon reaching 600 ^oC the H_2S flow started at 10 sccm resulting in 3.7 mbar total pressure. The stoichiometry of the films were analyzed by XPS, Figures 4.23, 4.25,4.27 while Raman characterization was implemented for determining the number of layers and the crystallinity by extracting the FWHM of the E2g mode Figures 4.24,4.26,4.28. This protocol resulted with higher MoS_2 stoichiometries than those obtained with the DOE, within the range of $1.85 - 1.87$ and substantially decreased oxide content of $7.23\% - 8.76\%$. Nevertheless the $Mo3d_{5/2}$ B.E. appeared at low energies. Summary of all the results are included in Table 4.3

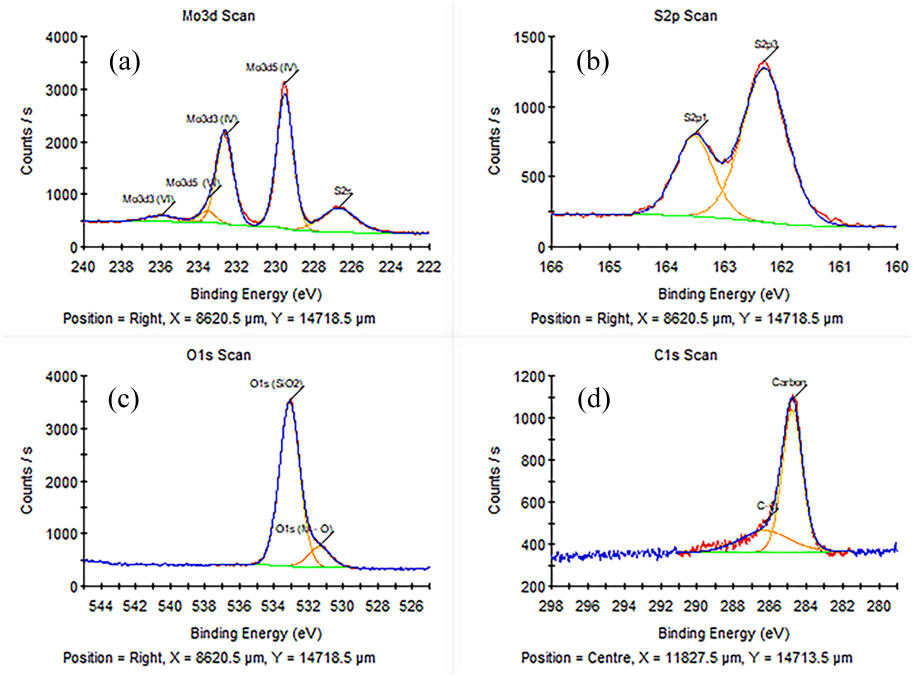

FIGURE 4.23: XPS characterization of MoO_3 annealed at 600^{o}C for 6 min a)Mo3d scan b)S2p scan c)O1S scan d) C1s scan

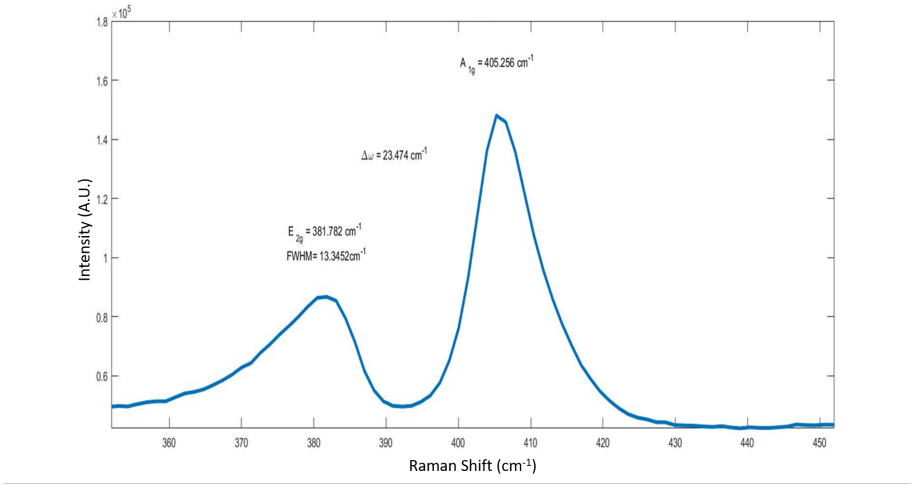

FIGURE 4.24: Raman characterization of MoO_3 annealed at 600^{o}C for 6 min

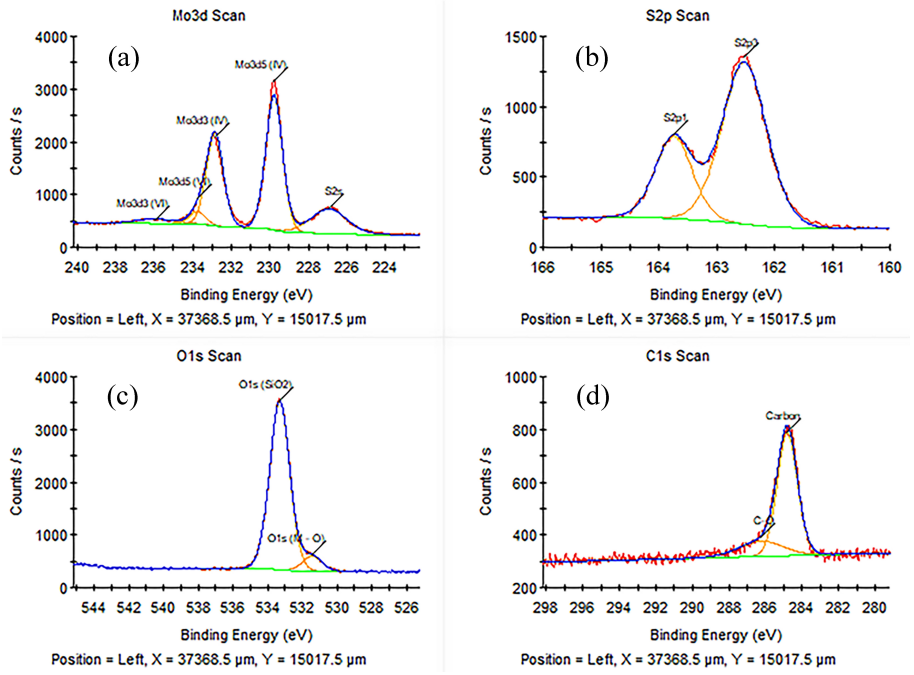

FIGURE 4.25: XPS characterization of MoO_3 annealed at 600^{o}C for 10 min a)Mo3d scan b)S2p scan c)O1S scan d) C1s scan

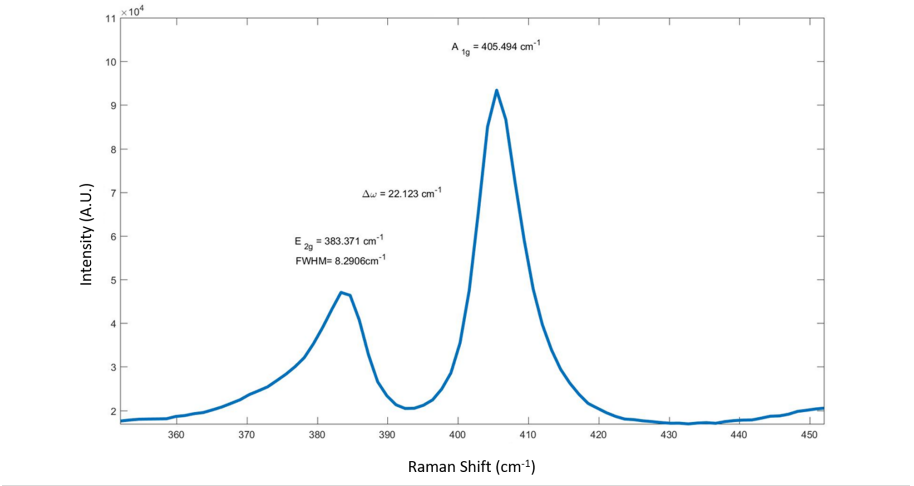

FIGURE 4.26: Raman characterization of MoO_3 annealed at 600^{o}C for 10 min

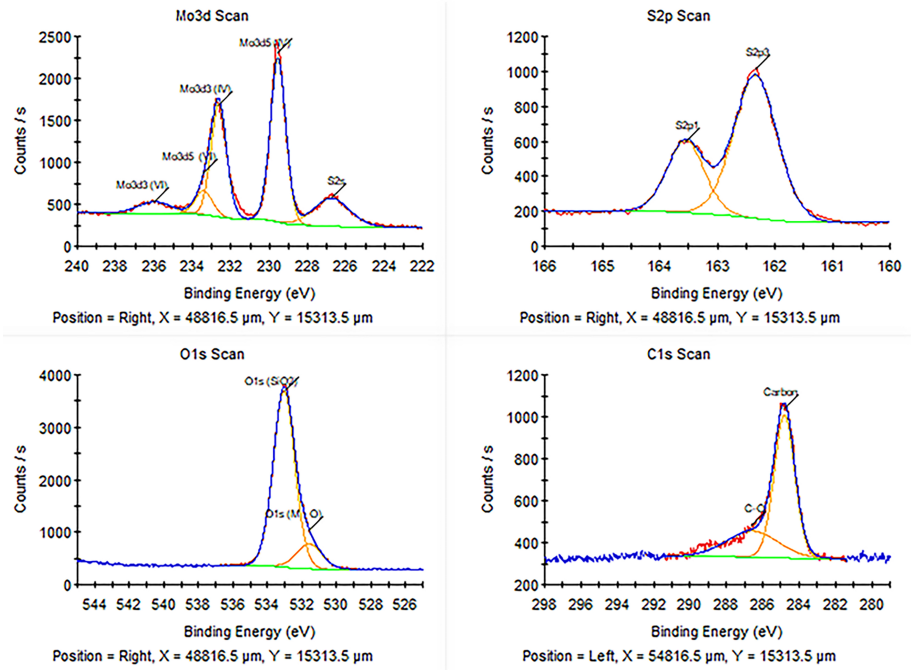

FIGURE 4.27: XPS characterization of MoO_3 annealed at 600^{o}C for 19 min a)Mo3d scan b)S2p scan c)O1S scan d) C1s scan

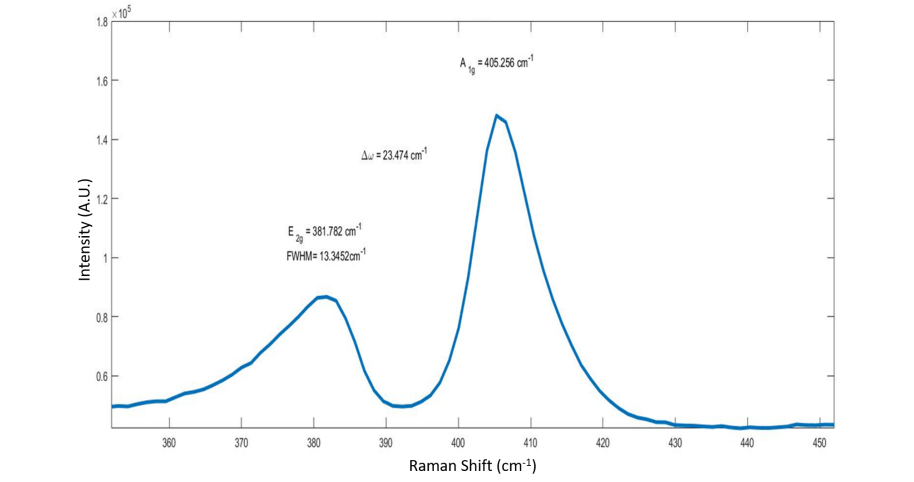

FIGURE 4.28: Raman characterization of MoO_3 annealed at 600^{o}C for 19 min

TABLE 4.3: One step annealing protocols characterization results

Annealing protocol	One step annealing	One step annealing	One step annealing
Temperature / Time	600 ^{o}C / 6 min	600 ^{o}C/ 10 min	600 ^{o}C / 19 min
Mo at%	35.1	34.82	35.07
S at%	64.9	65.18	64.94
S : Mo ratio	1.84	1.87	1.85
Mo 6+ / S2p	8.76	7.48	7.23
Mo 3d5/2 B.E.	229.58	229.61	229.55
E2g FWHM	12.7	13.3	8.29

In the next set of experiments three multi step annealing protocols were used in order to enhance resulting stoichiometry and crystallinity of the film. The total time of annealing in H_2S environment was kept constant at 19 min for all the experiments. In the first annealing protocol two steps were used. One step at 600^{o}C for 15 min and a second one at 900 ^{o}C for 4 min. During the ramping up to the high temperature set point only Ar flow was present. This protocol resulted from the deconvolution of Figure 4.29 in a stoichiometry of 1.98 but with an unexpected high molybbenum oxide percentage of 9.35% which was higher than the ones in the one step low temperature annealing protocols.This was attributed to incorporation of residual oxygen in the annealing tube into the grown MoS_2 film during sulphurization at high temperature. The second annealing experiment was carried out in order to validate this assumption. A two step annealing procedure at 600^{o}C and a lower temperature of 800^{o}C was implemented where the time of annealing for the first step was reduced to 10 min and the second step time increased to 9 min. This protocol resulted in a lower oxide percentage of 5.27% and stoichiometry of 1.91 as seen in Figure 4.31. Finally a third protocol with the same parameters as the second protocol was implemented with an additional third step of annealing at 900^{o}C in Ar environment for further crystallization of the film with out influencing its stoichiometry. The XPS deconvolution seen in Figure 4.33 resulted in the exact same stoichiometry as the second annealing protocol validating that annealing at a sulpur deficient environment at 900^{o}C there was no

sulphur loss. Due to the high annealing temperature though the oxide content was risen again to 7.7% and resulted in the same crystallinity order achieved from the first annealing protocol with the E_{2g} FWHM at 7.7 cm^{-1}. Summary of the XPS and Raman characterizations of the multi step protocols are presented in Table 4.4

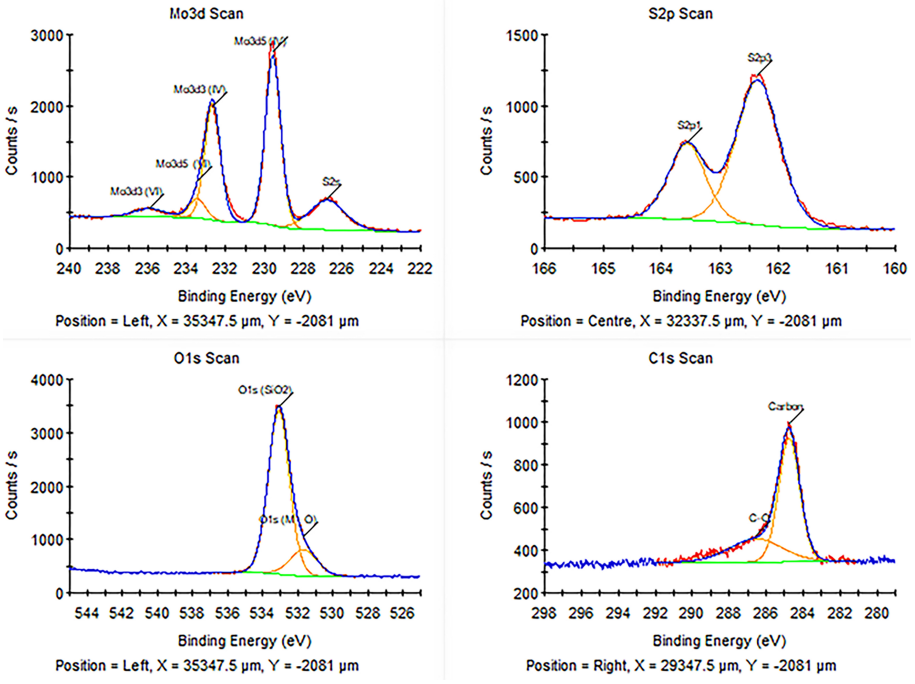

FIGURE 4.29: XPS characterization of MoO_3 annealed at 600^{o}C for 15 min and at 900^{o}C for 4 min a)Mo3d scan b)S2p scan c)O1S scan d) C1s scan

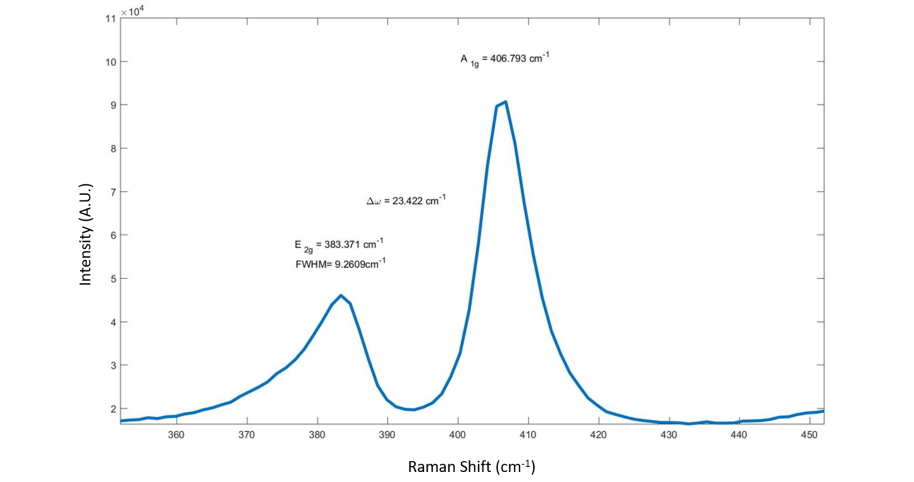

FIGURE 4.30: Raman characterization of MoO_3 annealed at 600^{o}C for 15 min and at 900^{o}C for 4 min

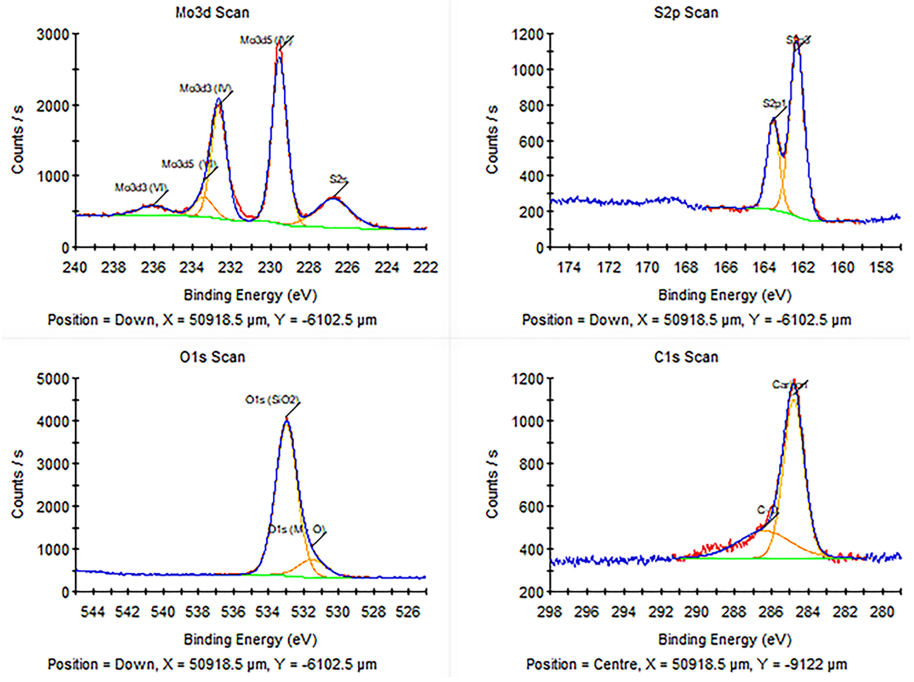

FIGURE 4.31: XPS characterization of MoO_3 annealed at 600^{o}C for 10 min and at 800^{o}C for 9 min a)Mo3d scan b)S2p scan c)O1S scan d) C1s scan

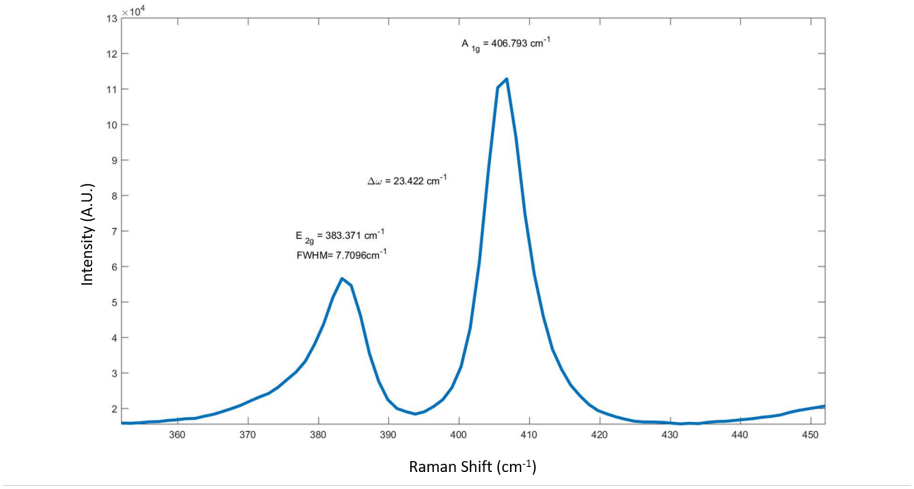

FIGURE 4.32: Raman characterization of MoO_3 annealed at 600^{o}C for 10 min and at 800^{o}C for 9 min

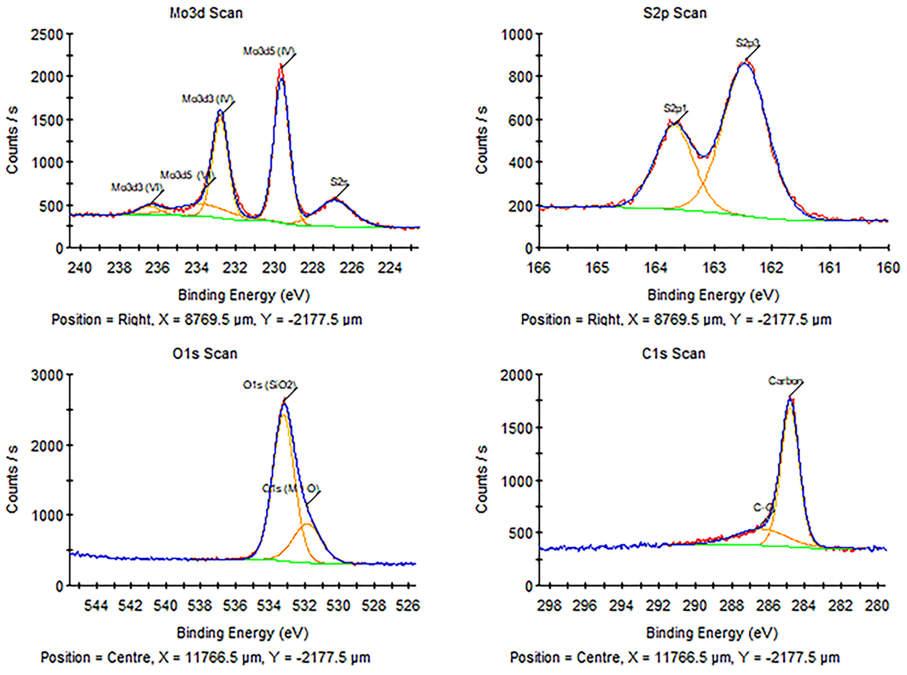

FIGURE 4.33: XPS characterization of MoO_3 annealed at 600^{o}C for 10 min, 800^{o}C for 9 min and 900^{o}C for 10 min in Ar environment a)Mo3d scan b)S2p scan c)O1S scan d) C1s scan

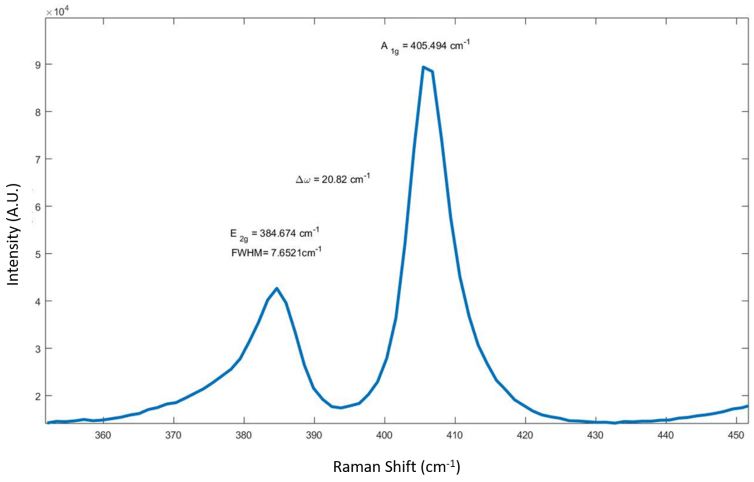

FIGURE 4.34: Raman characterization of MoO_3 annealed at 600^{o}C for 10 min, at 800^{o}C for 9 min and in Ar environment for 10 min at 900^{o}C

TABLE 4.4: Characterization results of multi step annealing protocols

Annealing protocol	Two step annealing	Two step annealing	Three step annealing
Step no. Temperature / Time	Step 1. 600 ^{o}C / 15 min Step 2. 900 ^{o}C / 4 min	Step 1. 600 ^{o}C / 10 min Step 2. 800 ^{o}C / 9 min	Step 1. 1.600 ^{o}C / 10 min Step 2. 2.800 ^{o}C / 9 min Step 3. 3.900 ^{o}C / 10 min
Mo at%	33.51	34.35	34.31
S at%	66.49	65.65	65.69
S : Mo ratio	1.98	1.91	1.91
Mo 6+ / S2p	9.35	5.27	7.9
Mo 3d5/2 B.E.	229.64	229.58	229.54
E2g FWHM	7.65	9.2	7.7

The final set of annealing protocols presented in Table 4.5 was implemented in order to achieve slightly more substoichiometric MoS_2 films within acceptable 2H n - type phase [119] [36] while further reducing the persistent molybdenum oxide. The first protocol was set for a 10 min annealing at 600^{o}c and a second step at 800^{o}c for 4 min to ensure a good stoichiometry. This resulted in S : Mo ratio of 1.846 and 6.66 % content of molymbdenum oxide. For the second protocol the same parameters were used followed by quench instead of letting the samples cool down naturally. This protocol presented a small increase of the produced

film stoichiometry and for the first time the content of the molybdenum oxide was decreased to 3.25 % resulting in a binding energy of $Mo3d_{5/2}$ of 229.91, values consistent with n - type MoS_2 [120] [36]. Figures 4.35, 4.37 show the deconvolutions for the two annealing protocols where the reduction of the molybdenum oxides can be clearly seen. In Figures 4.36, 4.38 the Raman spectra for the two protocols are presented where the FWHM of E_{2g} of the quenched sample appears to be larger due to the fast cooling of the sample. The emergence of photoluminescence for high temperature annealing can be seen in 4.39 providing evidence for the high quality MoS_2 film.

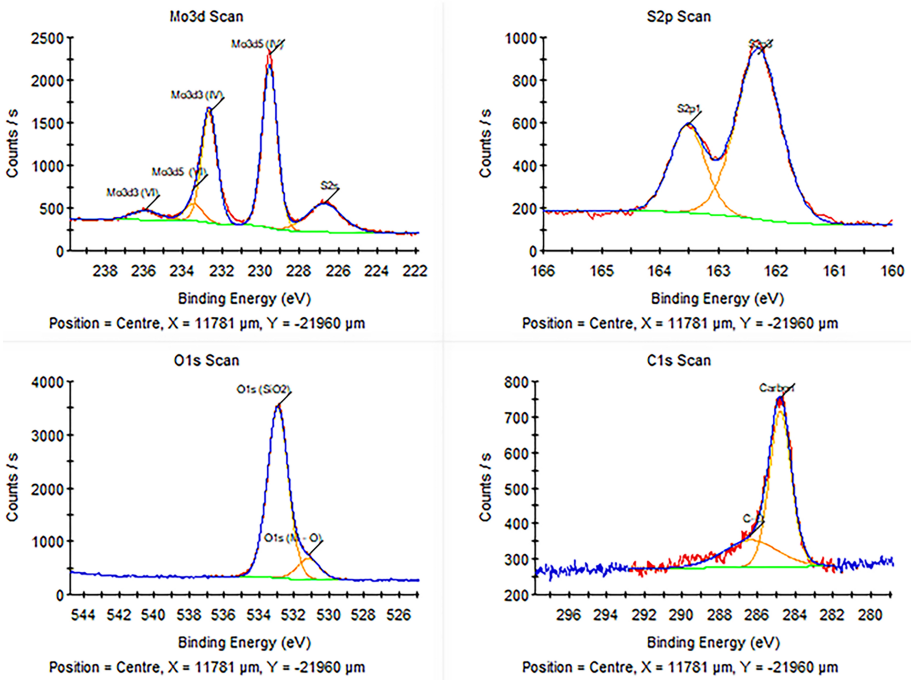

FIGURE 4.35: XPS characterization of MoO_3 annealed at 600^{o}C for 10 min, 800^{o}C for 4 min a)Mo3d scan b)S2p scan c)O1S scan d) C1s scan

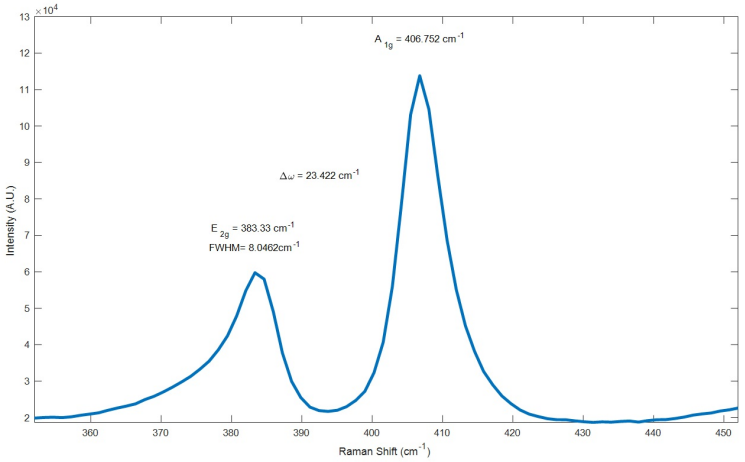

FIGURE 4.36: Raman characterization of MoO_3 annealed at 600^{o}C for 10 min, at 800^{o}C for 4 min

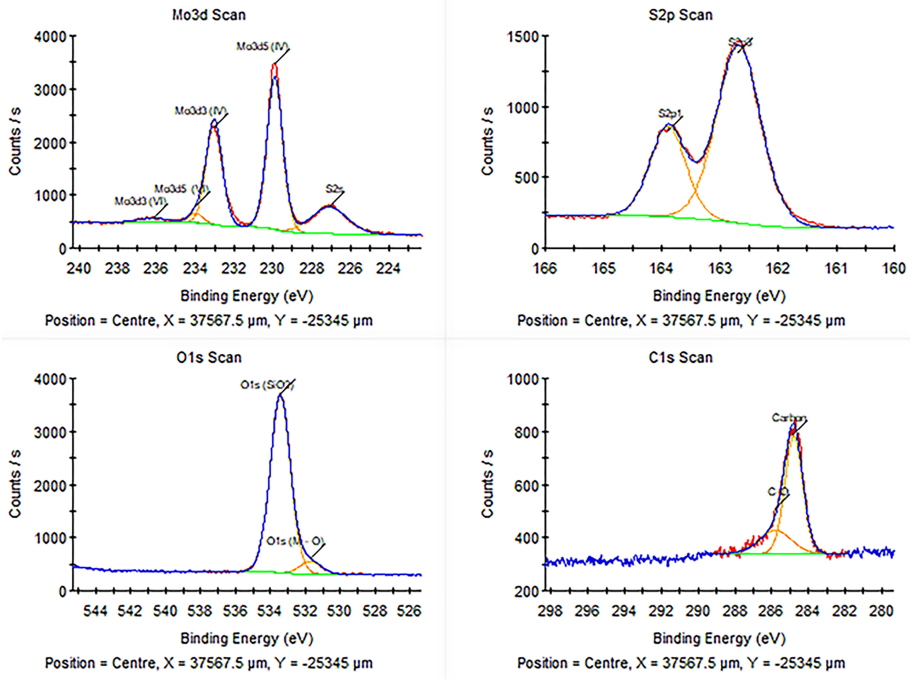

FIGURE 4.37: XPS characterization of MoO_3 annealed at 600^{o}C for 10 min, 800^{o}C for 4 min and subsequently quenched a)Mo3d scan b)S2p scan c)O1S scan d) C1s scan

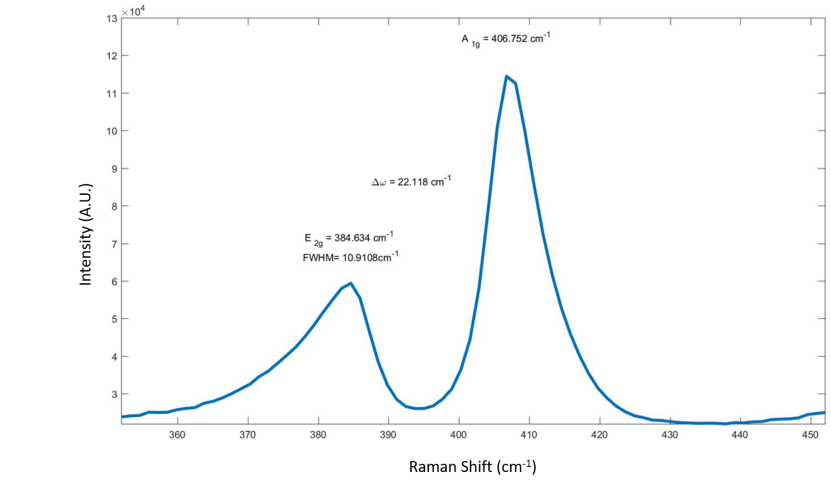

FIGURE 4.38: Raman characterization of MoO_3 annealed at 600^{o}C for 10 min, at 800^{o}C for 4 min and subsequently quenched

TABLE 4.5: Characterization of two step annealing vs quenched two step annealing protocol

Annealing protocol	Two step annealing	Two step annealing
Step no. Temperature / Time	Step 1. 600 ^{o} / 10 min Step 2.800 ^{o} / 4 min	Step 1. 600 ^{o} / 10 min Step 2.800 ^{o} / 4 min Quench
Mo at%	35.13	34.84
S at%	64.87	65.17
S : Mo ratio	1.84	1.87
Mo 6+ / S2p	6.86	3.25
Mo 3d5/2 B.E.	229.55	229.91
E2g FWHM	8	10.9

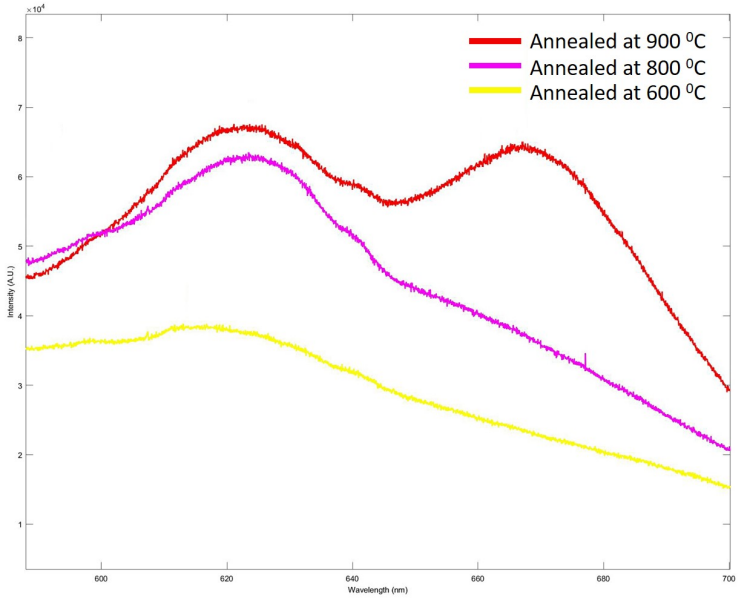

FIGURE 4.39: Photoluminescence evolution

4.5 Conclusion

This chapter has presented the growth of 2D materials including graphene, HfS_2 and MoS_2 via CVD and ALD followed by thermal vapour sulphurization techniques for the graphene, HfS_2 and MoS_2 respectively. Graphene LPCVD growth was investigated by employing CH_4 gas and H_2 gases. An optimization process of the CVD growth was tailored by analyzing the Raman spectra of the grown films under different pressures, gas ratios and temperatures by examining the 2D/G peak ratios in order tho validate the successful growth of monolayers and the ratio of the D/G peak was monitored for the quality of the grown films. The optimum conditions of the CVD growth were found for a gas ratio of 100 sccm / 210 sccm for H_2 / CH_4 at 20mbar and temperature of 900^0C which resulted in monolayer growth and minimum defects. HfS_2 was deposited via CVD by employing the hafnium containing precursor $HfCl_4$. After validating the thermodynamical feasibility of the reaction between the precursor and H_2S CVD was employed by using a three

zone furnace where the precursor was loaded in an injection tube in the first zone at 175^0C providibg adequate vapour pressure and Si /SiO_2 substrates were loaded in the third zone at 850^0C. The pressure of the deposition was kept at 20 mbar at a constant flow of 50 sccm of H_2. The grown films were characterized by Raman spectroscopy and photoluminescence measurements where it was found that the successful deposition of the material was accompanied by shifts of the two Raman modes of the material. Further examination of the as grown films revealed the existence of bend upward cracks. Finally MoS_2 was grown by first growing ultrathin MoO_3 thin films by ALD. The grown oxide was characterized by XPS and annealed in low pressure in H_2S environment. Different sulphurization processes were investigated in order to obtain a high quality highly crystalline grown film with different stoichiometries by characterizing the films with XPS spectroscopy Raman and photoluminescence measurements.

Chapter 5

Fabrication and characterization of wafer scale 2D TMDC FETs and heterostructures

5.1 2D FET fabrication tools and process

5.1.1 Photolithography

Photolithography is used in order to transfer geometric shapes that are etched on a photomask to the surface of a sample by exposure a photoresist to a light source of a certain wavelength. Thus the first step of the photolithography process, is the spin coating of a photoresist onto the sample−wafer in order to form a thin film with uniform thickness. Then the photomask is placed between the light source and the photoresist layer. The wavelength of the light source is usually UV or beyond UV wavelength DUV or EUV. Next step is the development where the photomasks pattern or the inverse is imprinted on the sample. There are two kinds of photo resists: positive and negative. For a positive resist, when the resist is exposed its chemical structure changes becoming so more soluble in its developer. The developer removes the resist on the exposed areas. The negative resist

behaves in an opposite manner. When the negative resist is exposed these regions are polymerized and do not dissolve in the developer. The developer only removes resist on the unexposed regions. A typical photolithography process is consisted by the following steps: 1. Wafer cleaning (cleaning of organic and inorganic contaminations) 2. Wafer baking. (removing moisture) 3. Primer coating. (coating the wafer with a primer for promoting photoresist adhesion) 4. Photoresist coating. (coating the surface with a photoresist layer) 5. Soft baking. (removing remaining solvents from the photoresist) 6. Mask alignment. (aligning the patterns on the mask to the wafer) 7. Exposure. (exposing the resist to the desired wavelength 8. Development. (removing unwanted areas of resist by the developer) 9. Hard baking. (hardening the photoresist to improve the adhesion to the wafer)

5.1.1.1 Photolithography process

Photolithography was used during the process fabrication in four stages.The first stage was for defining masked areas for the subsequent etching of the semiconducting 2D channels. The second stage was for defining source and drain areas for the FET, where the metals of choice would be deposited.The third photolithography step was used in order to define areas for the deposition of the top gate metal and the last photolithography step was for defining areas for via holes in order to have direct access at the source drain metals after the top dielectric deposition.

Before finalizing the photolithography protocol for the etching step a number of different photoresists were used including the MICROPOSIT S1800 series and the AZ nLOF 2000 Series. Both series where proved to be a poor choice for TMDCs as it can be observed in figure 5.1 because of issues that arised during the development stage. The developers for both series are H_2O − alkaline based mixtures that were interacting with the TMDCs lifting them off from the substrate resulting in poor yield and overall degradation of the devices. For that reason an alternate photolithography solution was devised for the photolithography steps that the developer would come in touch with the TMDC material,namely, masking

for etching, source and drain patterning.No relative issues were observed for the graphene fabrication.

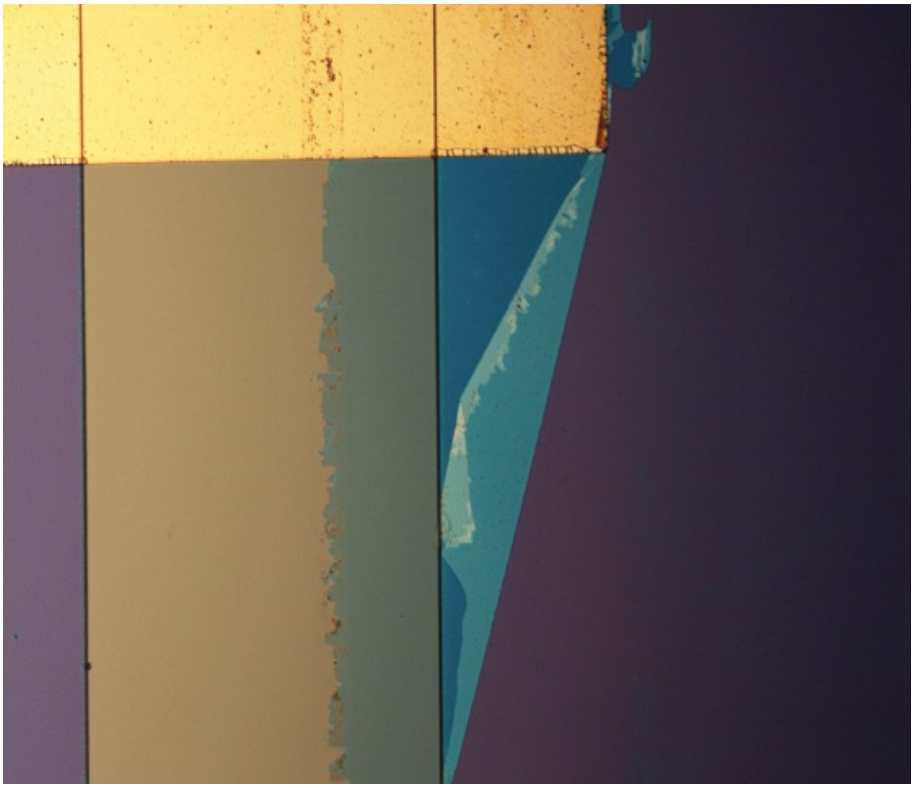

FIGURE 5.1: Optical microscopy of MoS_2 delaminated from the substrate
.

5.1.1.2 Bilayer photolithography

For the photolithography patterning of TMDCs a bilayer photoresist protocol was employed using as a first layer the positive tone S1813 and as an overlayer the negative tone $SU8-2$. $SU8-2$ photoresist is developed by an organic compound that instead of the water alkali mixture of S1813 and AZ series. Nevertheless SU8 is very difficult to be developed and stripped off as it is heavily crosslinked during the fabrication steps. For that reason S1813 was used as an under layer. After exposure the unexposed areas of SU8 are developed in EC solvent and the exposed S1813 is dissolved both in the vertical and lateral direction providing an excellent undercut shown in figure 5.2 that is also useful for the metal $lift-off$ after the metal deposition. In summary the TMDC sample is heated on a hot plate to remove the humidity from it's surface in order to promote adhesion of the photoresist. After cooling the sample S1813 is spin coated and baked at 110^0C for one minute. Two minutes later the SU8 photoresist is spin coated and baked. The baking prorocol is one minute at 60^0C then immediately one minute at 105^0C and finally one minute at 60^0C. This multistep heating protocol was followed in order to avoid stress developed and cracks at the photoresist layers due to different themal expansion coefficients. After the sample is cooled at room temperature it is exposed under UV radiation and finally the same three step heating protocol is used to hard bake the photoresist followed by the development.

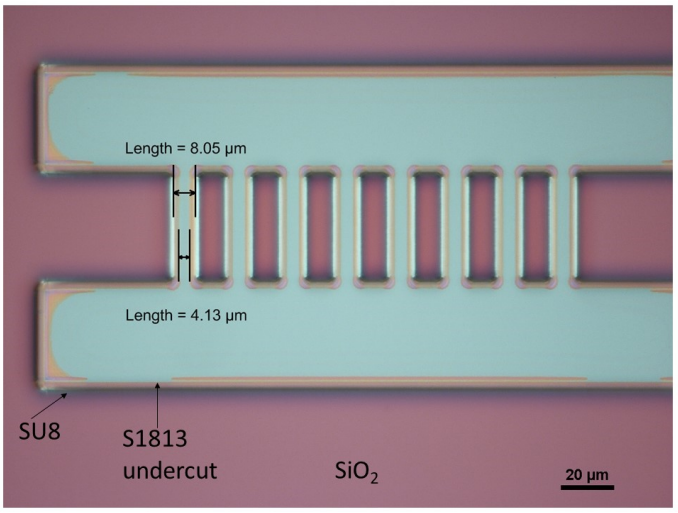

FIGURE 5.2: SU8 S1813 bilayer protocol photolithography with an undercut of 4μm

.

5.1.2 Reactive ion etching

Reactive Ion Etching (RIE) is a dry etching technique that is used in order to selectively remove materials. RIE is a dry etching technique that is based on a number of physicochemical processes occurring in an ion plasma environment. With the use of a reactive plasma, high − energetic ions of the plasma interact with the material to be processed, chemically reacting with it and removing it. In order to create an ion plasma vacuum and an electromagnetic field is applied. The ion plasma is generated in vacuum by applying an electromagnetic field. A RIE system consists of a vacuum chamber that contains a set of different substrate holders to be used that are inert to the different gases that are used, an RF power source that produces the plasma by breaking the gas molecules into ions and a pump for reaching the desired pressure.

5.1.2.1 Reactive ion etching process

For creating semiconducting channels of MoS_2 RIE was used in order to selectively remove the material. It was found that after the RIE process a large number of patterned devices where left with hardened photoresist residues covering them with

thicknesses of a few nanometers deteriorating their electrical properties. Because of the two dimensional thickness of the materials, plasma ashing, a standard step for typical semiconductor processes was not a viable solution, for that reason the samples where left in NMP overnight to increase the number of devices that were free of residues.

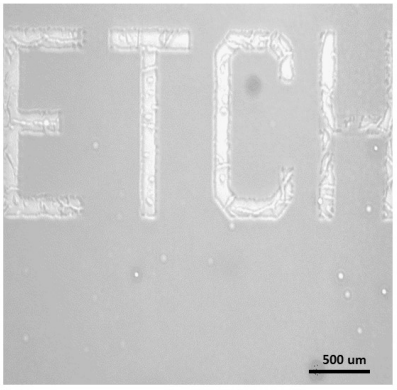

FIGURE 5.3: Hardened residues of photoresist after SF6 etching process

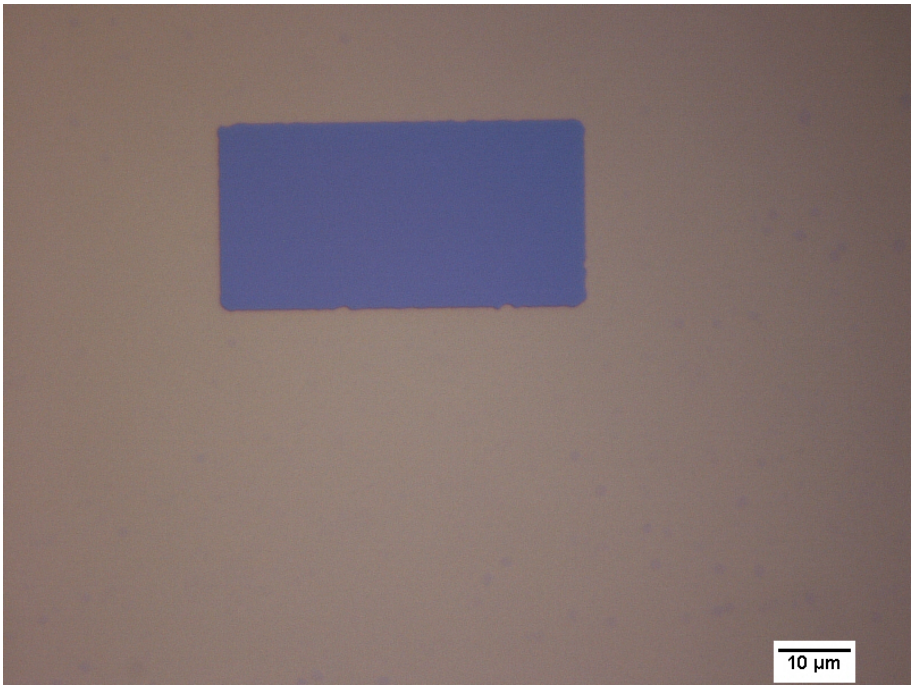

FIGURE 5.4: Successful lift off of the photoresist after CHF_3 etching process

Two different protocols were used. The first protocol used for the etching of MoS_2 used a mixture SF_6 / Ar (20 sccm /5 sccm) at 50 mTorr with a forward RF power of 80 watts for 45 seconds. The second protocol involved a mixture of CHF_3 / O_2 35 / 15 at 300 mTorr a fowrard power of 80 Watt for 1 min. The higher pressure and the addition of the oxygen gas in the process was followed in order to reduce the fluorocarbons that hardened the photoresist. Figure 5.3 shows the results of the etching process for the SF6 chemistry and 5.4 shows the complete lift off of the photoresist after the CHF3 / O_2 etching.

5.1.3 Oxide encapsulated MoS_2 fabrication

After the sulphurisation of the films the chips were processed to create dual-gate transistors as shown in the schematic diagram of Figure 1. First a 10 nm of Al_2O_3 layer was deposited by ALD employing the precursor Trimethylaluminum (TMA) and ozone by a process of 100 cycles of 150 msec O_3 pulses and 15 msec pulses of TMAon.The grown alumina layer acts as a protection layer preventing any alkaline solution from the subsequent development to come in contact with the MoS_2 while at the same time protecting the film from oxidation and contamination. The channels of the transistors were patterned using S1813 as a photoresist and MF319 as a developer. The positive tone resist process is as follows: 1. 30 minutes drying in a 200^0C oven, 2. 5 minutes cool down, 3. spin S1813 at 6000rpm for 30 seconds, 4. bake at 115C for 1 minute, 5. expose in 40 mJ / cm^2 UV (using EVG 6200 without a filter) 6. develop in MF 319 for 30 seconds 7. Rinse in DI water and dry with nitrogen gun. The next step involves the removal of the alumina from the exposed areas in order to etch the MoS2 in FET channels. As MoS_2 is inert in short HF runs the samples were dipped in HF 20:1 for 25 seconds to remove the exposed alumina. (The 25 seconds had been calibrated for overetching the 10nm alumina by 10%). The channels were finally patterned using a variety of process with different advantages and disadvantages. Ion Beam etching (IBE) offered a very rapid and accurate etching with the advantage that it can also etch remaining alumina. The disadvantage of IBE is that it overly crosslinks the photoresist so it

makes it hard for removal. The weak reactive ion plasma process based on CHF_3 and O_2 offered an easier to remove layer with excellent etching results. Finally, a wet method was used were the chips were dipped in fuming Nitric Acid for 10 seconds. The advantage of this process is that it rapidly removes the MoS2 without affecting the oxide under it while at the same time removing the unwanted photoresist. Such a process can be less favourable for mass production as the that would create a variable undercut on a wafer scale. For the dry processes photoresist was removed in N-methyl pyrolidone (NMP) at 80^oC in 2 hours. Working devices were obtained from all 3 etching processes.Figure 5.5 presents the fabrication step before the MoS_2 etching.

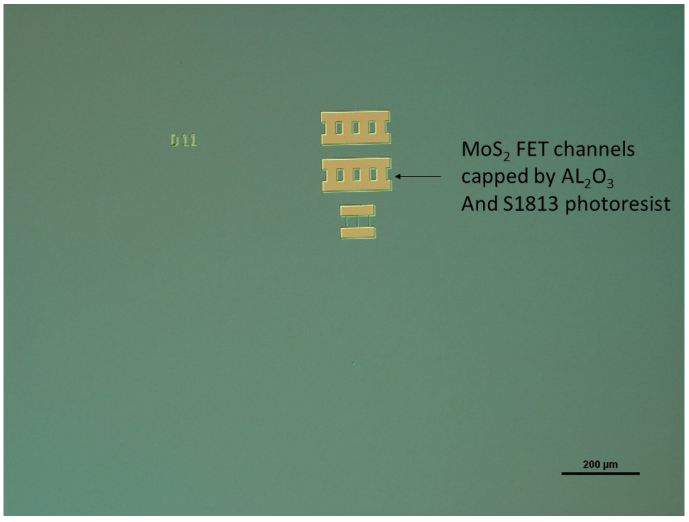

FIGURE 5.5: Optical microscopy of the process step before MoS_2 etching

The next step was to transfer the pattern of the metal electrodes. This was performed using AZ 2070 as a photoresist and AZ 726 MIF as the developer. The negative tone resist process is as follows: 1. 30 minutes drying in a 200^0C oven, 2. 5 minutes cool down, 3. spin AZ 2070 at 5000rpm for 30 seconds, 4. bake at 110^0C for 1 minute, 5. expose in 90 mJ / cm^2 UV (using EVG 6200 with i-line filter) 6. post-bake at 110^0C for 1 minute 7. develop in AZ 726 for 45 seconds 8. Rinse in DI water and dry with nitrogen gun.Alumina was removed from the contact points using the same 20:1 HF 25 seconds etch that was used for the channels. A layer of 5 / 150nm Ti / Au was sputtered. The metal pattern was lift-off at 80^0C in N-methyl pyrolidone (NMP) in a magnetically stirred bath in 2 hours. The

remaining alumina was removed from the channels using buffered 20:1 HF (25sec in 20:1 HF) and the backside oxide was etched by RIE (3min10sec, 34 sccm Ar, 16 sccm CHF3, 30mTorr, 200 W, 20^0C).Figure 5.6 presents the photolithography metal patterns on a number of FET devices and figure 5.7 presents the devices after the metal deposition. Figure 5.8 the final photolithography process using the photoresist SU8 3000 in order to fabricate wells at the FET regions for isolating the rest of the device coming in contact with liquids during wet measurements.

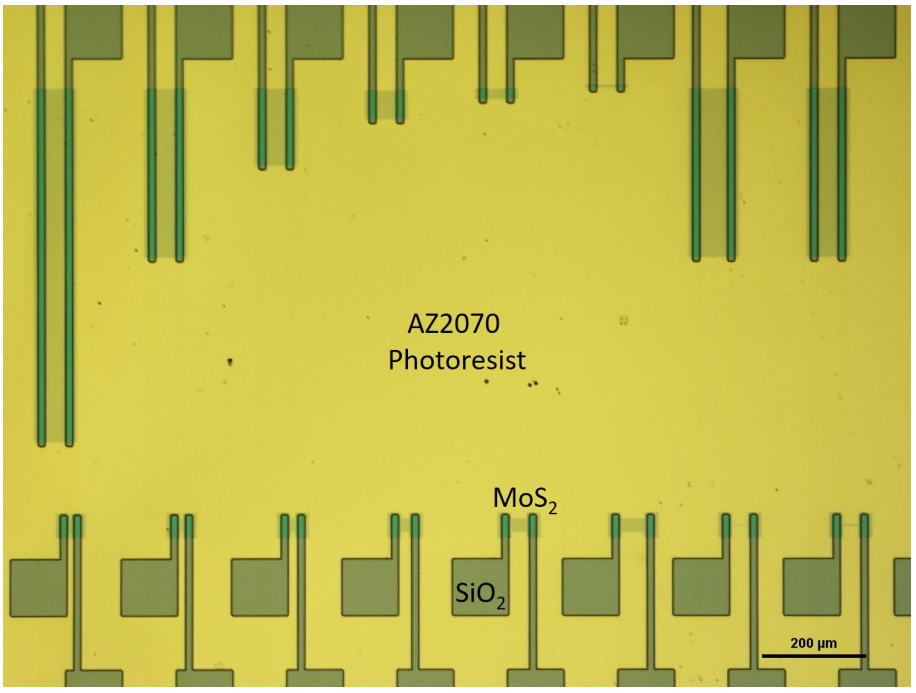

FIGURE 5.6: Optical microscopy of metal patterns on patterned MoS_2

Finally polyethylene oxide / lithium perchlorate (PEO / $LiClO_4$) ionic liquid was prepared by dissolving polyethylene oxide (PEO) and LiClO4 in methanol with a mass ratio of 1 : 0.12 :40 [121] and transferred on the surface of the chips by a pipette. The transistors were measured using a Keysight B1500a in a cascade probe station.

5.1.4 MoO_3 prepatterned process

As MoO3 is a material that dissolves very rapidly in alkaline solutions, a simpler process was also designed that removes a lot of complexity and improves the

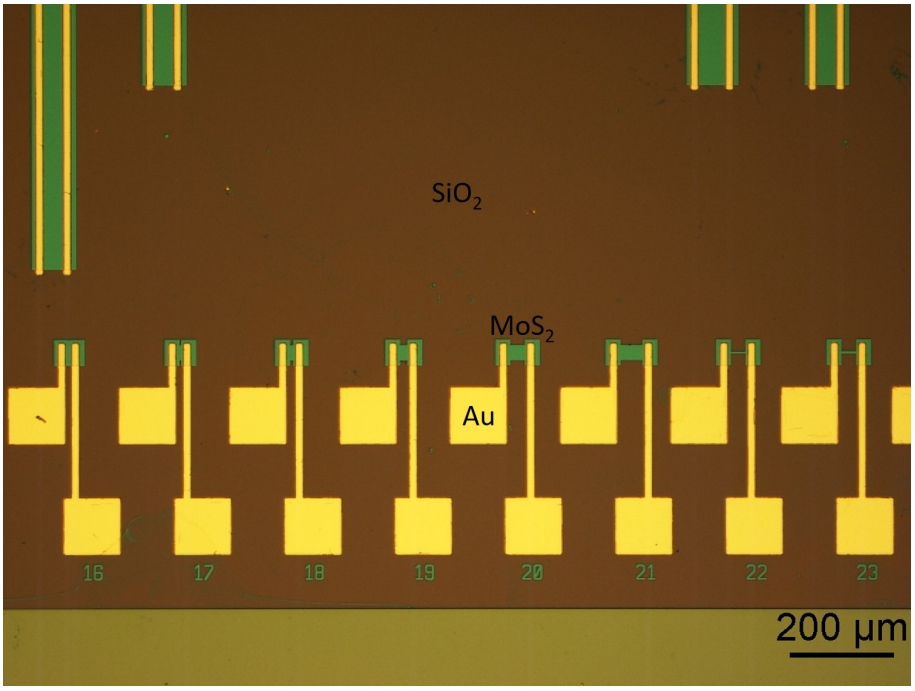

FIGURE 5.7: Final FET devices

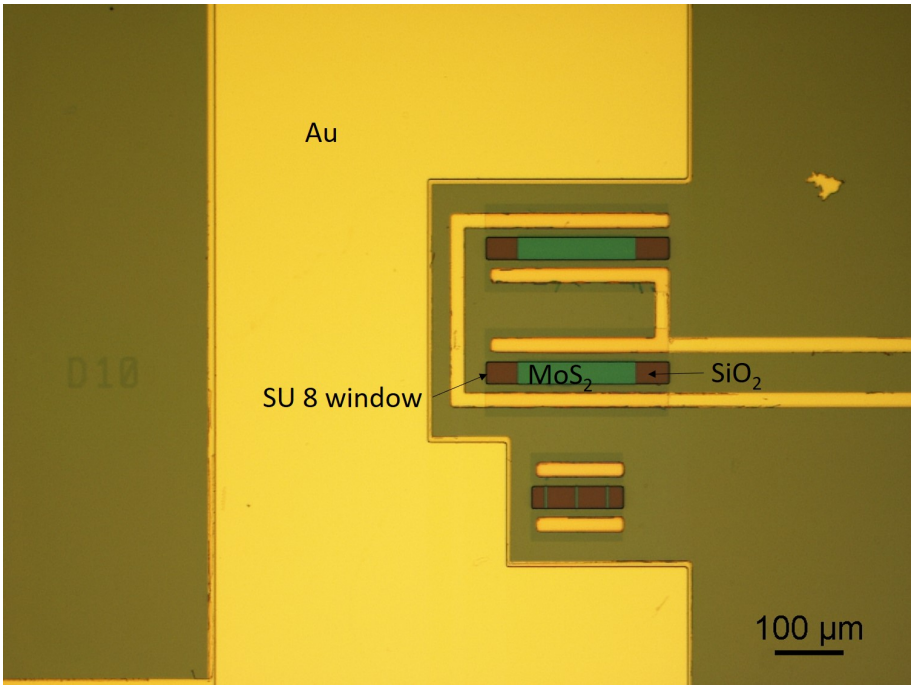

FIGURE 5.8: OPtical microscopy of an FET device protected by a patterned SU8 window

quality of the transistors. In this process MoO_3 was patterned for the channel layer directly following the same lithography process described above for the MoS_2. The last step of the process involves development of the photoresist and washing with DI water. During this step MoO3 is dissolved and therefore the channels are patterned. The photoresist can then be removed by rinsing with Acetone-IPA as it has not hard crosslinked. The wafer is then diced into smaller pieces and undergoes the sulphurisation process described in the section above. As the channels are already formed the MoS_2 is protected with alumina and then patterned for the metal contacts deposition following steps f, g, h of figure 1. This method provided the advantage that a full 6-inch wafer was patterned at once and reduced the complexity of etching MoS2 and removing highly crosslinked photoresist while alleviating the effects of possible unwanted doping during the RIE process [122]. As it will be shown in the results section the results of the prepatterned protocol exhibited marginally better peromance. It was expected that the prepatterned device would have a higher performance due to the fact that the patterned film relieved the lateral stress during the annealing process. The fact that this did not happen indicates towards the fact that the starting MoO3 is structured with short discontinuities so there is no stress during MoS2 formation. This might initially seem as a disadvantage but by tuning the annealing process it was achieved that the resulting film always remained continuous and therefore the porosity of the MoO3 was used as an advantage.

5.1.5 Sputtering

Sputtering is a process in which atoms from a cathode − target are driven off the material by bombarding ions. Sputtered atoms travel away until they meet a substrate, where they deposit as a layer. An applied electric field between two electrodes is creating ions in a gas at low pressure. The gas breaks down and it conducts electricity at a specific minimum voltage. Then the ions of the plasma are accelerated at the target by a large electric field and as they impact the target, atoms or molecules are ejected from the surface of the target into the plasma,

where they are carried away and then deposited on the substrate. This type of sputtering is called DC sputtering. The sputtering gas is usually an inert gas in order to avoid chemical reactions between the sputtered atoms and the sputtering gas. However, in the case of the reactive sputtering a technique that is used to deposit films such as oxides and nitrides, a reactive gas is added to the inert gas so that the deposited film can be a chemical compound. As the ions strike the target, their electrical charge is neutralized. When the target is an insulating material, the neutralization results in a positive charge on the target surface. This charge should reach a level where the bombarding ions are repelled away and the process stops. In order to continue the process, the polarity must be reversed to attract electrons from the plasma so the surface charge can be eliminated. For that reason a radio−frequency voltage is applied on the target. This type of sputtering is known as RF sputtering. In order to increase the efficiency of the sputtering process, a magnetron source is used for magnetic confinement. The magnetic field causes the electrons to spiral so in that way they have more chance of undergoing an ionizing collision and thus enabling the plasma to be operated at a higher density. This kind of sputtering is called magnetron sputtering. Sputtering was used using the Orion AJA sputterer to form the metal electrodes for the MoS_2 FET devices. The power of the sputterer was set to the minimum stable value of 75 W (3 inch target) to avoid any unwanted Ar sputtering of the MoS2 and at a pressure of 2 mTorr.

5.2 DC characteristics of 2D FETs

5.2.1 Fabrication and DC characteristics of CVD grown graphene FET

Graphene grown,copper was etched backside etched in RIE using an oxygen atmosphere at 100 W for one minute to remove graphene grown at the backside of the copper foil.After etching the foil was spin coated at 4500rpm / min with 495

PMMA 11 and baked on a hot plate for 2 minutes at 100^0C. Subsequently the foil was etched in ammonium persulfate solution for 2 hours. Finally the graphene PMMA was cleaned multiple times in beakers containing DI water and transfered on Si / SiO_2 (270nm). The sample was left in a chloroform bath for three days and then cleaned with the standard protocol by rinsing acetone and IPA. Then S1813 photolithography was used in order to define graphene channels by spin coating the positive tone photoresist S1813 on the sample at 4500 rpm for 60 seconds. followed by a one minute heating on a hot plate at 110^0C. UV photolithography was performed with an exposure of 130 mJ / cm^2.Finally the structures were developed in the developer MF319 for 40 seconds. In order to etch graphene O_2 gas was used with the power set at 100 Watt for 1 minute. Then a second photolithography step was used employed by using the negative tone photoresist AZ2070 by spin coating the photoresist at 4500 rpm for 60 sec and subsequently soft baking for one minute at 110^0C source and drain areas were defined by exposing at 180 mJ/cm^2 followed by a hard bake at 110^0C for 1 minute. Finally the structure was developed in the 726 MIF developer for 45 seconds. E beam evaporation was used for depositing Ti / Au 20 nm/50 nm with a deposition rate of 0.02 nm / min for the Ti metal and 0.03 nm / min. for the Au metal at a base pressure of $7x10^{-6}$ mTorr. The metals were lifted off by immersion in NMP. Finally photoresist was resist spin coated to protect the fabricated devices during the back etching of the oxide present on the wafer by etching in an CHF_3 / Ar enviroment with gas flows of 16 sccm / 34 sccm with a power of 200 Watt and pressure of 30 mTorr for 8.5 min. The resulting device was measured with the Hall effect providing information of the major carrier concentration and their mobility amongst other electric properties. Apparently the graphene was p doped with a carrier concentration of $+4.7 \times 10^{12}$ / cm^2 and mobility of 45.1 cm^2 / V.s . Summary of the Hall results is presented below.

RESULTS SUMMARY

Rs: 2.943e+04 ohm/sq	RHs:	+133 m³/C	Ns: +4.702e+12 /cm³
R : 0.002943 ohm-cm	Mob:	45.1 cm²/V-s	N : +4.702e+19 /cm³

FIGURE 5.9: Graphene Hall effect results

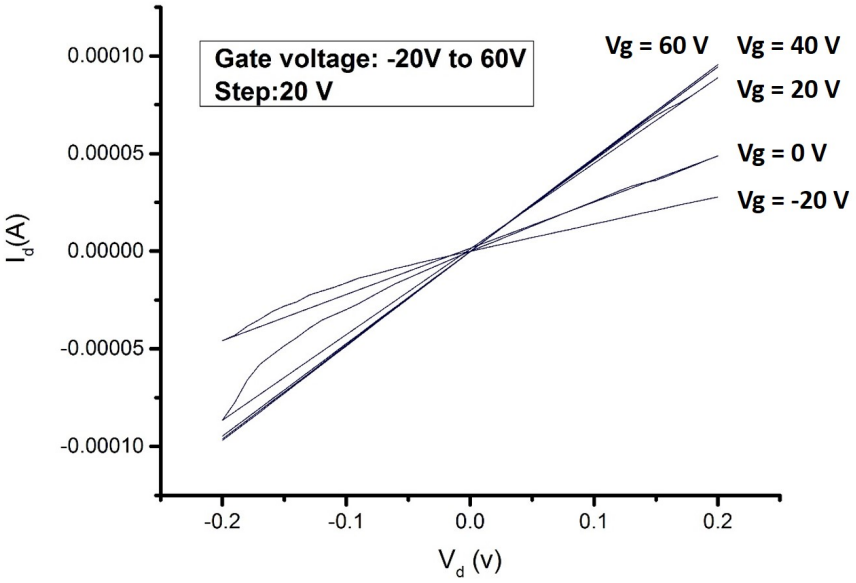

FIGURE 5.10: Graphene FET output curve

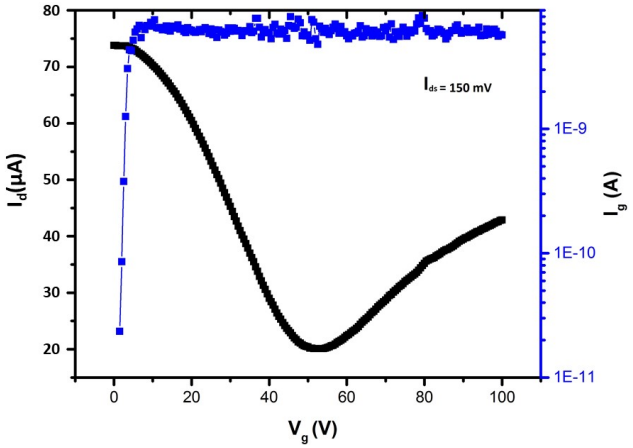

FIGURE 5.11: Graphene FET transfer curve, the right axis illustrates the back-gate leakage current

The output curve shown in Figure 5.10 is demonstrating the Ohmic contacts achieved between Ti / Au and graphene and the efficient gating on the 270 nm SiO_2. The transfer characteristics of the FET presented in figure 5.11 are in agreement with the Hall measurements, since a large shift of the Dirac point to positive voltages is observed, this shift can be accounted to the p doping of the material. The ON / OFF ratio of the device is 3.3 as it was expected and described before.

5.2.2 DC characteristics of 2d TMDCs FETs

After the fabrication described by Al_20_3 capping a number of devices were fabricated as FETs. Figure 5.12 presents an FET fabricated from the first annealing protocol (single step high sulphur pressure) presented in 4 exhibiting poor conductivity

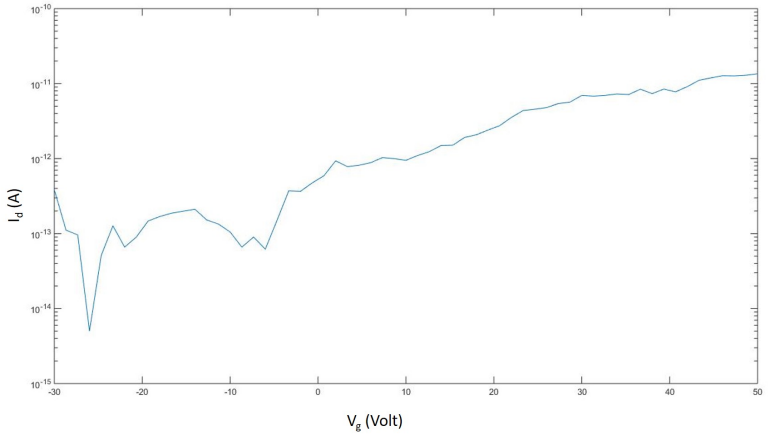

FIGURE 5.12: Transfer characteristics of MoS_2 grown at high H_2S vapour pressure

The following devices presented are FETs fabricated by the two step annealing protocol that exhibited a stoichiometry of S : Mo 1.87. First presented in figure TLM measurement was done in order to evaluate the sheet resistance and the contact resistance before and after the Al_2O_3 deposition. Figure 5.13 presents the TLM graph for FET devices with widths 40 μm. The sheet resistance was found to be 4.69 kΩ / $\square$ and a contact resistance of 59.7 MΩ. Upon the Al_2O_3 deposition

the TLM shown in figure 5.14 the sheet resistance dropped to 3.96 kΩ / □ and the contact resistance was found at 49.6 MΩ.

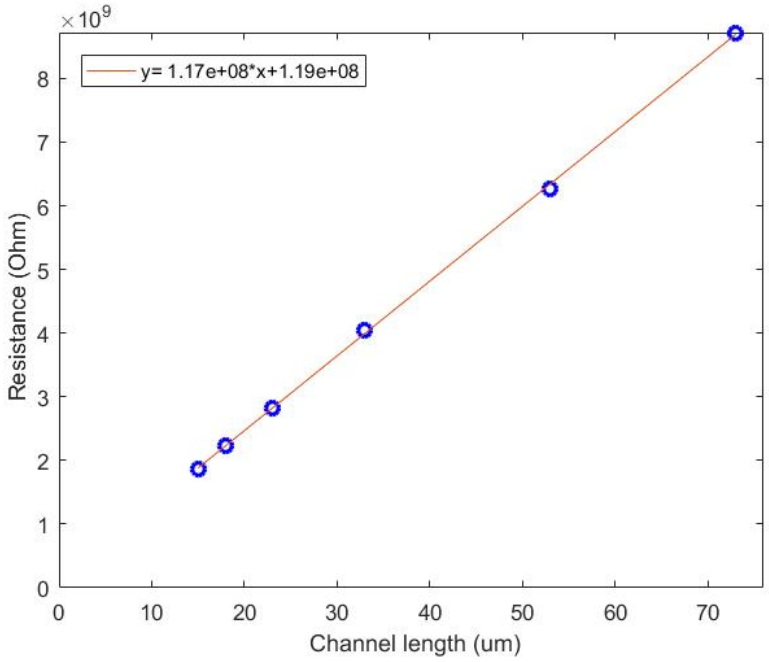

FIGURE 5.13: TLM measurements of MOS_2

Next ionic measurements were performed by pipetting PEO / $LiClO_4$ on top of the SU8 window fabricated above the FET channel. The gate voltage used for modulating the FETs conductivity was set at -1V to 2V. Figure 5.15 presents the log transfer characteristics of the subthreshold slope, 700mV / dec and and 10^3 on/off ratio for Vd = 350 mV / dec. Figure 5.16 presents the linear transfer characteristic where the threshold voltage of the device was found at 1.3 V.

The prepaterned MoS_2 film in figure 5.17 showed substantially better transfer characteristics exhibiting a subthreshold slope of 180 mV / dec and thereshold voltage of 1.3 V for Vd = 75 mV presented in figure 5.18.

The prepatterned device was also tested by gating it with a PBS buffer solution in order to explore the possibility of employing these films for bio sensing applications by acquiring measurements at zero backgate voltage and -40 V. The results shown in figure 5.19 are representing the zero back gate with the blue line where an ON/ OFF ratio of 2 exhibiting a high off - state at 10^{-8}. The dual gated experiment

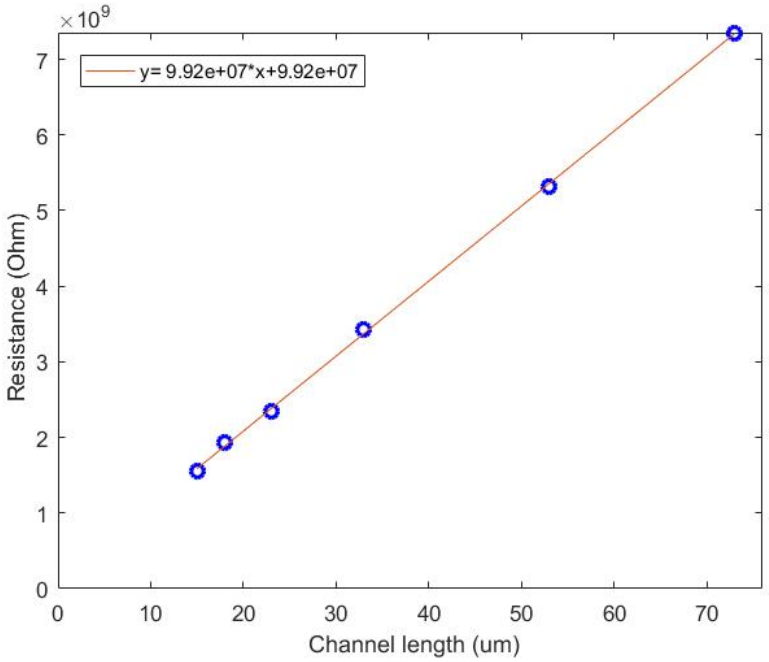

FIGURE 5.14: TLM measurements of Al_2O_3 capped MOS_2

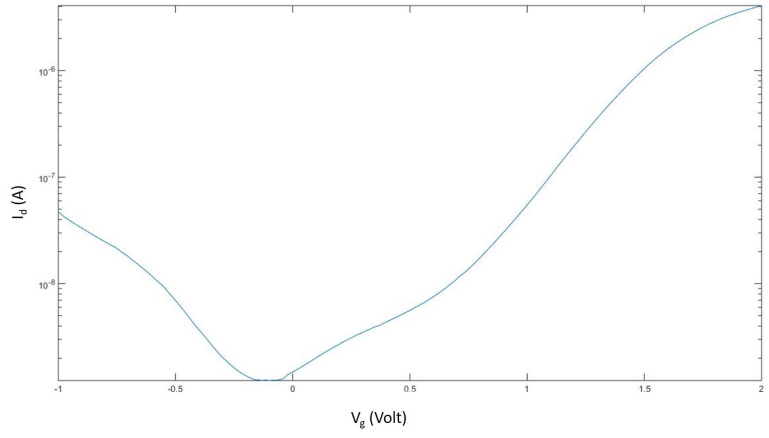

FIGURE 5.15: Log transfer characteristic curve of top gated MOS_2

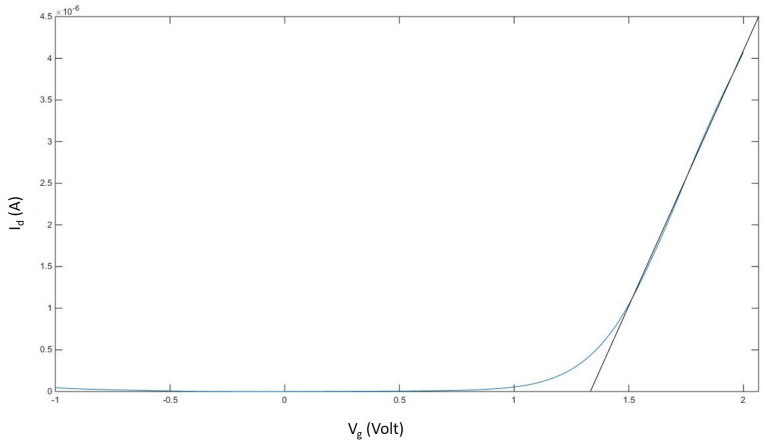

FIGURE 5.16: Linear transfer characteristic curve of top gated MoS_2

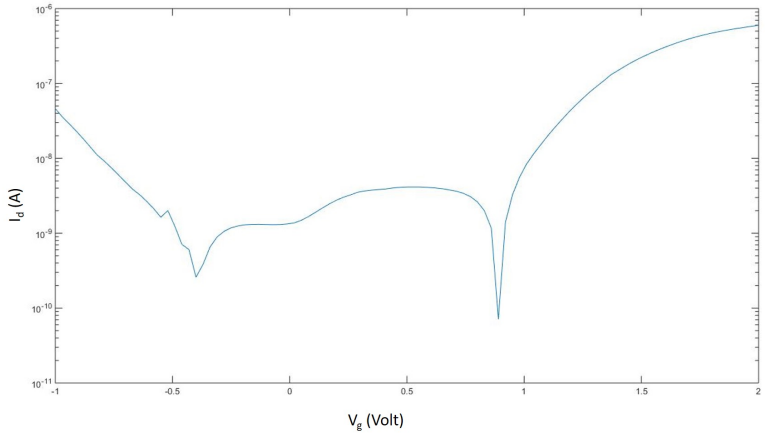

FIGURE 5.17: Log transfer characteristic curve of top gated prepatterned MoS_2

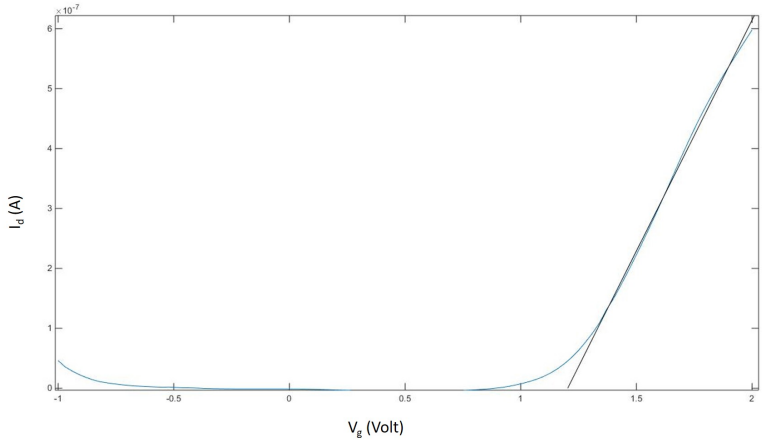

FIGURE 5.18: Linear transfer characteristic curve of top gated prepatterned MoS_2

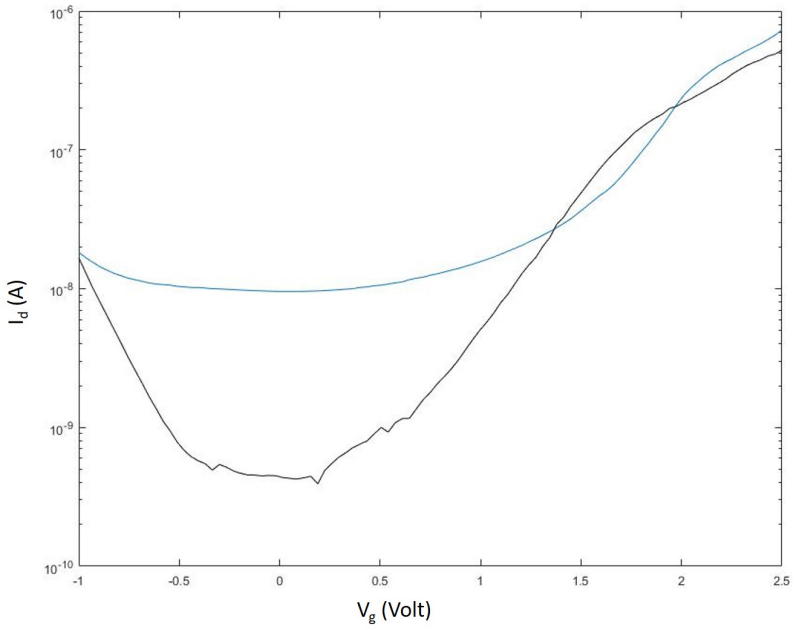

FIGURE 5.19: Log transfer characteristic curve of double gated prepatterned MoS_2 (blue curve for zero back gate, black curve for -40V back gate)

was done at -40 V (shown in black) efectively depleting the MoS_2 channel leading to an off current dropped to 10^{-8} and a substantial subthreshold slope compared to the non back gated experiment, re emerging at 800 mV / dec.

5.3 2D wafer scale heterostructures process

Here a hetrostructuring process is presented that is based in common photolithographic techniques for creating wafer scale 2D heterostructures.

First step of the process is a typical photolithography patterning of the desired structure to be patterned on a blank Si / SiO_2. The grown 2D film is lifted from the growth substrate the method described by [90], briefly 2% polystyrene dissolved in toluene is spin coated on the 2D material and baked. After the cooling of the sample a small droplet of water is placed at the edges and penetrates between the substrate and the film due to different surface energies releasing the film. Then the film is placed on top of the pre - patterned S1813 photoresist and is heated at 95^0C for 5 minutes which is close to its transition glass temperature. The heating allows the PS film to come in conformal contact to the substrate by eliminating wrinkles that are a common isue for transferred 2D materials because of the inherent height of the photoresist pattern, figure 5.21(a) shows the transfer polymer / Mos_2 on patterned photoresist where no ripples are present in the defined areas. After allowing the sample to cool down, chloroform is used in order to dissolve the PS film by not affecting the under lying photoresist. In that way the 2D material is left intact in predefined areas. The same process can be repeated multiple times for creating aligned heterostructures in a wafer scale manner.The first experiments were carried out in order to test the transfer efficiency in terms of minimum size transfer possible and the transfer yield. Figure 5.20 shows the minimum size transferred at 5 um with a transfer yield of 292 / 300 transferred areas. Figure 5.21 (b) shows a number of MoS_2 WS_2 heterostructureswhile figures 5.21 (c)(d)presents the Raman and photoluminescence characteristics of the heterostructures. Finally figure 5.22is presenting all the steps of the heterostructuring process.

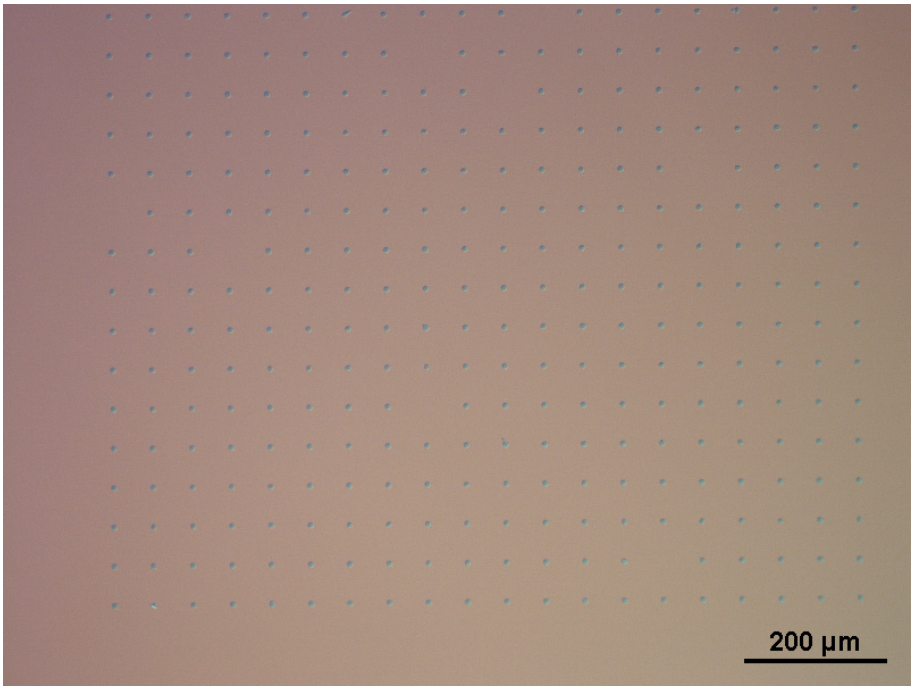

FIGURE 5.20: Large scale transfer of micrometer sized patterns heterostructure

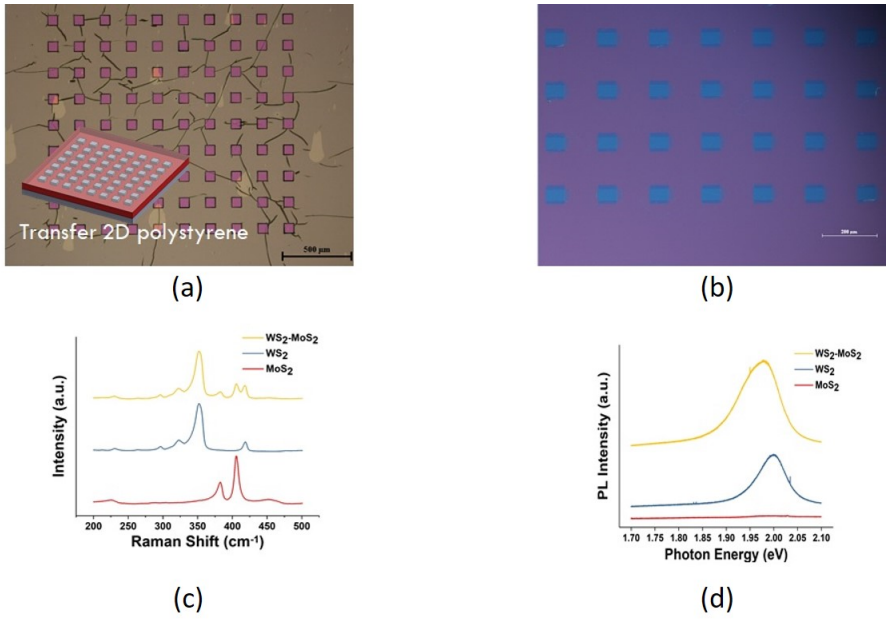

FIGURE 5.21: a) Optical microscopy of polymer - 2D transferred on patterned S1813 b)Optical microscopy of multiple $WS_2 - MoS_2$ heterostructureRaman characterization of $WS_2 - MoS_2$ heterostructures c) Raman characterization of the individual materials and at the overlapping area of the heterostructure d)Photoluminescence measurement of each individual material and their overlapping area

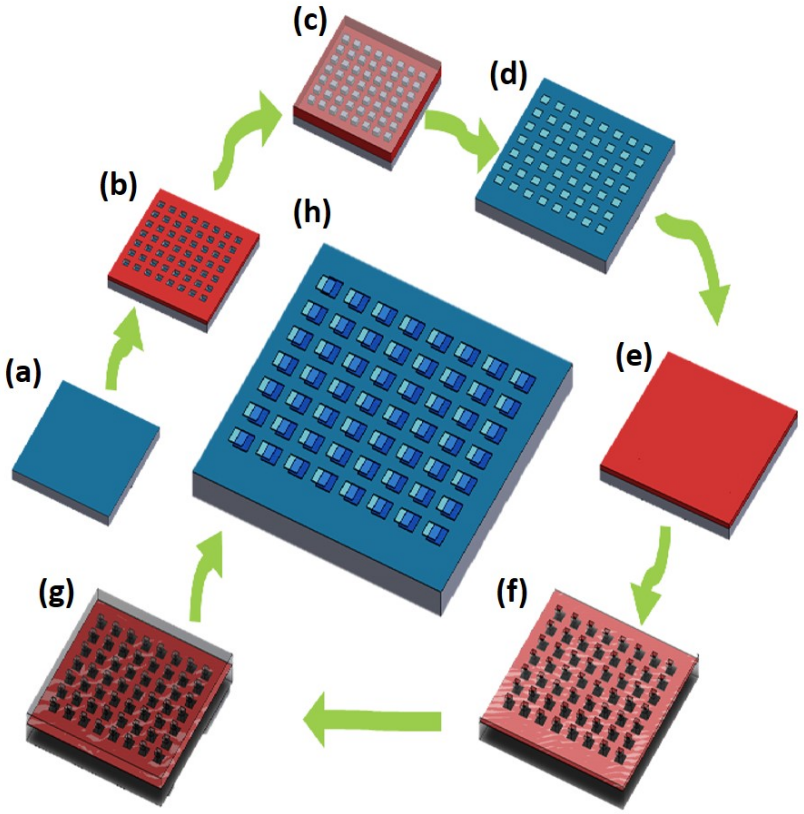

FIGURE 5.22: The wafer scale 2D heterostructure process a)fresh substrate, b)S1813 photolithography patern c) polymer 2D material transfer d)dissolve and lift - off of the photoresist e)spin coat photoresist f)photolithofraphy pattern g)second transfer of 2D - polymer h)final heterostructure after lift - off and polymer removal

5.4 Conclusion

This chapter has demonstrated different approaches of wafer microfabrication techniques for 2D materials. While graphene proved to be capable to be fabricated and further characterized in an FET configuration using standard photolithographic techniques, oxide encapsulation of MoS_2 prior to the photolithography process was proven to be the most viable solution of fabrication due to the protection of the material from the developers used. Furthermore a novel prepatterning protocol of the ALD grown MoO_3 was developed eliminating the need for etching the material in order to create FET channels that has presented substantially better

transfer characteristics compared to non prepatterned film. Finally a high quality deterministic transfer of 2D materials was presented for the fabrication of 2D heterostructures towards wafer scale implementation of different 2D materials.

Chapter 6

CVD grown MoS_2 meta - material

6.1 Introduction

The change of optical properties that some usually natural compounds or polymeric materials show upon the application of external stress is named mechanochromism. An artificial nanomechanical metasurface formed by a subwavelength nanowire array made of Molybdenum Disulphide, Molybdenum oxide and Silicon nitride, is presented in this chapter, that changes colour upon mechanical deformation. The aforementioned deformation induces reversible changes in the optical transmission (relative Transmission change of 197% at 654nm), thus demonstrating a giant mechanochromic effect. Moreover, it is shown that this type of metasurface, can exist in two non-volatile states presenting a difference in optical transmission of 45% at 678nm , when they are forced to bend rapidly. The wide optical tunability that photonic nano-mechanical metasurfaces, such as the one presented here, possess by design, can provide a valuable platform for mechanochromic and bistable responses across the visible and near infrared regime and form a new family of smart materials with applications in reconfigurable, multifunctional photonic filters, optical memory, switches, stress sensors and / or actuators. Up to date, control of electromagnetic properties of photonic metamaterials and / or metasurfaces, artificial media structured on the subwavelength scale, have been achieved

via nanomechanical reconfiguration of its building blocks, [123] [124] [125] structural phase change in the material of constituting elements, [126] [127] [128] [129] carrier injection effects, [130] [131] [132] [133] application of liquid crystals, [134] [135] chemical modification [136] and by stretching the elastic substrate supporting plasmonic or dielectric metamolecules. [137] [138] Mechanochromism is the colour change, upon mechanically induced reorganization of crystal structure or mechanically induced structural phase transition. [139] Such effects have been studied in a number of materials, [139] [140] where strongest effects are seen in polymers, [141] liquid crystal elastomers, [142] [143] nano-fibres [144] and photonic crystals. [145] Recently, chromic effects have been used as tuning mechanisms for photonic metasurfaces and plasmonics related devices with thermochromic and electrochromic responses, respectively. [146] [147] In recent years, strain engineering of optical and mechanical properties of solids, in particular silicon and two-dimensional solids have attracted considerable attention. [148] [149] Two dimensional materials, such as graphene, oxides, nitrides and transition metal dichalcogenides are of particular interest as constitutive elements for reconfigurable metamaterials and metasurfaces, as the extreme electron confinement inherits them with unique dielectric properties that can be controlled by external stimuli. [150] In particular, molybdenum disulfide, MoS_2 is formed from the covalent bond between transition metal atoms (Mo) sandwiched by two layers of chalcogen atoms (Sulphur), while every sheet is bound via weak van der Waals interaction. Several theoretical reports have indicated that the energy bandgap renormalization can occur on MoS_2 upon stress, where microscopic parameters like carrier mobility and effective mass of carriers upon mechanical deformation can lead to substantial changes on refractive index. Furthermore, excitonic peak emission wavelengths have been observed to be sensitive to mechanical stress in its monolayer form. [151] [152] [153] [154] [155] [156] MoS_2 has excellent mechanical properties because its large Young modulus (330 GPa) and high elastic limit which makes it an attractive material for nanomechanical devices. [157] A previously unexplored mechanism of tuning optical properties of photonic metasurfaces exploits the phenomenon

of mechanochromism. The elastic strain in a MoS_2 / MoO_{3-x} / Si_3N_4 nanomechanical photonic metasurface causes a profound change in its optical properties, which originates from the strain-sensitive refractive index of MoS_2, enhanced by electromagnetic resonances created by nanostructuring. Specifically, heat activated nano-mechanical deformation of the array of nanowires leads to profound reversible changes of its transmission, reflection and absorption in the visible part of the spectrum operating either as photonic filter or as a photonic memory element. Transmission changes of up to 197% are obtained at 654 nm upon 2% of mechanical strain, while two non-volatile states presenting a difference in optical transmission of 45% achieved at 675 nm. The response of the system is controlled via the speed of induced mechanical stress. These types of devices can serve not only as photonic elements but also as strain sensors / actuators with an optical readout. The metasurface was fabricated on a 90 nm thick Si_3N_4 membrane which was patterned as an array of nanowires 22 μm long, 400 nm wide with gaps of 100 nm separating them (see Figure 6.1).

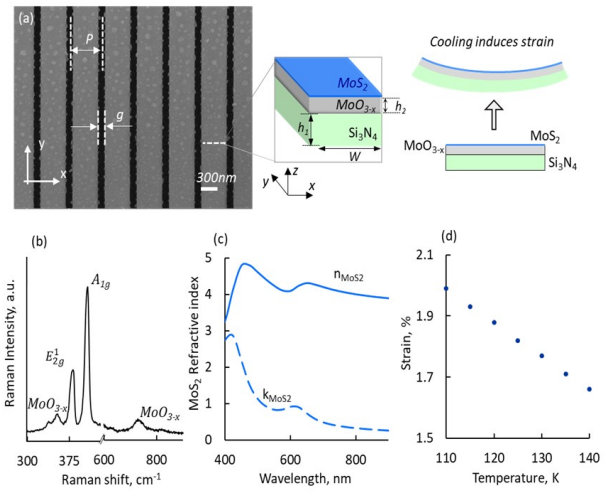

FIGURE 6.1: MoS_2 based metasurface. (a) Scanning electron microscope image of the metamaterial formed by a nanowire array manufactured on a MoS_2 / MoO_{3-x} / Si_3N_4 trilayer membrane, schematic of a single nanowire [P = 500, g=100, h1 = 90, h2 = 50, h3 = 5, W = 400 nm], scale bar 300 nm. (b) Raman spectra of metamaterial shows the composition of the sample (c) Ellipsometric data of a few layer MoS_2 film (d) Strain induced in a single nanowire upon cooling, deformation of the nanowire is caused by the large thermal expansion mismatch between Si_3N_4 and MoO_{3-x}.

.

6.2 Experimental section, Metamaterial fabrication

Metamaterial fabrication: Nano-grating metamaterial patterns, with a fixed gap width g=100 nm and period P=500 nm, covering an area of approximately 22 m x 25 m, were directly etched via focused ion beam (FIB) milling, using a FEI Helios NanoLab 600 dual beam system, on a commercially available 90 nm thick Si_3N_4 membrane from Norcada Inc. Then, an APCVD synthesis method was used for the deposition of the MoS_2 on the pre-patterned membrane, with two separate precursors: MoO_3 (10 mg) and sulphur (70 mg). A silicon nitride membrane is placed at the centre of the furnace and a quartz boat containing the MoO_3 precursor was placed upstream at a distance of 3 cm. The sulphur powder is placed in a separate quartz boat outside the furnace at a distance of 30 cm with controlled ambient temperature. Prior to the deposition, the quartz tube was flushed with 500 sccm of Ar gas for 1 h. The temperature of the furnace was first ramped up to 500^0C with a rate of 20 ^{0}C / min and subsequently up to 700^0C with 4^0C / min under constant flow of Ar at 200 sccm allowing the evaporation and deposition of MoO_3. At the temperature of 700^0C the sulphur zone was heated up to 170^0C for 15 minutes. During the process, a sulphur rich time window, the as-deposited MoO_3 was partially converted to MoO_{3-x} and MoS_2 progressing in a layer by layer manner while MoS_2 in the gas phase is codeposited. After the 15 minutes time window, the gradually sulphur deficient environment results in the deposition of a metal oxide rich layer. Variable-Angle Spectroscopic Ellipsometry: The complex relative permittivity / refractive index APCVD deposited MoS_2 was evaluated by spectroscopic ellipsometry (J. A. Woollam 4000) over the wavelength range from 400 to 900 nm. Numerical simulations: Full-wave electromagnetic simulations of the metamaterial structure, based on the geometry presented in Figure 6.1 a, were performed using the finite element method in COMSOL Multiphysics. Calculations employ periodic boundary conditions in the x and y directions (i.e. effectively assuming an infinite array of infinitely long nanowires). They utilize refractive indices for silicon nitride and MoO_3 assumed to be non-dispersive and

equal to 2, while for MoS_2 ellipsometry data used are presented in Figure 6.1 c. Furthermore, numerical spectra are evaluated for an off-normal incident angle of 9^0C, as opposed to normal incidence, to more realistically represent the focused probe beam produced by the microspectrophotometers objective lens linearly polarized plane wave illumination; Nanowire mechanical deformation was obtained from finite element models of a single, isolated 22 μm long wire with fixed ends and rectangular cross sections as presented in Figure 6.1 . These assumed Youngs moduli E and density values for Si_3N_4, MoO_{3-x} and MoS_2: ESiN = 200 GPa; EMoO = 80 GPa; EMoS=320 GPa; rSiN = 3170 kg m^3, rMoO = 4690 kg m^3, rMoS=5060 kg m^3. Raman spectroscopy: Raman measurements under 532nm laser excitation indicate the deposition on the prepatterned membrane of both MoO_{3-x} and MoS_2. The few layer MoS_2 was confirmed by the Raman E_{2g1} mode at 381 cm^{-1} and A_{1g} mode at 407.5 cm^{-1} and the MoO_{3-x} the Raman peaks at 353 cm^{-1} and 733 cm^{-1}. Microspectrophotometry (including low temperature measurements): transmission and reflection spectra (Figure 6.2) were obtained using a microspectrophotometer (CRAIC QDI2010), with a 11m 11m sampling aperture via a 15 objective with NA 0.28. All data are normalized to reference levels for air (100% transmission), a silver mirror (high reflector) and a Vantablack vertically − aligned carbon nanotube array (zero reflection / transmission), and averaged over 15 repeated measurement cycles, each with a 500ms integration time. For the low temperature measurements, a cryogenic Linkam stage (model No THMS600) with temperature control. Pressure level is monitored throughout the experiment at 10^{-3} mbar. Measurements performed while temperature level was stabilized with fluctuation of less than 0.1K

6.3 Metamaterial characterization

The pre − patterned Si_3N_4 membrane, was coated with a 60nm thick layer of MoO_{3-x} and a 5 nm layer of MoS_2 by atmospheric pressure chemical vapor deposition (APCVD). The composition of the sample has been evaluated using reflective Raman spectroscopy. Figure 6.1 b shows the Raman spectrum of the nanowire

indicating its crystallinity: the 381 cm^{-1} line relates to the in− plane vibration E_{2g} mode, while the 407.5 cm^{-1} line corresponds to the out − of − plane vibration A_{1g} mode of MoS_2. [32] The 353 cm^{-1} and 733 cm^{-1} lines indicate the presence of MoO_{3-x} in the structure. [158] Furthermore,the complex refractive index of MoS_2 layer of the composite nanomembrane was measured by spectral ellipsometry, Figure 6.1 c. These results were used to computationally model the optical properties of the nanowire array, as presented in Figure 6.2 b. Measured and computed optical properties of the metamaterial are presented in Figure 6.2. At optical wavelengths longer than the structure period of 500 nm the nanowire array does not scatter light and acts as an optically homogeneous metamaterial layer, that can be fully characterized in terms of its transmission, reflection and absorption. However, the periodic structuring, results in reflection and transmission resonances at 654 nm and 810 nm for linearly polarized light parallel to the wires, with a quality factor of Q=25. The experimental spectra are well reproduced in computational modelling, as shown in Figure 6.2 b. The field maps in Figure 6.2 c,d reveal that on resonance, displacement currents running through the nanowires with higher concentration within the high index MoS_2 part, interfere constructively with incident light and block transmission over this wavelength, as studied in the past. [128] [159] [160] Small discrepancies between measured and computed spectra can be attributed to fabrication tolerances and accuracy of the refractive index values used in the modelling.

Optical properties of such metasurfaces are expected to be strongly dependent on temperature, given the stress-induced modifications of band structure of MoS_2 component. Indeed, heat activated nanoscale reconfiguration of the metamaterial induces nanomechanical deformation of the wires. Since the MoS_2 is much thinner than Si_3N_4 and MoO_{3-x} layers, the thermal expansion mismatch between the Si_3N_4 and MoO_{3-x} is the main mechanism of the bow-like deformation of the nanowires upon cooling / heating (the thermal expansion coefficients are 2 x 10^{-6} K^{-1} and 6 x 10^{-5} K^{-1} [161] , respectively). This deformation in its own turn leads to the stress-induced modification of the optical properties of the MoS_2 layer. Stress-induced change of optical properties of the wide band gap materials Si_3N_4 (E_g =

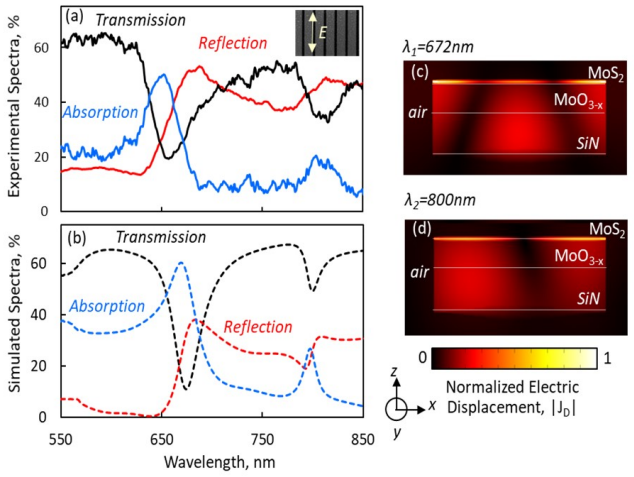

FIGURE 6.2: Optical properties of MoS_2 based metasurface. (a) Reflection, transmission and absorption spectra of mechanochromic metamaterial under linear polarized illumination, as indicated on inset to plate. (b) Numerically simulated reflection, transmission and absorption spectra of the metamaterial. (c,d) Numerically simulated distribution of the electromagnetic field in the metamaterial nanowire. Color maps show the magnitude of the electric displacement in the x−z plane.

.

4.5 eV) [162] and MoO_{3-x} (E_g= 3.1 eV) [163] are insignificant in the part of the spectrum of interest. Our finite element method (FEM) mechanical stress calculations -based on the linear momentum balance equation and the linear stress-strain relation- are displayed in Figure 6.1 d, employing a single nanowire. They show that decrease of the nanowire array temperature from 300K to 110K results in a bow-like deformation of 50nm that induces a compressive stress of 2.05% to the MoS_2 layer. Since thermal cooling of the metasurface induces mechanical strain upon the MoS_2 layer, the transmission spectra were measured at different temperatures using a microspectrophotometer, to test its mechanochromic response. First the induced changes in optical transmission was studied as a function of applied strain. Figure 6.3 presents the optical transmission of the mechanochromic metasurface for various strain levels, at the cooling rate of 5 K / min. The relative transmission was defined as the change ΔT / T_0, where $\Delta T = T_\epsilon - T_0$; T_ϵ being the absolute transmission at an applied strain ϵ and T_0 the transmission for zero strain. For small strain levels below 1% − the transmission change is small, however larger strain upon MoS_2 induces change in Transmission spectra

of the sample. At 2% strain the induced change reaches maximum values of 197% and 80% at 657 and 810 nm, accompanied with the samples colour change, inset Figure 6.3 a. In this work, the limits of elastic deformation wre not studied as the applied strain did not exceeded the 2% applied strain level in pursuit of higher transmission change to avoid irreversible nanomechanical deformations. This performance is already exceptionally high as the metasurfaces transmission minimum shifts from λ_0=657 nm to λ_1=681 nm providing giant mechanochromic sensitivity, which is defined by the ratio of the wavelength shift over the applied strain $\Delta\lambda$ / ϵ [nm/%] and is found to be as high as 12, one order of magnitude larger than other polymeric mechanochromic systems.[24] At this and slower cooling rates the change in transmission do not show any hysteretic response.

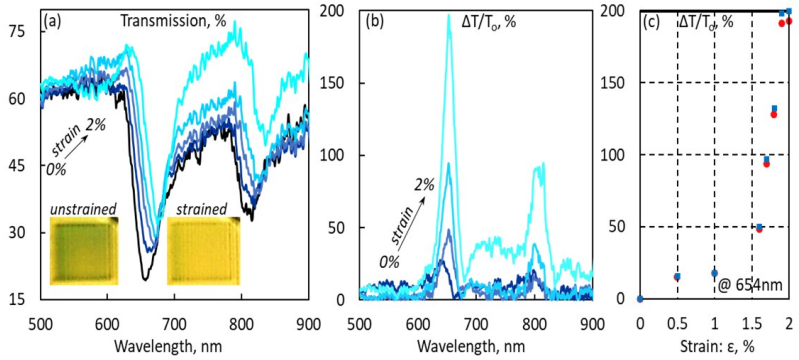

FIGURE 6.3: Mechanochromic response of MoS_2 based metasurface. Variation of the optical properties of MoS_2 metamaterial under stress caused by slow cooling [5^0K/min]. (a) Spectral dispersion of transmission of the metamaterial for different levels of strain up to maximum strain of 2%. Insets shows the perceived colours of metamaterial sample and zero strain and 2% strain. (b) Relative transmission change for different strain levels. (c) Reversibility of induced mechanochromic effect- at 654nm for the full strain cycle, strain up−red circular markers, strain down-cyan rectangular markers.

.

Upon faster cooling rate, 15K / min, a hysteretic behavior of metamaterials transmission is observed, as presented in Figure 6.4 . Figure 6.4 a presents a selection of spectra for different strain levels. For increasing strain, the metasurface demonstrates a red-shift of its spectrum similar to Figure 6.3 . However, on the level

of 1.9% strain a second dip of transmission mode is recorded, as transmission jumps from 31% to 41% for the wavelength of 680 nm, see Figure 6.4 b. In Figure 6.4 b shows the full strain cycle over transmission at the wavelength of 680 nm. Upon decreasing strain (blue line) the optical spectra are different from those of the same strain level for increasing strain (red line). At the level of 1% strain the hysteretic loop closes. Furthermore,the differential hysteresis is defined as: Δh= Abs[Trup(λ)-Trdown(λ)] / Trup (λ) as the relative transmission difference between the two non-volatile states for increasing-decreasing strain, with the largest value recorded at the wavelength of 678 nm equal to 47%. This response is mainly driven by the mechanical buckling of the metasurface; an effect accompanying flexible parts when subject to large applied mechanical load and can therefore be employed in devices requiring optical bistability such as optical memories. The experimentally observed red-shift of the optical response of the metamaterial spectrum depending on temperature can be satisfactorily explained in terms of mechanocromism. The red-shift of the spectrum is related to the strain-sensitive refractive index of MoS_2 rather than the structural reconfiguration of the sample. The metamaterial was designed to keep its optical response invariant upon deflection of the nanowires. Upon cooling, nanowires bend in the same fashion, as a result the metamaterials response is expected to provide negligible transmission changes for small deformations between neighboring nanowires, since most parameters remain the same such as the distance between the nanowires and the period of the metasurface. This is in contrast to previous works that present substantial changes in the optical properties due to the doubling of metamaterials period or by controlling the gap between the nanowires. [123] [164] [165] Our mechanical FEM calculations (COMSOL) indicate that the mid-point of each nanowire is displaced out-of-plane by 50 nm when strain is at 2% and temperature at 110^0K. For this deflection, the optical FEM modelling indicates that solely the 50 nm mechanical deformation of the central part of the array of the nanowires can induce relative transmission changes smaller than 5%. Furthermore, the fact that the transmission change is nonlinear with the applied strain, Figure 6.3 c as well as the observed hysteresis related to the applied stress rate over an increasing-decreasing thermal

cycle, Figure 6.4 , further verifies the mechanical nature of the effect over any thermal effects, that might exist, negligible in the current study.

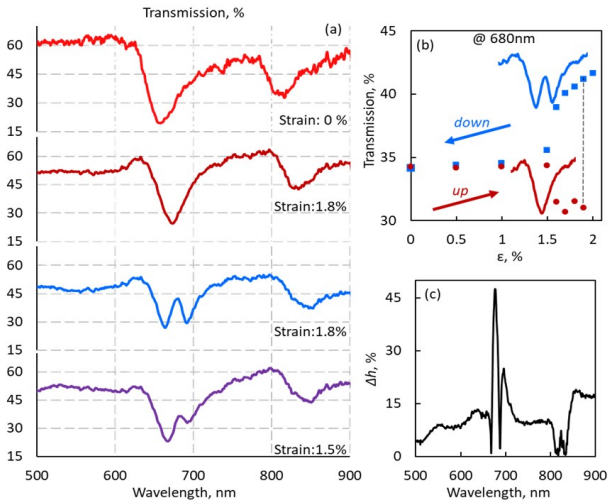

FIGURE 6.4: Hysterisis of MoS_2 based metasurface. (a) Transmission spectra for different strain levels in the regime of rapid cooling [15^0K/min] (b) Variation of the metamaterial transmission at 680 nm during the full strain cycle. A hysteresis of optical properties is observed at strain levels exceeding 1.5%. (c) Span of the hysteresis loop, Differential Hysteresis:$\Delta h = —Trup(\lambda) - Trdown(\lambda)— / Trup(\lambda)$ as a function of wavelength at strain level of 1.8%.

.

6.4 Conclusion

In summary, a new mechanism to tune properties of photonic metamaterials has been presented by studying the mechanochromic response of MoS_2 metasurfaces and identified the conditions under which they can operate either as photonic filters or switches. The proposed device provides continuous and reversible optical tuning of visible transmission with relative transmission change of more than 190% actuated by strain of 2%, which is translated into great mechanochromic sensitivity.

Chapter 7

Conclusions and future work

7.1 Conclusions

This work focused on the large scale film synthesis, the development of wafer scale compatible fabrication processes and the implementation of devices from two dimensional materials. Two material families were investigated for their vast application spectrum, graphene and TMDCs.

Through the literature review, of chapter 3, it was identified that, although there is a plethora of film synthesis protocols those are not always optimised for specific applications. Examples of a variety of synthesis focused research was shown to produce results that are good on paper but gloss over proper device implementation. With this drive, film synthesis protocols were designed as presented in Chapter 4. In the first part of chapter 4 the synthesis of graphene using the in-house built CVD system was discussed. The effects of pressure gas ratios and temperature where investigated and shown that a high quality single layer graphene layer presenting excellent Raman characteristics can be grown on copper substrates. HfS_2 is a very promising candidate for electronic and optoelectronics applications because of its wide bandgap and its predicted high electron mobility. A protocol for its chemical vapour deposition was shown by employing the precursor $HfCl_4$

and H_2S as the sulphurizing agent at low pressure and high temperature. Raman characterization validated the deposition of the thin film but variations of the in plane E_g mode revealed the existence of stresses that was validated by SEM imaging where the grown film presented cracks with domains lifting from the substrate. With a focus on electronic properties a high quality MoS2 synthesis method was designed. Throughout the film growth optimisation it was shown that the annealing H_2S partial pressure of a MoO_3 thin film, the temperature and the total amount of H_2S play the most important role for chalcogenide 2D materials, for semiconducting applications. In fact, those two parameters are the ones responsible for the correct stoichiometry to optimise semiconductor performance. Stoichiometries ranging from 1.85 to 1.98 of MoS where achieved, stoichiometries that fall in the range of stoichiometries for geological MoS_2. The literature review revealed that apart from inconsistencies in the film synthesis method there has not so far been presented a robust fabrication protocol that can be used to process large scale 2D films for electronic and optoelectronic applications. For this reason, Chapter 5 dealt with this matter by implementing a simple yet powerful method for the fabrication of devices from 2D films. It was shown that capping the semiconducting layer plays a very important role in the preservation of the film processes throughout the fabrication process. The method of capping presented here involves the use of 10 nm thin alumina layer deposited by ALD. The alumina layer was etched by HF where it was needed as it was found that TMDCs are inert in short exposures of HF. Furthermore a novel protocol for patterning MoO_3 was devised by patterning structures on the thin film and briefly washing the sample with DI water, washing away effectively the MoO_3. In that way the complexity of the fabrication was reduced by eliminating the need for an etching step and avoiding issues of crosslinked photoresist and unintentional doping by the gases during RIE. Finally, to demonstrate the performance of both the film and the fabrication process FET devices were fabricated and their performance was assessed. A novel protocol for creating 2D heterostructures by deterministic transfer of wafer scale grown 2D materials on photolithography patterned substrates.

The MoS_2 FETs made in this work showed subthreshold slope of less than 130

mV / dec and an on/off ratio of more than 10^4. This is a significant result as it is the first time shown that it is possible to grow and fabricate high performing polycrystalline TMDC transistors on a wafer scale without requiring transfer to a new substrate. A comparison of the FET characteristics revealed the supremacy of the pre - patterned films compared to the unstructured films for both ionic liquid measuremnts and dual gated PBS buffer measurements.

A CVD grown MoS_2 - MoO_3 thin film on an array of Si_3N_4 nanowires was used as a mechanocromic metamaterial in Chapter 6. The function of the metamaterial was based on the thermal expansion mismatch between the Si_3N_4 and MoO_3 the deformation of the nanowires and the stress-induced modification of the optical properties of the MoS_2 layer upon cooling and heating cycles. The metamaterial presented at 2% strain transmission changes that reach maximum values of 197% and 80% at 657 and 810 nm, accompanied by the colour change of the sample.

7.2 Future work

■ Looking into the future there is a number of TMDCs that could be grown by the ALD thermal sulphurization process such as HfS_2 by using HfN as the starting material. The engineering of its stoichiometry would be of high importance since no experimental attempts have been reported up to date.

■ The deterministic transfer method for wafer scale heterostructures presents the opportunity for wafer scale 2D stacking of materials that can not be grown in situ without altering their intrinsic properties therefore a number of materials with different stoichiometries from the family of 2D materials should be explored. Furthermore the nature of the technique renders it a valuable solution to be explored for the fabrication of chalenging devices such as quantum wells.

■ The sequential growth of different oxides and their sulphurization or selenization is also an area that should be investigated for real wafer scale 2D vertical

heterostructures with commercially driven applications such as photodetectors p - n diodes and photovoltaics.

■ The measurements presented of prepaterned MoS_2 FETs gated by ionic liquid and PBS buffer solution showed the cleanliness and robustness of the grown film under harsh liquid environments. Alongside with the hydrophobic nature of MoS_2 that provide a high protein adsorption opens a way for exploring wafer scale two dimensional biosensors.

■ Other types of transition metal dichalcogenides, should be studied as strain dependent refractive index materials for metamaterials, targeting different operational wavelengths.Furthermore materials with larger thermal expansion coefficient difference or longer nanowires can improve mechanochromic sensitivity.

Appendix A

1

A.1 Waveguide integrated graphene midinfrared Photodetector

A.1.1 Introduction

Group IV material photonic integrated circuit platforms have the ability to benefit from graphenes superb electronic and optical properties, in order to address applications in areas such as environmental and bio-chemical sensing, homeland security, medicine or astronomy. Silicon-on-insulator waveguides, which are commonly used in the near-infrared, also have low propagation loss in the 3-4 μm wavelength range. Here, we present the first graphene photodetector based on the coplanar integration method with silicon-on-insulator waveguide and transferred CVD graphene that operates at 3.8 μm wavelength.

A.1.2 Mid-infrared graphene photodetectors

Mid-infrared (MIR) silicon photonics can benefit from the maturity of CMOS processing and from demonstrated devices in the telecom wavelength range as many

of the techniques can be used at longer wavelengths [166]. The silicon-on insulator (SOI) platform has been widely implemented in MIR silicon photonics. SOI waveguides are low loss up to 4 m and waveguide propagation loss as low as 1.3 0.6 dB/cm has been demonstrated at a wavelength of 3.8 μm [167]. 2D materials have several advantages compared to conventional 3D materials, and in particular better quantum confinement in the direction perpendicular to the 2D plane, that leads to distinctive optical and electronic properties. 2D materials can be integrated with other materials using waveguides and cavities to form heterostructures [168]. Due to graphenes gapless band structure it acts as semimetal and can interact with light from microwave to ultraviolet wavelengths. The absorbed photons can be converted to electron hole pairs and move to electrodes quickly due to graphenes fast carrier mobility, which makes it a promising material for light detection or manipulation [169]. Graphene has excellent properties [170] such as high carrier mobility, thermal conductivity, and linear dispersion [171] as well as high optical absorption across a wide range of wavelengths. The optical absorption mechanisms in graphene are divided into two processes: interband transitions and intraband transitions. Interband transitions occur when one electron in the valance band of graphene absorbs a photon and is excited to an empty state in the conduction band with the same momentum [172]. The interband transition is only permitted under the condition that the energy of filled state is larger than the absolute value of the chemical potential. Otherwise, interband transitions will be prevented by Pauli blocking. On the other hand, intraband transition occurs under a phonon assisted process, which happens in the far-infrared (FIR) to terahertz wavelength regions. Interband transitions can be suppressed if the chemical potential is tuned close to the Dirac energy. With the control of the absorption mechanism, waveguide-coupled graphene optoelectronic devices have potential to operate in the MIR wavelength region, and under such circumstances the absorption mechanism is dominated by the interband transition [173] [174] [175]. Thus, the combination of low loss silicon waveguides and high absorption nature of graphene is promising for light detection in the MIR. Single layer graphene was

first demonstrated by Novoselov, Geim and their colleagues by graphite exfoliation in 2004 [176]. By using the coplanar integration method, the optical mode propagates in the silicon waveguides and interacts with graphene at the same time, thus achieving a greater interaction length compared to the normal incidence situation in which the interaction length is limited by the thickness of graphene. In terms of photodetection, by using the coplanar integration configuration, the light-graphene interaction is determined by the length of the device, rather than the thickness of the graphene as in the normal incidence situation. Thus, coplanar integration is a promising solution for high efficiency graphene integrated photodetectors [171] [177] [178] [**?**]. The first demonstration of a graphene photodetector was based on a graphene transistor, in which the metal-graphene junction was illuminated by infrared and visible light, achieving 40 GHz bandwidth at room temperature [179]. However, responsivities were limited to a few mA/W at telecom wavelengths. After optimizing the device configuration, the photoresponse of graphene photodetectors has been increased to a few A/W by several approaches, such as integration of graphene transistor and optical cavities [180], light interaction enhanced by introducing plasmonic antennas [181] [182], or by using in-plane evanescent field enhanced light/graphene interaction [177] [178] [**?**], [183] [184].

A.1.3 Design of the waveguide integrated graphene photodetector

Here we present a waveguide integrated metal-graphene-metal (M-G-M) photodetector with 500 μm long graphene section and with asymmetric electrode separation from the waveguide, operating at a wavelength of 3.8 μm at room temperature. The schematic of the cross-section of the device is shown in Figure A.1 . The first step of fabrication was to use a SOI wafer to form rib waveguides, with a width of 1300 nm, height of 500 nm, and slab region thickness of 50 nm. A 90 nm thick PECVD SiO2 layer was then deposited for passivation and to reduce charging effects. The next step was to transfer the graphene onto the chip surface, and to pattern it by reactive ion etching (RIE). Finally, 100 nm thick Au electrodes were

fabricated by using the lift-off patterning method. Au contacts were positioned on top of the graphene on either side of the waveguide core, with a separation of 1.5 μm on one side and 5μm on the other.

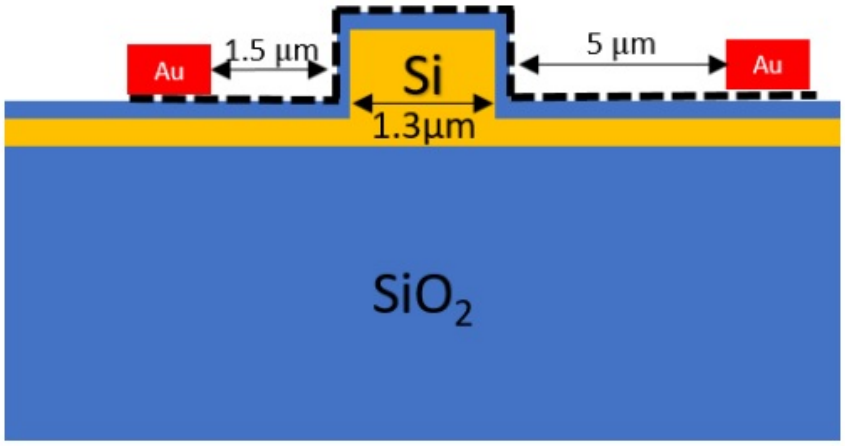

FIGURE A.1: Schematic cross-section diagram of the device.

.

A.1.4 Characterisation

A tunable quantum cascade laser (QCL) operating at 3.7-3.9 μm under continuous wave (CW) mode with transverse electric (TE) polarisation was used as a light source. The light was coupled into the Si waveguides via grating couplers using fluoride based MIR fibres. By using the cut-back method, the normalised transmission of the waveguides covered with graphene was measured, and is plotted in Figure A.2 . The gradient of the linear fitting indicates that absorption due to graphene on the waveguide surface was 150 dB/cm at the 3.8 μm wavelength. In terms of the optoelectronic characterisation, the device was characterised under 1 V bias voltage. Bias voltage was applied to the two electrodes. Generated photocurrent was measured by a picoammeter (Keithley 6487). Figure A.3 plots the photocurrent as a function of the increased optical power that was coupled into the graphene photodetector. The gradient of the linear fitting gives the photoresponsivity of the device at 3.8 μm under -1 V bias voltage of 2.2 mA/W. The optical power incident on the photodetector was calculated by taking into account

the absorption from the input fibre, the coupling loss of the input grating coupler, and the loss from access waveguides.

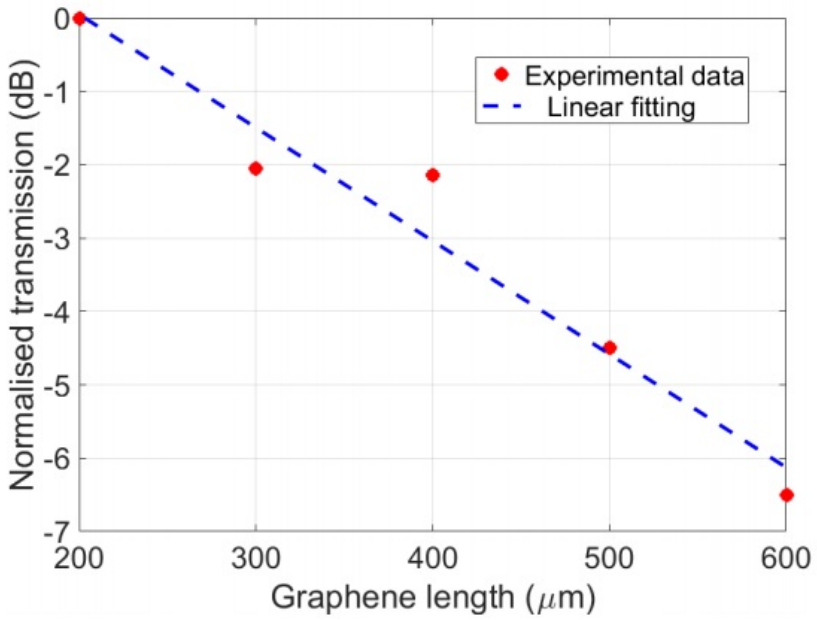

FIGURE A.2: The normalized transmission of waveguides of constant length covered by varying lengths of graphene. The gradient of the linear fitting is the graphene absorption coefficient, which is 150 dB/cm at 3.8 μm wavelength.

.

Figure A.4 shows the calculated photoresponsivities as a function of the bias voltage. From the graph, it can be seen that the negative voltage side shows the linear relation between the bias voltage and the photoresponsivity. Figure A.5 shows the spectrum of the transferred graphene on waveguides with 90 nm SiO2 after all the fabrication processes. G and 2D peaks can be seen in the spectrum but also the defects peaks, which indicates that the single crystal lattice was damaged during the fabrication. The maximum photoresponsivity of 2.2 mA/w has been measured under -1 V bias voltage at 3.8 μm wavelength There are some factors that can be optimised to improve the photoresponsivity of the device, such as optimising waveguide geometry to increase the overlap between the optical mode and graphene, adjusting the separations between the Au electrodes and the Si waveguide, and modifying fabrication processes to have better graphene quality.

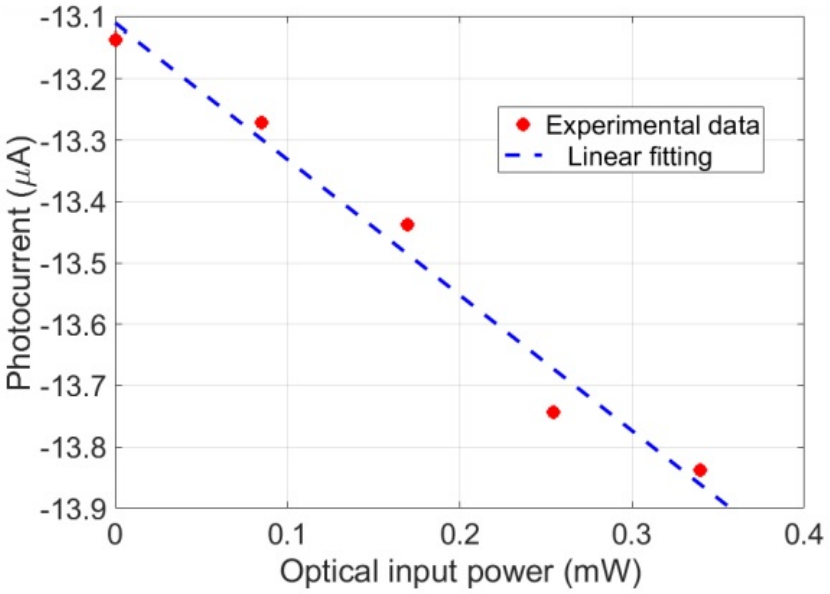

FIGURE A.3: Photocurrent versus optical input power coupled into the detector under -1 V bias voltage. The gradient of the linear fitting curve represents the photoresponsivity of the device, which is 2.2 mA/W at 3.8μm wavelength.

.

Therefore, it should be possible to obtain higher responsivity of the waveguide integrated graphene detectors.

A.1.5 Conclusion

In summary, we have demonstrated the first waveguide integrated graphene photodetector operating at 3.8 μm wavelength. A maximum photoresponsivity of 2.2 mA/W has been observed under -1 V bias voltage. The responsivity can be improved by improved design and fabrication of the detector. There is high potential for the implementation of waveguide integrated graphene photodetectors in the mid-infrared for various applications.

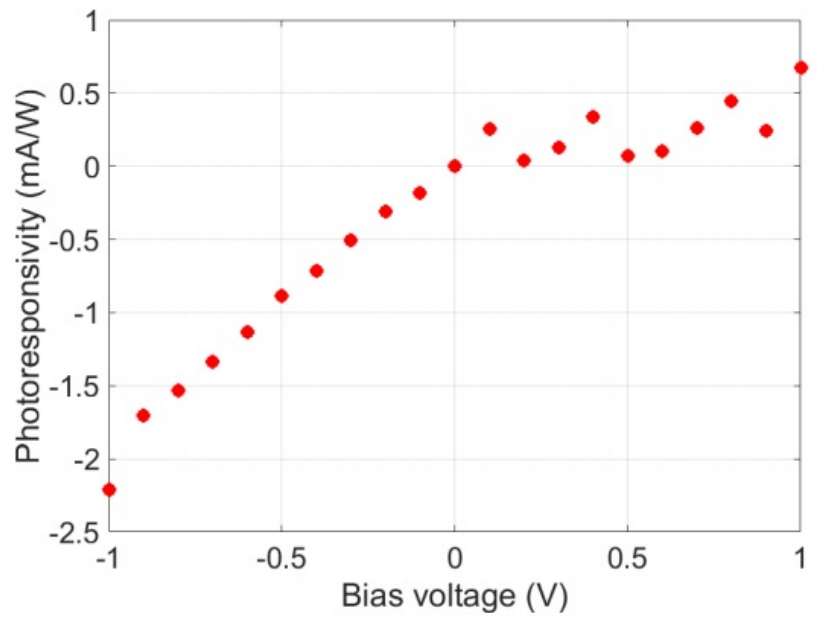

FIGURE A.4: Photoresponsivity versus bias voltage of the graphene photodetector at 3.8 μm wavelength. The highest responsivity appeared at -1 V.

.

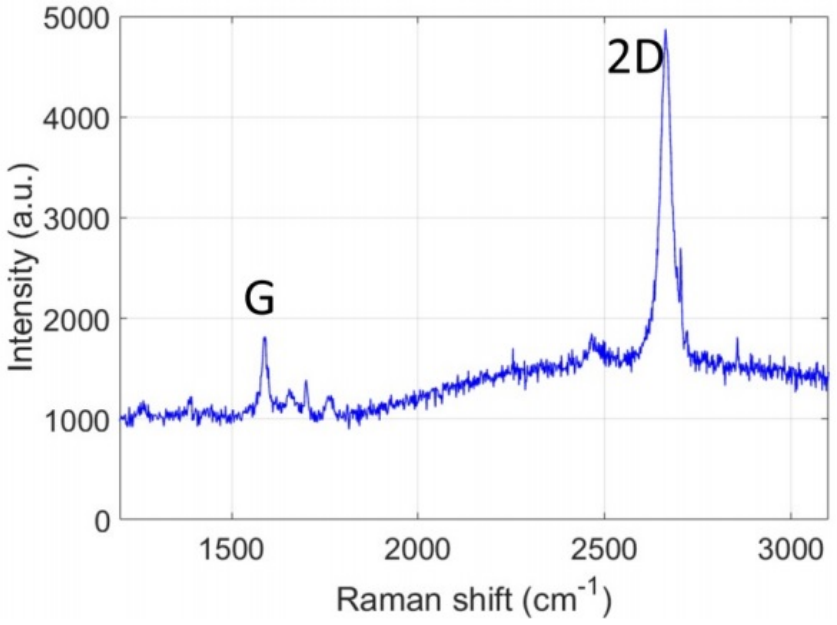

FIGURE A.5: Raman spectrum of transferred graphene on waveguides after metallization. G and 2D peaks show the existence of single layer graphene and defects peaks indicate defects in the graphene structure.

.

A.2 Graphene-Based Fiber Polarizer With PVB-Enhanced Light Interaction

A.2.1 Introduction

Optical polarizers and polarization devices are integral components in both optical communications systems and polarization-dependent optical sensors. Conventional polarizers typically use bulk optical configurations which are difficult to align and interface with fiber networks. Thus efficient, low loss, all-fiber-based polarization components are highly desirable for seamless integration within existing systems. One method of constructing a fiber polarizer is to use an optical fiber with a portion of its cladding removed and replaced with a thin-film overlay. Materials that have been used for this purpose include metal films [185], birefringent crystals [186] and liquid crystals [187]. However, these devices typically have a relatively narrow operation bandwidth, and/or high losses, which limit their application potential. In terms of extending the operation bandwidth, graphene is an excellent choice of material as its linear and gapless band dis-

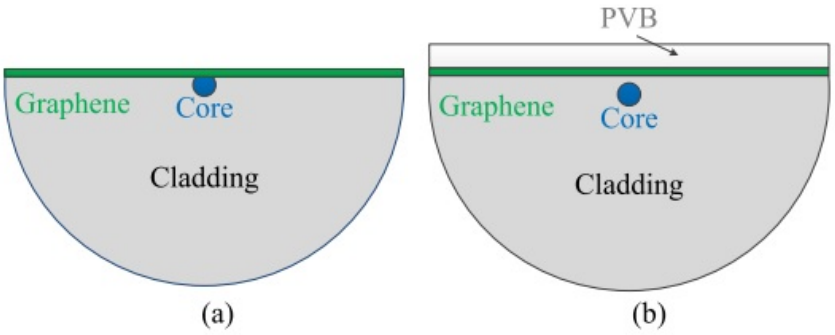

FIGURE A.6: (a)Cross-section of a graphene-based fiber polarizer with sidepolishing into the fiber core, as per [188]. (b) Cross-section of the fiber polarizer used in this study with a residual cladding between the core and the graphene layer.

persion result in flat, broadband absorption and high quantum efficiency [5]. Owing to these desirable optoelectronic properties, graphene has been considered for

a wide array of optical devices, such as all-optical modulators [189], Q-switched or mode-locked ultrafast lasers [190], [191], nonlinear processing [192], and ultra-broadband photodetectors [193]. Of particular relevance to our work, several graphene-based optical polarizers have already been proposed and demonstrated [188] [194], including one device based on a side-polished optical fiber, as shown in Fig. A.6 (a) [188].However, for this particular configuration, in order to achieve a material interaction sufficient for an extinction ratio of 19 dB, the graphene was placed in contact with the core, resulting in impractically high losses (?20 dB at 1550 nm). Other devices such as the planar waveguide-based graphene polarizer proposed in [194], have also exhibited large losses, in this case ?20 dB at 1310 nm [194]. These results make it obvious that an alternative approach is required to obtain both the high performance and low device losses required for fiber-based systems. In this paper, we present a novel approach to producing a low loss, high extinction ratio graphene-based polarizer. The device is based on a modified side-polished fiber design together with a graphene/polymer heterostructure that enhances the light-graphene interaction. The polarizer has an extinction ratio of ?37.5 dB at 1550 nm for a loss of ?1 dB. To our knowledge, this device offers an order of magnitude improvement in performance over any previously reported fiber-based graphene polarizers, while at the same time reducing the device loss by more than two orders of magnitude. The experimental results are in good agreement with the numerical investigations, which highlight the usefulness of these side-polished fibers as templates for the integration of other low-dimensional materials.

A.2.2 Device design

Side-polished optical fibers present a unique opportunity to study the interaction of light and matter in a configuration where

the path of the propagating light is unbroken. As such, the platform has many key benefits such as robustness, long interaction lengths and controllable interaction strengths. The approach developed in this paper is based on a side-polished

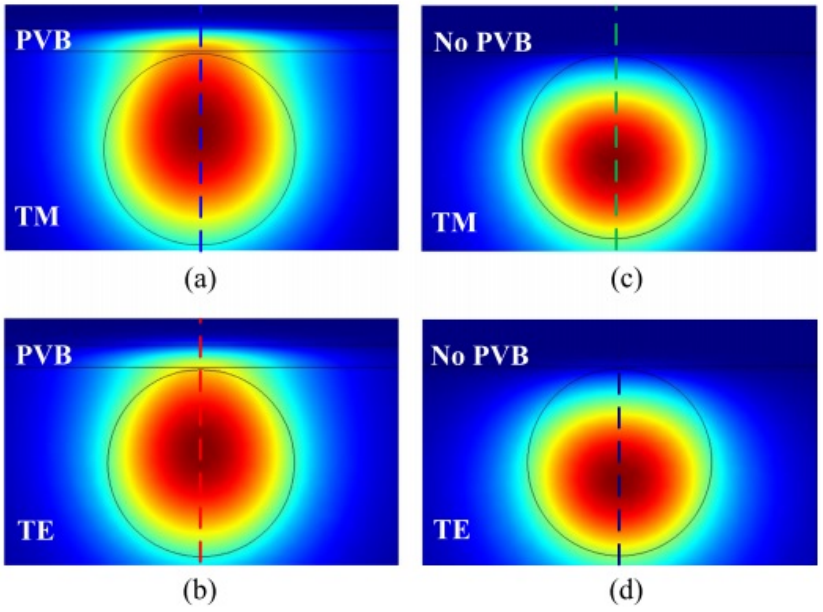

FIGURE A.7: Numerical finite element simulations of modes within the uniform polished sections at 1550 nm. Electric field distributions for (a) TM and (b) TE modes of a side-polished optical fiber with PVB-coated graphene layer, and for (c) TM and (d) TE modes of the same fiber but with graphene only at the polished surface.

.

fiber where the interaction window is polished close to, but not into the core, thus suppressing the transmission losses. However, a drawback of this design is that the field of the core guided mode will be very low at the surface of the window, resulting in a weak interaction with the mono-layer graphene film. To address this issue, we introduce a high index polyvinyl butyral (PVB) over-layer, which helps to draw out the evanescent tail of the propagating core mode and enhance the light-graphene interaction. The longitudinal cross-section of the device is illustrated in Fig. A.6 (b), which clearly shows the three-layer structure. Importantly, as PVB exhibits low optical losses over most of the transmission window of the silica fiber platform, with appropriate design these multi-layer devices could be made to operate from visible wavelengths up to the edge of the mid-infrared. The absorption of graphene arises from the materials intraband and interband transitions, and either can dominate depending on the chemical potential [195]. In our work, we make use of mono-layer graphene prepared by the CVD method, which is estimated to

have a chemical potential on the order of 0.1 eV [196]. Previous work has shown that for potentials of this value, the conductivity of the graphene sheet has a large negative imaginary component [16], so that the interband transition dominates the absorption. Thus we expect the TM mode of the fiber to be preferentially absorbed by the graphene sheet, resulting in a TE-pass polarizer [11]. In order to determine the effect that the PVB layer has on the transmission properties of the device, a numerical finite element study was undertaken. As a starting point, the operation wavelength was set at 1550 nm where the corresponding refractive index of PVB (ng = 1.48) is slightly larger than that of the silica fiber (ns = 1.45). Fig. A.7 (a) and (b) show the electromagnetic field distributions of the fundamental TM and TE modes

at the uniform polished sections of the fiber when coated with a 1 μm thick PVB layer on top of the graphene. For comparison, Fig. A.7 (c) and (d) show the same modes calculated without the PVB layer. These figures clearly illustrate the increased light-matter interaction at the polished fiber surface when the high index layer is included. Further verification is provided by Fig. A.8 (a), which shows the intensity distribution across the positions indicated by the dashed lines in Fig. A.7 . From this figure, we estimate an increase of ?10 dB of modal interaction at the polished surface, which can be attributed to the PVB overlayer. To investigate the influence the layer thickness has on this interaction, Fig. A.8 (b) plots the calculated extinction ratio as a function of wavelength when the PVB thickness varies from 0.6 μm to 1.2 μm in 0.2 μm steps. In general, a thicker PVB layer results in a larger extinction ratio across the wavelength range shown here. However, when the thickness reaches a value of 1.2 μm, the core guided mode becomes leaky for both polarizations. This effect is more distinct at shorter wavelengths and results in a large reduction of extinction ratio. Thus a 1 μm thick PVB layer was deemed to be the optimum choice for this work.

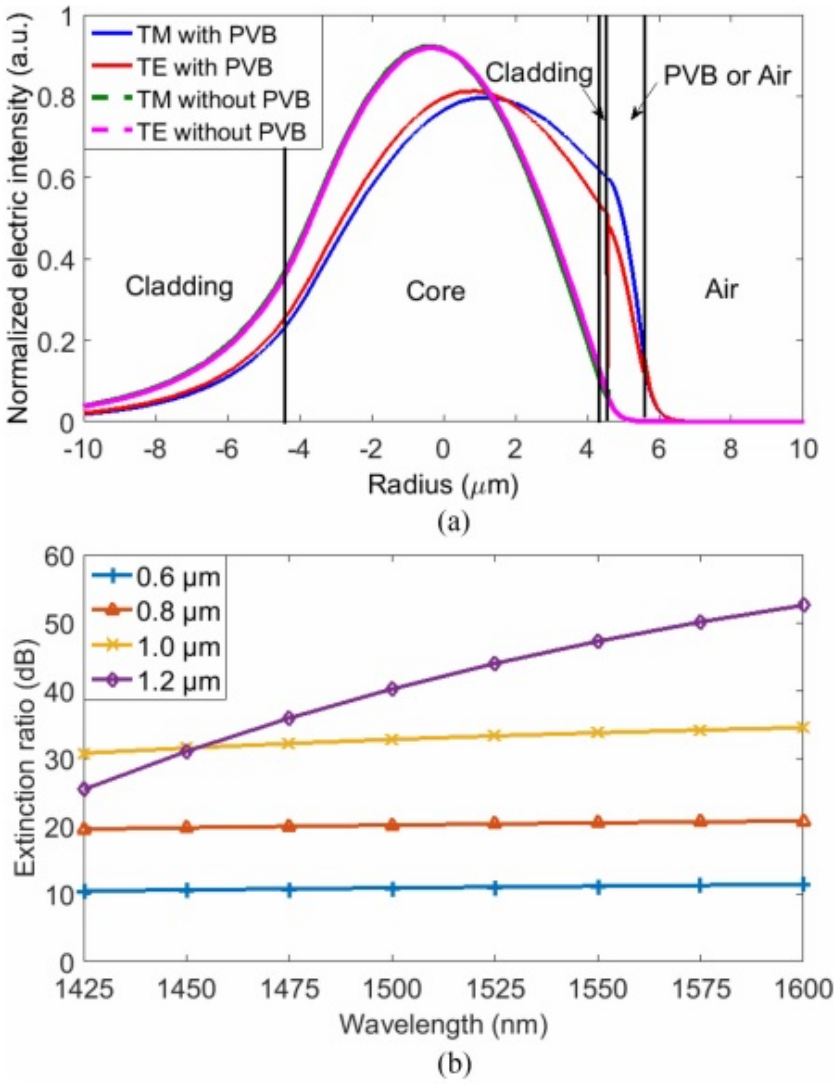

FIGURE A.8: (a) Normalized cross-sectional line scan along dashed lines indicated in Fig. 2. (b) Numerical simulation results showing the extinction ratio as a function of wavelength for different thicknesses of the PVB layer.

.

A.2.3 Fabrication and experiment

To fabricate the side-polished fibers, a modified block polishing technique was used to remove a portion of the cladding from a standard single mode fiber (SMF). The fiber was polished until the planar surface was formed at a distance of 1 μm from the core. The roughness of the polished surface

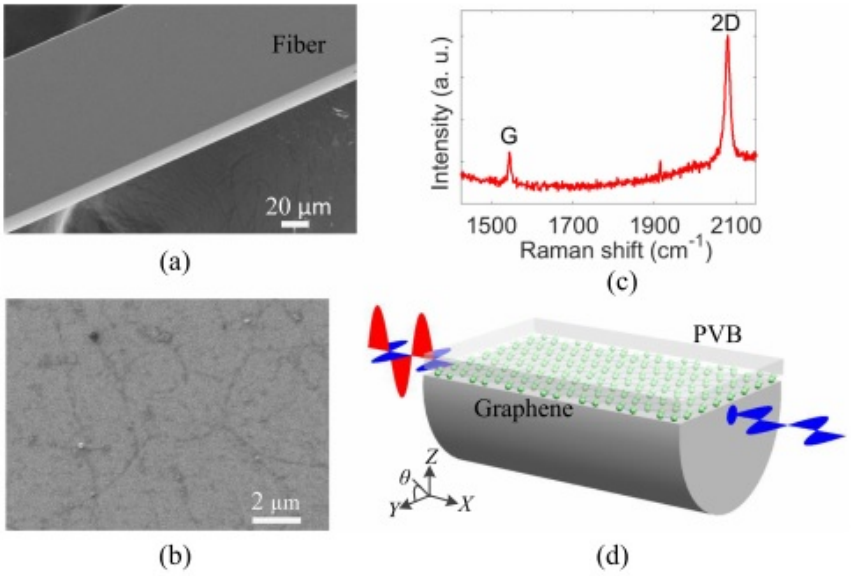

FIGURE A.9: (a) SEM image of our side-polished fiber. (b) Helium-ion microscope image of the graphene sheet and (c) the corresponding Raman spectrum. (d) Schematic model of the PVB-coated graphene polarizer based on a sidepolished optical fiber. Polarization angle is defined as $\theta = 0^0$ and 180^0 for TE mode (blue light wave), $\theta = 90^0$ and 270^0 for TM mode (red light wave).

.

was measured via a ZeScope profilometer to be as low as 1 nm RMS and an adiabatic transition from the fibers full circular geometry to the D-shaped uniform polished region was maintained, resulting in a polished fiber with negligible transmission loss [197]. Fig. A.9 (a) shows a SEM image of the top surface of the side-polished fiber, providing evidence of its ultra smooth surface. The polished region permitted access to more than 30 dB of the light propagating through the core. This was verified by dropping a high refractive index liquid onto the polished region and monitoring the change in transmitted power. The mono-layer graphene film was grown on a copper substrate by a chemical vapor deposition (CVD) method. Fig. A.9 (b) displays a helium-ion microscope image of the CVD grown graphene sheet, which clearly shows its high quality and uniform thickness. Further confirmation of the monolayer nature is provided by the Raman spectrum in Fig. A.9 (c), where the narrow 2D peak (25 cm?1 FWHM) is more than 4 times stronger than the G peak [198]. A 1 μm-thick PVB layer was subsequently spin

coated directly onto the bare graphene surface and baked for 5 min at 85 ?C. The copper substrate was etched away in an ammonium persulfate solution, leaving only the PVB-coated graphene sheet. The sheet was then rinsed in DIwater, before being transferred onto the polished fibers planar surface. Finally, the fiber was baked at 60 ?C for 10 min to thoroughly evaporate the water and improve the contact between the graphene film and the fiber. A schematic view of the resulting device is presented in Fig. A.9 (d). To characterize the optical transmission properties of the PVB-coated graphene-based fiber polarizer, the experimental configuration presented in Fig. A.10 was used. A tunable continuous wave laser (1425 to 1600 nm) was chosen for the signal so that the optical properties could be measured across a broad wavelength range. The signal was free-space coupled into the device using a 10 ? magnification microscope objective lens. Prior to this, polarization control was used to ensure the fidelity of the linear polarization state. The half-wave plate could then

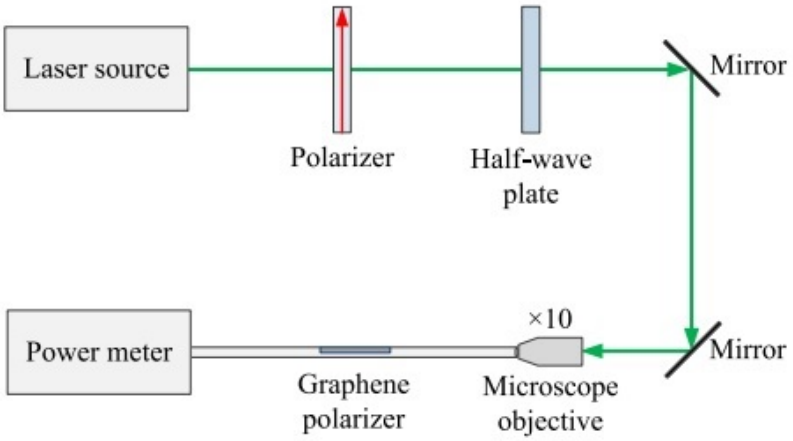

FIGURE A.10: Experimental configuration of the polarization measurements excited by near-infrared light.

.

be used to rotate the polarization of the input light. Since standard SMF fibers are used in this study, the fiber lengths were kept short and the device was maintained as straight as possible to prevent unwanted polarization rotation. The output power was then monitored via a power meter for different polarization angles and

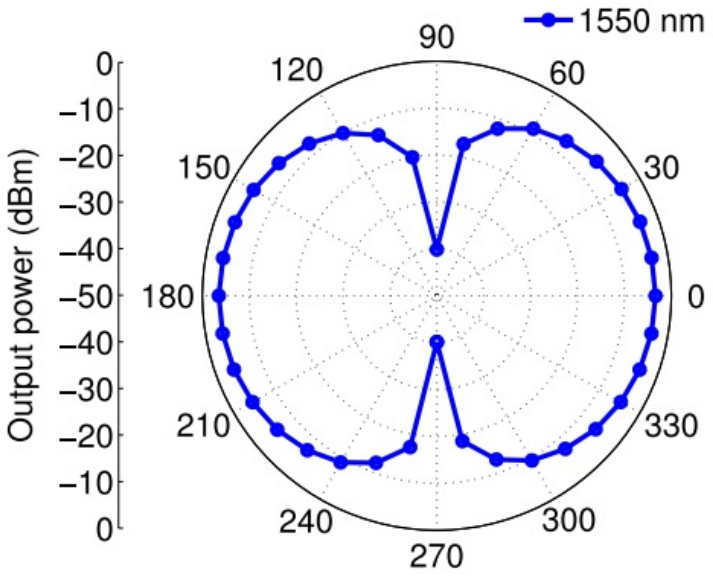

FIGURE A.11: Polar plot of the output power measured at 1550 nm when input power is 0 dBm.

.

wavelengths. An example polar plot of the transmitted power as a function of polarization angle is shown in Fig. A.11, for the wavelength of 1550 nm. It is clear that for the angles of 0? and 180?, when the TE mode was aligned to interact with the graphene, the transmission was maximized and when the polarization was rotated to 90? and 270? the transmission dropped by 37.5 dB, evidence of the TE pass nature of our device. To determine the magnitude of enhancement of the light-graphene interaction due to the PVB, the experiment was repeated on a device with a graphene only layer. In this experiment the extinction ratio was just 3 dB, thus the PVB layer increased the interaction by more that 30 dB in agreement with Fig. A.8 (a).Acontrol experimentwas also performed on a bare side-polished fiber to determine the extent of the polarizing effect of the D-shaped structure. When polished to a distance of 1 μm from the core, the bare fiber showed no evidence of any polarization dependent attenuation. Additional polarization measurements were also undertaken across the full wavelength range of our tunable laser source (1425 to 1600 nm) and at each wavelength, the extinction ratio did not drop below 26 dB (see Fig. A.12). These results also agree

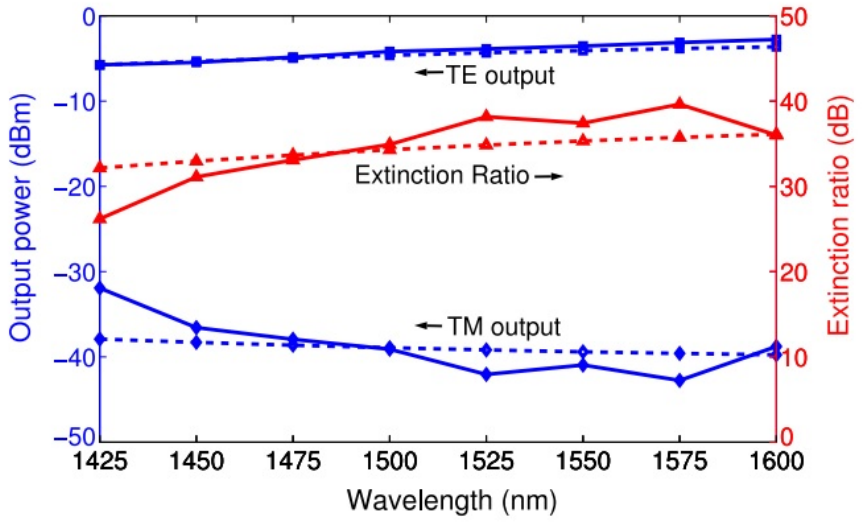

FIGURE A.12: Solid lines: experimental output powers for TE and TM modes and corresponding extinction ratios. Dash lines: predicted extinctions obtained from simulations in Section II.

.

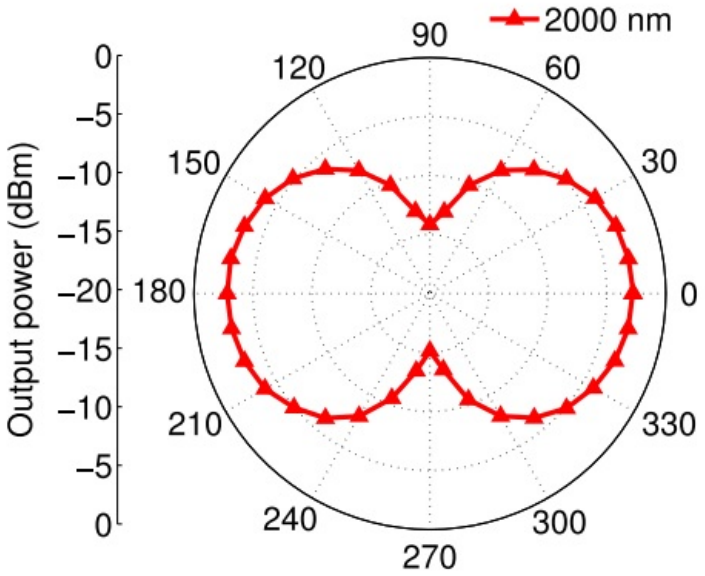

FIGURE A.13: Polar plot of the output power measured at 2000 nm when input power is 0 dBm.

.

well with the theoretical simulation results calculated over this range (dash lines in Fig. A.12), providing clear evidence of the broadband nature of our device and the significant improvement in the performance over previously reported results [188] [194]. Moreover, the polarization extinction ratio increases with larger incidentwavelengths. This is because absorption of theTMlight increases with increasing wavelength, which can be explained by the higher evanescent field of the longer wavelengths at the graphene interface. To provide further evidence of the broadband nature of the device, the measurements were extended to a operating wavelength of 2000 nm using a laser diode. The polar plot in Fig. A.13 shows the result of this experiment with a maximum value of ?3.5 dB and a minimum of ?16.5 dB detected at the output of our device. Comparing this to the results at 1550 nm, we attribute the lower extinction ratio of 13 dB to the limited polarization maintenance of the standard SMF fiber at this longer wavelength. Nevertheless, these results represent the highest extinction ratio measured at 2000 nm for a graphene-based fiber polarizer. Finally, it is also worth noting that as well as enhancing the light-graphene interaction, the PVB film also acts as a protective over-layer to improve the long-term stability of these devices, and no degradation has been observed when monitoring their performance over a 12-month period.

A.2.4 Conclusion

In conclusion, we have designed and experimentally demonstrated a graphene-based fiber polarizer with a high extinction ratio of ?37.5 dB and a low device loss of ?1 dB. Furthermore, an extinction ratio greater than 26 dB was recorded across the wavelength range 14251600 nm, with an additional value of 13 dB at 2000 nm, which confirms the broadband nature of our device. As the reduced extinction at 2000 nm is most likely due to the limited polarizationmaintenance of the SMF at this wavelength, we expect that more optimal fiber designs will enable device operation across the fibres entire single-mode transmission window. We believe that, owing to the combination of low losses and high extinction ratios, this device is the first truly practical graphene-fiber device for photonics applications. This

simple and effective scheme for enhanced light-matter interaction could easily be adapted for other two-dimensional materials such as MoS2 or black phosphors [199], thus serving as a platform for a new generation of all-fiber optoelectronic devices.

Appendix B

List of publications

B.1 Journal publications

- Giant Mechanochromic response of MoS2 based Photonic Metasurface / A. Karvounis, N. Aspiotis, I. Zeimpekis, J.Y. Ou, C. Huang, D. Hewak Paper Submitted, Advanced Science

- Waveguide integrated graphene mid-infrared photodetector. / Qu, Zhibo; Nedeljkovic, Milos; Wu, Yangbo; Soler Penades, Jordi; Khokhar, Ali; Cao, Wei; Osman, Ahmed; Qi, Yanli; Aspiotis, Nikolaos; Morgan, Katrina; Huang, Chung-Che; Mashanovich, Goran. Silicon Photonics XIII. ed. / Graham T. Reed; Andrew P. Knights. Vol. 10537 SPIE, 2018. 105371N (Proceedings of SPIE; Vol. 10537).

- Graphene-based fiber polarizer with PVB-enhanced light interaction. / Zhang, Haojie; Healy, Noel; Shen, Li; Huang, Chung-Che; Aspiotis, Nikolaos; Hewak, Daniel; Peacock, Anna C. In: Journal of Lightwave Technology, 05.06.2016, p. 1-5.

B.2 Conference and meeting contributions

- Aspiotis, Nikolaos, Abbas, Omar, Adnan, Zeimpekis, Ioannis, Mailis, Sakellaris, Sazio, Pier-John, Huang, Chung-Che and Hewak, Daniel (2017) A lift-off method for wafer scale hetero-structuring of 2D materials. EUROMAT 2017: European Congress and Exhibition on Advanced Materials and Processes, Thessaloniki, Greece. 17 - 22 Sep 2017. 1 pp .

- Huang, Chung-Che, Aspiotis, Nikolaos, Cui, Qingsong, Alzaidy, Ghadah, Weatherby, Ed, Craig, Chris, Morgan, Katrina, Zeimpekis, Ioannis and Hewak, Daniel (2017) Chemical vapor deposition and Van der Waals epitaxy for wafer-scale emerging 2D transition metal di-chalcogenides. 2nd International Conference on Physics of 2D Crystals (ICP2C2), Viet Nam. 25 - 30 Apr 2017.

- Huang, Chung-Che, Aspiotis, Nikolaos, Cui, Qingsong, Alzaidy, Ghadah, Abdulrahman, Weatherby, Edwin, Craig, Christopher, Morgan, Katrina, Zeimpekis, Ioannis and Hewak, Daniel (2017) Evolution in emerging 2D functional chalcogenides with CVD and Van der Waals Epitaxy. EMN 2D Materials, Lyon, France. 08 - 12 Aug 2017.

- Zeimpekis, Ioannis, Aspiotis, Nikolaos, Morgan, Katrina, Huang, Chung-Che and Hewak, Daniel (2017) Wafer scale pre-patterned ALD MoS2 FETs. MRS Fall Meeting 2017, Boston, United States. 26 Nov - 01 Dec 2017.

- Aspiotis, Nikolaos, Abbas, Omar, Adnan, Zeimpekis, Ioannis, Mailis, Sakellaris, Sazio, Pier-John, Huang, Chung-Che and Hewak, Daniel (2017) Wafer scale spatially selective transfer of 2D materials and heterostructures. MRS Fall Meeting 2017, Boston, United States. 26 Nov - 01 Dec 2017.

- Morgan, Katrina, Zheng, Xu, Ho, Ying-Lung, Taverne, Mike P.C., Chen, Lifeng, Huang, Chung-Che, Zeimpekis, Ioannis, Aspiotis, Nikos K., Rarity,

John G. and Hewak, Daniel (2016) 3D structures integrated with MoS2. TMD-UK, Bath, United Kingdom. 01 - 02 Sep 2016. 2 pp .

- Huang, Chung-Che, Aspiotis, Nikolaos, Alzaidy, Ghadah, Cui, Qingsong, Weatherby, Ed, Morgan, Katrina and Hewak, Dan (2016) Advanced CVD technology for emerging transition metal di-chalcogenides. Workshop on Two-Dimensional Transition Metal Dichalcogenides Materials and Photovoltaic Devices, Brazil. 29 - 31 Mar 2016.

- Huang, Chung-Che, Alzaidy, Ghadah, Aspiotis, Nikolaos, Cui, Qingsong, Weatherby, Ed, Craig, Chris, Morgan, Katrina, Zeimpekis, Ioannis and Hewak, Daniel (2016) Emerging CVD technology for functional chalcogenide materials. Vacuum Symposium: Functional Thin Films, United Kingdom. 12 - 13 Oct 2016.

- Aspiotis, Nikolaos, Zeimpekis, Ioannis, Morgan, Katrina, Alzaidy, Ghadah, Abdulrahman, Huang, Chung-Che and Hewak, Daniel (2016) Large scale CVD 2D heterostructures. TMD-UK, Bath, United Kingdom. 01 - 02 Sep 2016.

- Huang, C., Alzaidy, Ghadah A., Aspiotis, Nikolaos, Weatherby, Ed C., Wang, Shuncai, Walker, John C., Jiang, Zheng and Hewak, Daniel (2015) Fabrication of tin sulphide and emerging transition metal di-chalcogenides by CVD. The 2nd China-United States Symposium on Energy (CUE-2 2015), China. 26 - 28 Jun 2015.

- Huang, C.C., Aspiotis, N. and Hewak, D. (2015) Telecommunications beyond silicon: one atom thick chalcogenide photodiodes. Royal Society Meeting: Communication Networks Beyond the Capacity Crunch Further Discussion, United Kingdom. 13 - 14 May 2015. 1 pp .

- Huang, Chung-Che, Alzaidy, Ghadah, Abdulrahman, Aspiotis, Nikolaos, Weatherby, Edwin and Hewak, Daniel (2015) Wafer-scale CVD process for 2D transition metal di-chalcogenides. NCTU Nobel Lecture Series Technology is Great: Commercial applications of graphene, Hsin-Chu, Taiwan. 21 - 22 Dec 2015.

Bibliography

[1] Lilienfeld Julius Edgar. Method and apparatus for controlling electric currents, January 28 1930. US Patent 1,745,175.

[2] John Bardeen and Walter Hauser Brattain. The transistor, a semi-conductor triode. *Physical Review*, 74(2):230, 1948.

[3] Bernd Hoefflinger. Itrs: The international technology roadmap for semiconductors. In *Chips 2020*, pages 161–174. Springer, 2011.

[4] LD Landau. Zur theorie der phasenumwandlungen ii. *Phys. Z. Sowjetunion*, 11(545):26–35, 1937.

[5] Kostya S Novoselov, Andre K Geim, Sergei V Morozov, D Jiang, Y_ Zhang, Sergey V Dubonos, Irina V Grigorieva, and Alexandr A Firsov. Electric field effect in atomically thin carbon films. *Science*, 306(5696):666–669, 2004.

[6] Qing Hua Wang, Kourosh Kalantar-Zadeh, Andras Kis, Jonathan N Coleman, and Michael S Strano. Electronics and optoelectronics of two-dimensional transition metal dichalcogenides. *Nature nanotechnology*, 7(11): 699, 2012.

[7] Deblina Sarkar, Wei Liu, Xuejun Xie, Aaron C Anselmo, Samir Mitragotri, and Kaustav Banerjee. MoS_2 field-effect transistor for next-generation label-free biosensors. *ACS nano*, 8(4):3992–4003, 2014.

[8] AH Castro Neto, Francisco Guinea, Nuno MR Peres, Kostya S Novoselov, and Andre K Geim. The electronic properties of graphene. *Reviews of modern physics*, 81(1):109, 2009.

[9] M F Craciun, S Russo, M Yamamoto, and S Tarucha. Tuneable electronic properties in graphene. *Nano Today*, 6(1):42–60, 2011.

[10] Andre K Geim and Konstantin S Novoselov. The rise of graphene. *Nature materials*, 6(3):183, 2007.

[11] Andre K Geim and Konstantin S Novoselov. The rise of graphene. In *Nanoscience and Technology: A Collection of Reviews from Nature Journals*, pages 11–19. World Scientific, 2010.

[12] Yuanbo Zhang, Tsung-Ta Tang, Caglar Girit, Zhao Hao, Michael C Martin, Alex Zettl, Michael F Crommie, Y Ron Shen, and Feng Wang. Direct observation of a widely tunable bandgap in bilayer graphene. *Nature*, 459(7248): 820, 2009.

[13] Eduardo V Castro, KS Novoselov, SV Morozov, NMR Peres, JMB Lopes Dos Santos, Johan Nilsson, F Guinea, AK Geim, and AH Castro Neto. Biased bilayer graphene: semiconductor with a gap tunable by the electric field effect. *Physical review letters*, 99(21):216802, 2007.

[14] Ganhua Lu, Kehan Yu, Zhenhai Wen, and Junhong Chen. Semiconducting graphene: converting graphene from semimetal to semiconductor. *Nanoscale*, 5(4):1353–1368, 2013.

[15] Melinda Y Han, Barbaros Özyilmaz, Yuanbo Zhang, and Philip Kim. Energy band-gap engineering of graphene nanoribbons. *Physical review letters*, 98 (20):206805, 2007.

[16] Isaac Childres, Luis A Jauregui, Wonjun Park, Helin Cao, and Yong P Chen. Raman spectroscopy of graphene and related materials. *New developments in photon and materials research*, 1, 2013.

[17] Andrea C Ferrari, JC Meyer, V Scardaci, C Casiraghi, Michele Lazzeri, Francesco Mauri, S Piscanec, Da Jiang, KS Novoselov, S Roth, et al. Raman spectrum of graphene and graphene layers. *Physical review letters*, 97(18): 187401, 2006.

[18] Andrea C Ferrari, JC Meyer, V Scardaci, C Casiraghi, Michele Lazzeri, Francesco Mauri, S Piscanec, Da Jiang, KS Novoselov, S Roth, et al. Raman spectrum of graphene and graphene layers. *Physical review letters*, 97(18): 187401, 2006.

[19] L Gustavo Cançado, A Jorio, EH Martins Ferreira, F Stavale, CA Achete, RB Capaz, MVO Moutinho, A Lombardo, TS Kulmala, and AC Ferrari. Quantifying defects in graphene via raman spectroscopy at different excitation energies. *Nano letters*, 11(8):3190–3196, 2011.

[20] Manish Chhowalla, Hyeon Suk Shin, Goki Eda, Lain-Jong Li, Kian Ping Loh, and Hua Zhang. The chemistry of two-dimensional layered transition metal dichalcogenide nanosheets. *Nature chemistry*, 5(4):263, 2013.

[21] Efrén Navarro-Moratalla, Joshua O Island, Samuel Mañas-Valero, Elena Pinilla-Cienfuegos, Andres Castellanos-Gomez, Jorge Quereda, Gabino Rubio-Bollinger, Luca Chirolli, Jose Angel Silva-Guillén, Nicolás Agraït, et al. Enhanced superconductivity in atomically thin TaS_2. *Nature communications*, 7:11043, 2016.

[22] AH Castro Neto. Charge density wave, superconductivity, and anomalous metallic behavior in 2d transition metal dichalcogenides. *Physical review letters*, 86(19):4382, 2001.

[23] F Jr Di Salvo, DE Moncton, and JV Waszczak. Electronic properties and superlattice formation in the semimetal $TiSe_2$. *Physical Review B*, 14(10): 4321, 1976.

[24] Won Seok Yun, SW Han, Soon Cheol Hong, In Gee Kim, and JD Lee. Thickness and strain effects on electronic structures of transition metal dichalcogenides: 2H-MX_2 semiconductors (M = Mo, W; X = S, Se, Te). *Physical Review B*, 85(3):033305, 2012.

[25] Andrea Splendiani, Liang Sun, Yuanbo Zhang, Tianshu Li, Jonghwan Kim, Chi-Yung Chim, Giulia Galli, and Feng Wang. Emerging photoluminescence in monolayer $MoS_2$2. *Nano letters*, 10(4):1271–1275, 2010.

[26] Kin Fai Mak, Changgu Lee, James Hone, Jie Shan, and Tony F Heinz. Atomically thin MoS_2: a new direct-gap semiconductor. *Physical review letters*, 105(13):136805, 2010.

[27] Roscoe G Dickinson and Linus Pauling. The crystal structure of molybdenite. *Journal of the American Chemical Society*, 45(6):1466–1471, 1923.

[28] Xiaoxu Zhao, Shoucong Ning, Wei Fu, Stephen J Pennycook, and Kian Ping Loh. Differentiating polymorphs in molybdenum disulfide via electron microscopy. *Advanced Materials*, page 1802397, 2018.

[29] Intek Song, Chibeom Park, and Hee Cheul Choi. Synthesis and properties of molybdenum disulphide: from bulk to atomic layers. *RSC Advances*, 5 (10):7495–7514, 2015.

[30] K Gołasa, M Grzeszczyk, KP Korona, R Bożek, J Binder, J Szczytko, A Wysmołek, and A Babiński. Optical properties of molybdenum disulfide (MoS_2). *Acta Physica Polonica, A.*, 124(5), 2013.

[31] Hong Li, Qing Zhang, Chin Chong Ray Yap, Beng Kang Tay, Teo Hang Tong Edwin, Aurelien Olivier, and Dominique Baillargeat. From bulk to monolayer MoS_2: evolution of raman scattering. *Advanced Functional Materials*, 22(7):1385–1390, 2012.

[32] Changgu Lee, Hugen Yan, Louis E Brus, Tony F Heinz, James Hone, and Sunmin Ryu. Anomalous lattice vibrations of single-and few-layer MoS_2. *ACS nano*, 4(5):2695–2700, 2010.

[33] Yifei Yu, Chun Li, Yi Liu, Liqin Su, Yong Zhang, and Linyou Cao. Controlled scalable synthesis of uniform, high-quality monolayer and few-layer MoS_2 films. *Scientific reports*, 3:1866, 2013.

[34] Hong Li, Qing Zhang, Chin Chong Ray Yap, Beng Kang Tay, Teo Hang Tong Edwin, Aurelien Olivier, and Dominique Baillargeat. From bulk to monolayer MoS_2: evolution of raman scattering. *Advanced Functional Materials*, 22(7):1385–1390, 2012.

[35] David Briggs and John T Grant. *Surface analysis by Auger and X-ray photoelectron spectroscopy*. SurfaceSpectra, 2012.

[36] Stephen McDonnell, Rafik Addou, Creighton Buie, Robert M Wallace, and Christopher L Hinkle. Defect-dominated doping and contact resistance in MoS_2. *ACS nano*, 8(3):2880–2888, 2014.

[37] Sunkook Kim, Aniruddha Konar, Wan-Sik Hwang, Jong Hak Lee, Jiyoul Lee, Jaehyun Yang, Changhoon Jung, Hyoungsub Kim, Ji-Beom Yoo, Jae-Young Choi, et al. High-mobility and low-power thin-film transistors based on multilayer MoS_2 crystals. *Nature communications*, 3:ncomms2018, 2012.

[38] Kristen Kaasbjerg, Kristian S Thygesen, and Karsten W Jacobsen. Phonon-limited mobility in n-type single-layer MoS_2 from first principles. *Physical Review B*, 85(11):115317, 2012.

[39] Nan Ma and Debdeep Jena. Charge scattering and mobility in atomically thin semiconductors. *Physical Review X*, 4(1):011043, 2014.

[40] Amretashis Sengupta, Anuja Chanana, and Santanu Mahapatra. Phonon scattering limited performance of monolayer MoS_2 and WSe_2 n-mosfet. *AIP Advances*, 5(2):027101, 2015.

[41] YI Zhang, Luyao Zhang, and Chongwu Zhou. Review of chemical vapor deposition of graphene and related applications. *Accounts of chemical research*, 46(10):2329–2339, 2013.

[42] Jaeho Jeon, Sung Kyu Jang, Su Min Jeon, Gwangwe Yoo, Yun Hee Jang, Jin-Hong Park, and Sungjoo Lee. Layer-controlled CVD growth of large-area two-dimensional MoS_2 films. *Nanoscale*, 7(5):1688–1695, 2015.

[43] M Syväjärvi and R Yakimova. Quality comparison: Epitaxial graphene vs graphene by CVD. *Linköping, Sweden: Concept Graphene*, 2012.

[44] KS Novoselov and AH Castro Neto. Two-dimensional crystals-based heterostructures: materials with tailored properties. *Physica Scripta*, 2012 (T146):014006, 2012.

[45] Cecilia Mattevi, Hokwon Kim, and Manish Chhowalla. A review of chemical vapour deposition of graphene on copper. *Journal of Materials Chemistry*, 21(10):3324–3334, 2011.

[46] Xiuyun Zhang, Lu Wang, John Xin, Boris I Yakobson, and Feng Ding. Role of hydrogen in graphene chemical vapor deposition growth on a copper surface. *Journal of the American Chemical Society*, 136(8):3040–3047, 2014.

[47] Pierre Trinsoutrot, Caroline Rabot, Hugues Vergnes, Alexandru Delamoreanu, Aziz Zenasni, and Brigitte Caussat. High quality graphene synthesized by atmospheric pressure CVD on copper foil. *Surface and Coatings Technology*, 230:87–92, 2013.

[48] Congqin Miao, Churan Zheng, Owen Liang, and Ya-Hong Xie. Chemical vapor deposition of graphene. In *Physics and applications of graphene-experiments*. IntechOpen, 2011.

[49] Ajjiporn Dathbun and Sutichai Chaisitsak. Effects of three parameters on graphene synthesis by chemical vapor deposition. In *Nano/Micro Engineered and Molecular Systems (NEMS), 2013 8th IEEE International Conference on*, pages 1018–1021. IEEE, 2013.

[50] Maria Losurdo, Maria Michela Giangregorio, Pio Capezzuto, and Giovanni Bruno. Graphene CVD growth on copper and nickel: role of hydrogen in kinetics and structure. *Physical Chemistry Chemical Physics*, 13(46):20836–20843, 2011.

[51] Lin Gan and Zhengtang Luo. Turning off hydrogen to realize seeded growth of subcentimeter single-crystal graphene grains on copper. *Acs Nano*, 7(10): 9480–9488, 2013.

[52] Joshua D Wood, Scott W Schmucker, Austin S Lyons, Eric Pop, and Joseph W Lyding. Effects of polycrystalline cu substrate on graphene growth by chemical vapor deposition. *Nano letters*, 11(11):4547–4554, 2011.

[53] Ivan Vlassiouk, Sergei Smirnov, Murari Regmi, Sumedh P Surwade, Nishtha Srivastava, Randall Feenstra, Gyula Eres, Chad Parish, Nick Lavrik, Panos Datskos, et al. Graphene nucleation density on copper: fundamental role of background pressure. *The Journal of Physical Chemistry C*, 117(37):18919–18926, 2013.

[54] S Kataria, S Wagner, J Ruhkopf, A Gahoi, H Pandey, R Bornemann, Sam Vaziri, Anderson D Smith, M Ostling, and Max C Lemme. Chemical vapor deposited graphene: From synthesis to applications. *physica status solidi (a)*, 211(11):2439–2449, 2014.

[55] Claire Berger, Zhimin Song, Tianbo Li, Xuebin Li, Asmerom Y Ogbazghi, Rui Feng, Zhenting Dai, Alexei N Marchenkov, Edward H Conrad, Phillip N First, et al. Ultrathin epitaxial graphite: 2d electron gas properties and a route toward graphene-based nanoelectronics. *The Journal of Physical Chemistry B*, 108(52):19912–19916, 2004.

[56] Konstantin V Emtsev, Aaron Bostwick, Karsten Horn, Johannes Jobst, Gary L Kellogg, Lothar Ley, Jessica L McChesney, Taisuke Ohta, Sergey A Reshanov, Jonas Röhrl, et al. Towards wafer-size graphene layers by atmospheric pressure graphitization of silicon carbide. *Nature materials*, 8(3):203, 2009.

[57] Taisuke Ohta, Farid El Gabaly, Aaron Bostwick, Jessica L McChesney, Konstantin V Emtsev, Andreas K Schmid, Thomas Seyller, Karsten Horn, and Eli Rotenberg. Morphology of graphene thin film growth on sic (0001). *New Journal of Physics*, 10(2):023034, 2008.

[58] H Hibino, H Kageshima, F Maeda, M Nagase, Y Kobayashi, and H Yamaguchi. Microscopic thickness determination of thin graphite films formed on sic from quantized oscillation in reflectivity of low-energy electrons. *Physical Review B*, 77(7):075413, 2008.

[59] J Hass, R Feng, T Li, X Li, Z Zong, WA De Heer, PN First, EH Conrad, CA Jeffrey, and C Berger. Highly ordered graphene for two dimensional electronics. *Applied Physics Letters*, 89(14):143106, 2006.

[60] Christos Dimitrakopoulos, Yu-Ming Lin, Alfred Grill, Damon B Farmer, Marcus Freitag, Yanning Sun, Shu-Jen Han, Zhihong Chen, Keith A Jenkins, Yu Zhu, et al. Wafer-scale epitaxial graphene growth on the si-face of hexagonal sic (0001) for high frequency transistors. *Journal of Vacuum Science & Technology B, Nanotechnology and Microelectronics: Materials, Processing, Measurement, and Phenomena*, 28(5):985–992, 2010.

[61] https://cordis.europa.eu/docs/projects/cnect/9/257829/080/deliverables/001-conceptgraphened44report.pdf.

[62] BaoShan Hu, ZiDong Wei, Hiroki Ago, Yan Jin, MeiRong Xia, ZhengTang Luo, QingJiang Pan, and YunLing Liu. Effects of substrate and transfer on CVD-grown graphene over sapphire-induced cu films. *Science China Chemistry*, 57(6):895–901, 2014.

[63] Yu Wang, Yi Zheng, Xiangfan Xu, Emilie Dubuisson, Qiaoliang Bao, Jiong Lu, and Kian Ping Loh. Electrochemical delamination of CVD-grown graphene film: toward the recyclable use of copper catalyst. *ACS nano*, 5(12):9927–9933, 2011.

[64] KS Novoselov, D Jiang, F Schedin, TJ Booth, VV Khotkevich, SV Morozov, and AK Geim. Two-dimensional atomic crystals. *Proceedings of the National Academy of Sciences*, 102(30):10451–10453, 2005.

[65] MM Benameur, B Radisavljevic, JS Heron, S Sahoo, H Berger, and A Kis. Visibility of dichalcogenide nanolayers. *Nanotechnology*, 22(12):125706, 2011.

[66] Gábor Zsolt Magda, János Pető, Gergely Dobrik, Chanyong Hwang, László P Biró, and Levente Tapasztó. Exfoliation of large-area transition metal chalcogenide single layers. *Scientific reports*, 5:14714, 2015.

[67] Amit Gupta, Vaishali Arunachalam, and Sukumaran Vasudevan. Liquid-phase exfoliation of MoS_2 nanosheets: the critical role of trace water. *The journal of physical chemistry letters*, 7(23):4884–4890, 2016.

[68] Xiaobin Fan, Pengtao Xu, Dekai Zhou, Yifan Sun, Yuguang C Li, Minh An T Nguyen, Mauricio Terrones, and Thomas E Mallouk. Fast and efficient preparation of exfoliated 2h MoS_2 nanosheets by sonication-assisted lithium intercalation and infrared laser-induced 1t to 2h phase reversion. *Nano letters*, 15(9):5956–5960, 2015.

[69] Na Liu, Paul Kim, Ji Heon Kim, Jun Ho Ye, Sunkook Kim, and Cheol Jin Lee. 28large-area atomically thin MoS_2 nanosheets prepared using electrochemical exfoliation. *ACS nano*, 8(7):6902–6910, 2014.

[70] Branimir Radisavljevic, Aleksandra Radenovic, Jacopo Brivio, i V Giacometti, and A Kis. Single-layer MoS_2 transistors. *Nature nanotechnology*, 6(3):147, 2011.

[71] V Senthilkumar, Le C Tam, Yong Soo Kim, Yumin Sim, Maeng-Je Seong, and Joon I Jang. Direct vapor phase growth process and robust photoluminescence properties of large area MoS_2 layers. *Nano research*, 7(12): 1759–1768, 2014.

[72] Shanshan Wang, Youmin Rong, Ye Fan, Merce Pacios, Harish Bhaskaran, Kuang He, and Jamie H Warner. Shape evolution of monolayer MoS_2 crystals grown by chemical vapor deposition. *Chemistry of Materials*, 26(22):6371–6379, 2014.

[73] SN Heo, Y Ishiguro, R Hayakawa, T Chikyow, and Y Wakayama. Perspective: Highly ordered MoS_2 thin films grown by multi-step chemical vapor deposition process. *APL Materials*, 4(3):030901, 2016.

[74] Sina Najmaei, Zheng Liu, Wu Zhou, Xiaolong Zou, Gang Shi, Sidong Lei, Boris I Yakobson, Juan-Carlos Idrobo, Pulickel M Ajayan, and Jun Lou. Vapour phase growth and grain boundary structure of molybdenum disulphide atomic layers. *Nature materials*, 12(8):754, 2013.

[75] Ifat Jahangir, Goutam Koley, and MVS Chandrashekhar. Back gated fets fabricated by large-area, transfer-free growth of a few layer MoS_2 with high electron mobility. *Applied Physics Letters*, 110(18):182108, 2017.

[76] Qingqing Ji, Yanfeng Zhang, Teng Gao, Yu Zhang, Donglin Ma, Mengxi Liu, Yubin Chen, Xiaofen Qiao, Ping-Heng Tan, Min Kan, et al. Epitaxial monolayer MoS_2 on mica with novel photoluminescence. *Nano letters*, 13 (8):3870–3877, 2013.

[77] Feifei Lan, Zhanping Lai, Yongkuan Xu, Hongjuan Cheng, Zaien Wang, Chengjun Qi, Jianli Chen, and Song Zhang. Synthesis of vertically standing MoS_2 triangles on sic. *Scientific reports*, 6:31980, 2016.

[78] Dmitry Ruzmetov, Kehao Zhang, Gheorghe Stan, Berc Kalanyan, Ganesh R Bhimanapati, Sarah M Eichfeld, Robert A Burke, Pankaj B Shah, Terrance P ORegan, Frank J Crowne, et al. Vertical 2D/3D semiconductor heterostructures based on epitaxial molybdenum disulfide and gallium nitride. *ACS nano*, 10(3):3580–3588, 2016.

[79] Ji Won Suk, Wi Hyoung Lee, Jongho Lee, Harry Chou, Richard D Piner, Yufeng Hao, Deji Akinwande, and Rodney S Ruoff. Enhancement of the electrical properties of graphene grown by chemical vapor deposition via controlling the effects of polymer residue. *Nano letters*, 13(4):1462–1467, 2013.

[80] Hua Yu, Mengzhou Liao, Wenjuan Zhao, Guodong Liu, XJ Zhou, Zheng Wei, Xiaozhi Xu, Kaihui Liu, Zonghai Hu, Ke Deng, et al. Wafer-scale growth and transfer of highly-oriented monolayer MoS_2 continuous films. *ACS nano*, 11(12):12001–12007, 2017.

[81] Donglin Ma, Jianping Shi, Qingqing Ji, Yu Zhang, Mengxi Liu, Qingliang Feng, Xiuju Song, Jin Zhang, Yanfeng Zhang, and Zhongfan Liu. Etching-free transfer of wafer-scale MoS_2 films. *arXiv preprint arXiv:1501.00786*, 2015.

[82] Lu Ma, Digbijoy N Nath, Edwin W Lee, Choong Hee Lee, Mingzhe Yu, Aaron Arehart, Siddharth Rajan, and Yiying Wu. Epitaxial growth of large area single-crystalline few-layer MoS_2 with high space charge mobility of 192 cm^2 V- 1 s- 1. *Applied Physics Letters*, 105(7):072105, 2014.

[83] Yi-Hsien Lee, Xin-Quan Zhang, Wenjing Zhang, Mu-Tung Chang, Cheng-Te Lin, Kai-Di Chang, Ya-Chu Yu, Jacob Tse-Wei Wang, Chia-Seng Chang, Lain-Jong Li, et al. Synthesis of large-area MoS_2 atomic layers with chemical vapor deposition. *Advanced materials*, 24(17):2320–2325, 2012.

[84] Dumitru Dumcenco, Dmitry Ovchinnikov, Kolyo Marinov, Predrag Lazic, Marco Gibertini, Nicola Marzari, Oriol Lopez Sanchez, Yen-Cheng Kung, Daria Krasnozhon, Ming-Wei Chen, et al. Large-area epitaxial monolayer MoS_2. *ACS nano*, 9(4):4611–4620, 2015.

[85] Xi Ling, Yi-Hsien Lee, Yuxuan Lin, Wenjing Fang, Lili Yu, Mildred S Dresselhaus, and Jing Kong. Role of the seeding promoter in MoS_2 growth by chemical vapor deposition. *Nano letters*, 14(2):464–472, 2014.

[86] Xingwang Zhang, Fei Meng, Jeffrey R Christianson, Christian Arroyo-Torres, Mark A Lukowski, Dong Liang, Jordan R Schmidt, and Song Jin. Vertical heterostructures of layered metal chalcogenides by van der waals epitaxy. *Nano letters*, 14(6):3047–3054, 2014.

[87] Yi-Hsien Lee, Lili Yu, Han Wang, Wenjing Fang, Xi Ling, Yumeng Shi, Cheng-Te Lin, Jing-Kai Huang, Mu-Tung Chang, Chia-Seng Chang, et al. Synthesis and transfer of single-layer transition metal disulfides on diverse surfaces. *Nano letters*, 13(4):1852–1857, 2013.

[88] Yi-Hsien Lee, Xin-Quan Zhang, Wenjing Zhang, Mu-Tung Chang, Cheng-Te Lin, Kai-Di Chang, Ya-Chu Yu, Jacob Tse-Wei Wang, Chia-Seng Chang, Lain-Jong Li, et al. Synthesis of large-area MoS_2 atomic layers with chemical vapor deposition. *Advanced materials*, 24(17):2320–2325, 2012.

[89] Chung-Che Huang, Feras Al-Saab, Yudong Wang, Jun-Yu Ou, John C Walker, Shuncai Wang, Behrad Gholipour, Robert E Simpson, and Daniel W

Hewak. Scalable high-mobility MoS_2 thin films fabricated by an atmospheric pressure chemical vapor deposition process at ambient temperature. *Nanoscale*, 6(21):12792–12797, 2014.

[90] Alper Gurarslan, Yifei Yu, Liqin Su, Yiling Yu, Francisco Suarez, Shanshan Yao, Yong Zhu, Mehmet Ozturk, Yong Zhang, and Linyou Cao. Surface-energy-assisted perfect transfer of centimeter-scale monolayer and few-layer MoS_2 films onto arbitrary substrates. *ACS nano*, 8(11):11522–11528, 2014.

[91] Yongji Gong, Junhao Lin, Xingli Wang, Gang Shi, Sidong Lei, Zhong Lin, Xiaolong Zou, Gonglan Ye, Robert Vajtai, Boris I Yakobson, et al. Vertical and in-plane heterostructures from WS_2/MoS_2 monolayers. *Nature materials*, 13(12):1135, 2014.

[92] Vinod K Sangwan, Deep Jariwala, In Soo Kim, Kan-Sheng Chen, Tobin J Marks, Lincoln J Lauhon, and Mark C Hersam. Gate-tunable memristive phenomena mediated by grain boundaries in single-layer MoS_2. *Nature nanotechnology*, 10(5):403, 2015.

[93] Deblina Sarkar, Wei Liu, Xuejun Xie, Aaron C Anselmo, Samir Mitragotri, and Kaustav Banerjee. MoS_2 field-effect transistor for next-generation label-free biosensors. *ACS nano*, 8(4):3992–4003, 2014.

[94] Frank Schwierz. Graphene transistors: status, prospects, and problems. *Proceedings of the IEEE*, 101(7):1567–1584, 2013.

[95] Seyoung Kim, Junghyo Nah, Insun Jo, Davood Shahrjerdi, Luigi Colombo, Zhen Yao, Emanuel Tutuc, and Sanjay K Banerjee. Realization of a high mobility dual-gated graphene field-effect transistor with Al_2O_3 dielectric. *Applied Physics Letters*, 94(6):062107, 2009.

[96] Aniruddha Konar, Tian Fang, and Debdeep Jena. Effect of high-κ gate dielectrics on charge transport in graphene-based field effect transistors. *Physical Review B*, 82(11):115452, 2010.

[97] Xinran Wang, Xiaolin Li, Li Zhang, Youngki Yoon, Peter K Weber, Hailiang Wang, Jing Guo, and Hongjie Dai. N-doping of graphene through electrothermal reactions with ammonia. *Science*, 324(5928):768–771, 2009.

[98] Noejung Park, Bum-Kyu Kim, Jeong-O Lee, and Ju-Jin Kim. Influence of metal work function on the position of the dirac point of graphene field-effect transistors. *Applied Physics Letters*, 95(24):243105, 2009.

[99] Jakub Kedzierski, Pei-Lan Hsu, Alfonso Reina, Jing Kong, Paul Healey, Peter Wyatt, and Craig Keast. Graphene-on-insulator transistors made using C on Ni chemical-vapor deposition. *IEEE Electron Device Letters*, 30(7): 745–747, 2009.

[100] Branimir Radisavljevic and Andras Kis. Mobility engineering and a metal insulator transition in monolayer MoS_2. *Nature materials*, 12(9):815, 2013.

[101] Seung Su Baik, Seongil Im, and Hyoung Joon Choi. Work function tuning in two-dimensional MoS_2 field-effect-transistors with graphene and titanium source-drain contacts. *Scientific reports*, 7:45546, 2017.

[102] Stephen McDonnell, Christopher Smyth, Christopher L Hinkle, and Robert M Wallace. MoS_2 - titanium contact interface reactions. *ACS applied materials & interfaces*, 8(12):8289–8294, 2016.

[103] Adam T Neal, Han Liu, JJ Gu, and PD Ye. Metal contacts to MoS_2: A two-dimensional semiconductor. In *Device Research Conference (DRC), 2012 70th Annual*, pages 65–66. IEEE, 2012.

[104] Saptarshi Das, Hong-Yan Chen, Ashish Verma Penumatcha, and Joerg Appenzeller. High performance multilayer MoS_2 transistors with scandium contacts. *Nano letters*, 13(1):100–105, 2012.

[105] Sunkook Kim, Aniruddha Konar, Wan-Sik Hwang, Jong Hak Lee, Jiyoul Lee, Jaehyun Yang, Changhoon Jung, Hyoungsub Kim, Ji-Beom Yoo, Jae-Young Choi, et al. High-mobility and low-power thin-film transistors based on multilayer MoS_2 crystals. *Nature communications*, 3:ncomms2018, 2012.

[106] Youngchan Kim, Hunyoung Bark, Gyeong Hee Ryu, Zonghoon Lee, and Changgu Lee. Wafer-scale monolayer mos2 grown by chemical vapor deposition using a reaction of moo3 and h2s. *Journal of Physics: Condensed Matter*, 28(18):184002, 2016.

[107] Yongjie Zhan, Zheng Liu, Sina Najmaei, Pulickel M Ajayan, and Jun Lou. Large-area vapor-phase growth and characterization of mos2 atomic layers on a sio2 substrate. *Small*, 8(7):966–971, 2012.

[108] John Robertson, Xue Liu, Chunlei Yue, Matthew Escarra, and Jiang Wei. Wafer-scale synthesis of monolayer and few-layer mos2 via thermal vapor sulfurization. *2D Materials*, 4(4):045007, 2017.

[109] Yu-Chuan Lin, Wenjing Zhang, Jing-Kai Huang, Keng-Ku Liu, Yi-Hsien Lee, Chi-Te Liang, Chih-Wei Chu, and Lain-Jong Li. Wafer-scale mos 2 thin layers prepared by moo 3 sulfurization. *Nanoscale*, 4(20):6637–6641, 2012.

[110] Tianbao Zhang, Yang Wang, Jing Xu, Lin Chen, Hao Zhu, Qingqing Sun, Shijin Ding, and David Wei Zhang. High performance few-layer mos2 transistor arrays with wafer level homogeneity integrated by atomic layer deposition. *2D Materials*, 5(1):015028, 2017.

[111] Wenxu Zhang, Zhishuo Huang, Wanli Zhang, and Yanrong Li. Two-dimensional semiconductors with possible high room temperature mobility. *Nano Research*, 7(12):1731–1737, 2014.

[112] Sohail Ahmed and Jiabao Yi. Two-dimensional transition metal dichalcogenides and their charge carrier mobilities in field-effect transistors. *Nano-micro letters*, 9(4):50, 2017.

[113] Mei Zhang, Yiming Zhu, Xinsheng Wang, Qingliang Feng, Shanlin Qiao, Wen Wen, Yanfeng Chen, Menghua Cui, Jin Zhang, Congzhong Cai, et al. Controlled synthesis of ZrS_2 monolayer and few layers on hexagonal boron nitride. *Journal of the American Chemical Society*, 137(22):7051–7054, 2015.

[114] Ruoyu Yue, Adam T Barton, Hui Zhu, Angelica Azcatl, Luis F Pena, Jian Wang, Xin Peng, Ning Lu, Lanxia Cheng, Rafik Addou, et al. $HfSe_2$ thin films: 2d transition metal dichalcogenides grown by molecular beam epitaxy. *ACS nano*, 9(1):474–480, 2014.

[115] C Kreis, S Werth, R Adelung, L Kipp, M Skibowski, EE Krasovskii, and W Schattke. Valence and conduction band states of HfS_2: From bulk to a single layer. *Physical Review B*, 68(23):235331, 2003.

[116] Kai Xu, Zhenxing Wang, Feng Wang, Yun Huang, Fengmei Wang, Lei Yin, Chao Jiang, and Jun He. Ultrasensitive phototransistors based on few-layered HfS_2. *Advanced Materials*, 27(47):7881–7887, 2015.

[117] Larbi Roubi and Cosmo Carlone. Resonance raman spectrum of HfS_2 and ZrS_2. *Physical Review B*, 37(12):6808, 1988.

[118] A Cingolani, M Lugarà, and F Lévy. Resonance raman scattering in $HfSe_2$ and HfS_2. *Physica Scripta*, 37(3):389, 1988.

[119] Leo Brewer and RH Lamoreaux. The Mo-S system (molybdenum-sulfur). *Bulletin of alloy phase diagrams*, 1(2):93–95, 1980.

[120] Gwan-Hyoung Lee, Young-Jun Yu, Xu Cui, Nicholas Petrone, Chul-Ho Lee, Min Sup Choi, Dae-Yeong Lee, Changgu Lee, Won Jong Yoo, Kenji Watanabe, et al. Flexible and transparent MoS_2 field-effect transistors on hexagonal boron nitride-graphene heterostructures. *ACS nano*, 7(9):7931–7936, 2013.

[121] Hai Hu, Feng Zhai, Debo Hu, Zhenjun Li, Bing Bai, Xiaoxia Yang, and Qing Dai. Broadly tunable graphene plasmons using an ion-gel top gate with low control voltage. *Nanoscale*, 7(46):19493–19500, 2015.

[122] Mikai Chen, Hongsuk Nam, Sungjin Wi, Greg Priessnitz, Ivan Manuel Gunawan, and Xiaogan Liang. Multibit data storage states formed in plasma-treated MoS_2 transistors. *Acs Nano*, 8(4):4023–4032, 2014.

[123] Jun-Yu Ou, Eric Plum, Liudi Jiang, and Nikolay I Zheludev. Reconfigurable photonic metamaterials. *Nano letters*, 11(5):2142–2144, 2011.

[124] Artemios Karvounis, Jun-Yu Ou, Weiping Wu, Kevin F MacDonald, and Nikolay I Zheludev. Nano-optomechanical nonlinear dielectric metamaterials. *Applied Physics Letters*, 107(19):191110, 2015.

[125] Adeel Afridi, Josep Canet-Ferrer, Laurent Philippet, Johann Osmond, Pascal Berto, and Romain Quidant. Electrically driven varifocal silicon metalens. *ACS Photonics*, 5(11):4497–4503, 2018.

[126] Tom Driscoll, Hyun-Tak Kim, Byung-Gyu Chae, Bong-Jun Kim, Yong-Wook Lee, N Marie Jokerst, Sabarni Palit, David R Smith, Massimiliano Di Ventra, and Dimitri N Basov. Memory metamaterials. *Science*, 325 (5947):1518–1521, 2009.

[127] Andreas Tittl, Ann-Katrin U Michel, Martin Schäferling, Xinghui Yin, Behrad Gholipour, Long Cui, Matthias Wuttig, Thomas Taubner, Frank Neubrech, and Harald Giessen. A switchable mid-infrared plasmonic perfect absorber with multispectral thermal imaging capability. *Advanced Materials*, 27(31):4597–4603, 2015.

[128] Artemios Karvounis, Behrad Gholipour, Kevin F MacDonald, and Nikolay I Zheludev. All-dielectric phase-change reconfigurable metasurface. *Applied Physics Letters*, 109(5):051103, 2016.

[129] Qian Wang, Edward TF Rogers, Behrad Gholipour, Chih-Ming Wang, Guanghui Yuan, Jinghua Teng, and Nikolay I Zheludev. Optically reconfigurable metasurfaces and photonic devices based on phase change materials. *Nature Photonics*, 10(1):60, 2016.

[130] Keshav M Dani, Zahyun Ku, Prashanth C Upadhya, Rohit P Prasankumar, SRJ Brueck, and Antoinette J Taylor. Subpicosecond optical switching with a negative index metamaterial. *Nano letters*, 9(10):3565–3569, 2009.

[131] Mengxin Ren, Baohua Jia, Jun-Yu Ou, Eric Plum, Jianfa Zhang, Kevin F MacDonald, Andrey E Nikolaenko, Jingjun Xu, Min Gu, and Nikolay I Zheludev. Nanostructured plasmonic medium for terahertz bandwidth all-optical switching. *Advanced Materials*, 23(46):5540–5544, 2011.

[132] Yao-Wei Huang, Ho Wai Howard Lee, Ruzan Sokhoyan, Ragip A Pala, Krishnan Thyagarajan, Seunghoon Han, Din Ping Tsai, and Harry A Atwater. Gate-tunable conducting oxide metasurfaces. *Nano letters*, 16(9):5319–5325, 2016.

[133] Matthew Morea, Kai Zang, Theodore I Kamins, Mark L Brongersma, and James S Harris. Electrically tunable, CMOS-compatible metamaterial based on semiconductor nanopillars. *ACS Photonics*, 5(11):4702–4709, 2018.

[134] Alexander Minovich, James Farnell, Dragomir N Neshev, Ian McKerracher, Fouad Karouta, Jie Tian, David A Powell, Ilya V Shadrivov, Hark Hoe Tan, Chennupati Jagadish, et al. Liquid crystal based nonlinear fishnet metamaterials. *Applied Physics Letters*, 100(12):121113, 2012.

[135] O Buchnev, JY Ou, M Kaczmarek, NI Zheludev, and VA Fedotov. Electro-optical control in a plasmonic metamaterial hybridised with a liquid-crystal cell. *Optics express*, 21(2):1633–1638, 2013.

[136] Florian Sterl, Nikolai Strohfeldt, Ramon Walter, Ronald Griessen, Andreas Tittl, and Harald Giessen. Magnesium as novel material for active plasmonics in the visible wavelength range. *Nano letters*, 15(12):7949–7955, 2015.

[137] Imogen M Pryce, Koray Aydin, Yousif A Kelaita, Ryan M Briggs, and Harry A Atwater. Highly strained compliant optical metamaterials with large frequency tunability. *Nano letters*, 10(10):4222–4227, 2010.

[138] Philipp Gutruf, Chengjun Zou, Withawat Withayachumnankul, Madhu Bhaskaran, Sharath Sriram, and Christophe Fumeaux. Mechanically tunable dielectric resonator metasurfaces at visible frequencies. *ACS nano*, 10 (1):133–141, 2015.

[139] Martin K Beyer and Hauke Clausen-Schaumann. Mechanochemistry: the mechanical activation of covalent bonds. *Chemical Reviews*, 105(8):2921–2948, 2005.

[140] Xiqi Zhang, Zhenguo Chi, Yi Zhang, Siwei Liu, and Jiarui Xu. Recent advances in mechanochromic luminescent metal complexes. *Journal of Materials Chemistry C*, 1(21):3376–3390, 2013.

[141] Brent R Crenshaw and Christoph Weder. Deformation-induced color changes in melt-processed photoluminescent polymer blends. *Chemistry of materials*, 15(25):4717–4724, 2003.

[142] Elaine Lee, Milin Zhang, Yigil Cho, Yue Cui, Jan Van der Spiegel, Nader Engheta, and Shu Yang. Tilted pillars on wrinkled elastomers as a reversibly tunable optical window. *Advanced Materials*, 26(24):4127–4133, 2014.

[143] Yuan Zhuang, Fei Yu, Hong Chen, Jie Zheng, Jie Ma, and Junhong Chen. Alginate/graphene double-network nanocomposite hydrogel beads with low-swelling, enhanced mechanical properties, and enhanced adsorption capacity. *Journal of Materials Chemistry A*, 4(28):10885–10892, 2016.

[144] Maximilian Raisch, Damiano Genovese, Nelsi Zaccheroni, Simon B Schmidt, Maria Letizia Focarete, Michael Sommer, and Chiara Gualandi. Highly sensitive, anisotropic, and reversible stress/strain-sensors from mechanochromic nanofiber composites. *Advanced Materials*, 30(39):1802813, 2018.

[145] Edwin P Chan, Joseph J Walish, Augustine M Urbas, and Edwin L Thomas. Mechanochromic photonic gels. *Advanced Materials*, 25(29):3934–3947, 2013.

[146] Kai Sun, Christoph A Riedel, Alessandro Urbani, Mirko Simeoni, Sandro Mengali, Maksim Zalkovskij, Brian Bilenberg, CH De Groot, and Otto L Muskens. VO_2 thermochromic metamaterial-based smart optical solar reflector. *ACS Photonics*, 5(6):2280–2286, 2018.

[147] Grant J Stec, Adam Lauchner, Yao Cui, Peter Nordlander, and Naomi J Halas. Multicolor electrochromic devices based on molecular plasmonics. *ACS nano*, 11(3):3254–3261, 2017.

[148] Andres Castellanos-Gomez, Rafael Roldán, Emmanuele Cappelluti, Michele Buscema, Francisco Guinea, Herre SJ van der Zant, and Gary A Steele. Local strain engineering in atomically thin MoS_2. *Nano letters*, 13(11):5361–5366, 2013.

[149] Qinglei Guo, Zengfeng Di, Max G Lagally, and Yongfeng Mei. Strain engineering and mechanical assembly of silicon/germanium nanomembranes. *Materials Science and Engineering: R: Reports*, 128:1–31, 2018.

[150] Gururaj V Naik, Vladimir M Shalaev, and Alexandra Boltasseva. Alternative plasmonic materials: beyond gold and silver. *Advanced Materials*, 25 (24):3264–3294, 2013.

[151] Yafei Li, Zhen Zhou, Shengbai Zhang, and Zhongfang Chen. MoS_2 nanoribbons: high stability and unusual electronic and magnetic properties. *Journal of the American Chemical Society*, 130(49):16739–16744, 2008.

[152] Liangzhi Kou, Chun Tang, Yi Zhang, Thomas Heine, Changfeng Chen, and Thomas Frauenheim. Tuning magnetism and electronic phase transitions by strain and electric field in zigzag MoS_2 nanoribbons. *The journal of physical chemistry letters*, 3(20):2934–2941, 2012.

[153] Priya Johari and Vivek B Shenoy. Tuning the electronic properties of semiconducting transition metal dichalcogenides by applying mechanical strains. *ACS nano*, 6(6):5449–5456, 2012.

[154] Hartwin Peelaers and Chris G Van de Walle. Effects of strain on band structure and effective masses in MoS_2. *Physical Review B*, 86(24):241401, 2012.

[155] Lei Yang, Xudong Cui, Jingyu Zhang, Kan Wang, Meng Shen, Shuangshuang Zeng, Shadi A Dayeh, Liang Feng, and Bin Xiang. Lattice strain effects on the optical properties of MoS_2 nanosheets. *Scientific reports*, 4: 5649, 2014.

[156] Fariba Kafi, Raheleh Pilevar Shahri, Mohammad Reza Benam, and Arsalan Akhtar. Tuning optical properties of MoS_2 bulk and monolayer under compressive and tensile strain: a first principles study. *Journal of Electronic Materials*, 46(10):6158–6166, 2017.

[157] Andres Castellanos-Gomez, Menno Poot, Gary A Steele, Herre SJ van der Zant, Nicolás Agraït, and Gabino Rubio-Bollinger. Elastic properties of freely suspended MoS_2 nanosheets. *Advanced Materials*, 24(6):772–775, 2012.

[158] Martin Dieterle, Gisela Weinberg, and Gerhard Mestl. Raman spectroscopy of molybdenum oxides part i. structural characterization of oxygen defects in MoO_3- x by dr UV/VIS, raman spectroscopy and x-ray diffraction. *Physical Chemistry Chemical Physics*, 4(5):812–821, 2002.

[159] Behrad Gholipour, Giorgio Adamo, Daniele Cortecchia, Harish NS Krishnamoorthy, Muhammad D Birowosuto, Nikolay I Zheludev, and Cesare Soci. Organometallic perovskite metasurfaces. *Advanced Materials*, 29(9):1604268, 2017.

[160] Behrad Gholipour, Davide Piccinotti, Artemios Karvounis, Kevin F MacDonald, and Nikolay I Zheludev. Reconfigurable ultraviolet and high-energy-visible dielectric metamaterials. *Nano letters*, 2019.

[161] SK Deb. Physical properties of a transition metal oxide: optical and photoelectric properties of single crystal and thin film molybdenum trioxide. *Proceedings of the Royal Society of London. Series A. Mathematical and Physical Sciences*, 304(1477):211–231, 1968.

[162] Yong-Nian Xu and WY Ching. Electronic structure and properties of a and b phases of silicon nitride silicon oxynitride and with comparison to silicon dioxide. *Physical Review e*, 51(24):379–389, 1995.

[163] Wei-Qing Yang, Zhao-Rong Wei, Xing-Hua Zhu, and Ding-Ying Yang. Strong influence of substrate temperature on the growth of nanocrystalline MoO_3 thin films. *Physics Letters A*, 373(43):3965–3968, 2009.

[164] Joao Valente, Jun-Yu Ou, Eric Plum, Ian J Youngs, and Nikolay I Zheludev. A magneto-electro-optical effect in a plasmonic nanowire material. *Nature communications*, 6:7021, 2015.

[165] Yusuke Nagasaki, Behrad Gholipour, Jun-Yu Ou, Masanori Tsuruta, Eric Plum, Kevin F MacDonald, Junichi Takahara, and Nikolay I Zheludev. Optical bistability in shape-memory nanowire metamaterial array. *Applied Physics Letters*, 113(2):021105, 2018.

[166] Richard Soref. Mid-infrared photonics in silicon and germanium. *Nature photonics*, 4(8):495, 2010.

[167] Goran Z Mashanovich, Frederic Y Gardes, David J Thomson, Youfang Hu, Ke Li, Milos Nedeljkovic, Jordi Soler Penades, Ali Z Khokhar, Colin J Mitchell, Stevan Stankovic, et al. Silicon photonic waveguides and devices for near-and mid-ir applications. *IEEE Journal of Selected Topics in Quantum Electronics*, 21(4):407–418, 2015.

[168] Kin Fai Mak, Long Ju, Feng Wang, and Tony F Heinz. Optical spectroscopy of graphene: from the far infrared to the ultraviolet. *Solid State Communications*, 152(15):1341–1349, 2012.

[169] FHL Koppens, T Mueller, Ph Avouris, AC Ferrari, MS Vitiello, and M Polini. Photodetectors based on graphene, other two-dimensional materials and hybrid systems. *Nature nanotechnology*, 9(10):780, 2014.

[170] Fengnian Xia, Han Wang, Di Xiao, Madan Dubey, and Ashwin Ramasubramaniam. Two-dimensional material nanophotonics. *Nature Photonics*, 8 (12):899, 2014.

[171] L Vicarelli, MS Vitiello, D Coquillat, Antonio Lombardo, Andrea Carlo Ferrari, W Knap, M Polini, V Pellegrini, and Alessandro Tredicucci. Graphene field-effect transistors as room-temperature terahertz detectors. *Nature materials*, 11(10):865, 2012.

[172] AB Kuzmenko, Erik Van Heumen, Fabrizio Carbone, and Dirk Van Der Marel. Universal optical conductance of graphite. *Physical review letters*, 100(11):117401, 2008.

[173] ZQ Li, Eric A Henriksen, Z Jiang, Zhao Hao, Michael C Martin, P Kim, HL Stormer, and Dimitri N Basov. Dirac charge dynamics in graphene by infrared spectroscopy. *Nature Physics*, 4(7):532, 2008.

[174] Phaedon Avouris and Marcus Freitag. Graphene photonics, plasmonics, and optoelectronics. *IEEE Journal of selected topics in quantum electronics*, 20 (1):72–83, 2014.

[175] Phaedon Avouris. Graphene: electronic and photonic properties and devices. *Nano letters*, 10(11):4285–4294, 2010.

[176] Kostya S Novoselov, Andre K Geim, Sergei V Morozov, D Jiang, Y_ Zhang, Sergey V Dubonos, Irina V Grigorieva, and Alexandr A Firsov. Electric field effect in atomically thin carbon films. *science*, 306(5696):666–669, 2004.

[177] Xuetao Gan, Ren-Jye Shiue, Yuanda Gao, Inanc Meric, Tony F Heinz, Kenneth Shepard, James Hone, Solomon Assefa, and Dirk Englund. Chip-integrated ultrafast graphene photodetector with high responsivity. *Nature Photonics*, 7(11):883, 2013.

[178] Xiaomu Wang, Zhenzhou Cheng, Ke Xu, Hon Ki Tsang, and Jian-Bin Xu. High-responsivity graphene/silicon-heterostructure waveguide photodetectors. *Nature Photonics*, 7(11):888, 2013.

[179] Fengnian Xia, Thomas Mueller, Yu-ming Lin, Alberto Valdes-Garcia, and Phaedon Avouris. Ultrafast graphene photodetector. *Nature nanotechnology*, 4(12):839, 2009.

[180] Michael Engel, Mathias Steiner, Antonio Lombardo, Andrea C Ferrari, Hilbert v Löhneysen, Phaedon Avouris, and Ralph Krupke. Light–matter interaction in a microcavity-controlled graphene transistor. *Nature communications*, 3:906, 2012.

[181] Zheyu Fang, Zheng Liu, Yumin Wang, Pulickel M Ajayan, Peter Nordlander, and Naomi J Halas. Graphene-antenna sandwich photodetector. *Nano letters*, 12(7):3808–3813, 2012.

[182] TJ Echtermeyer, L Britnell, PK Jasnos, Antonio Lombardo, RV Gorbachev, AN Grigorenko, AK Geim, Andrea Carlo Ferrari, and KS Novoselov. Strong plasmonic enhancement of photovoltage in graphene. *Nature communications*, 2:458, 2011.

[183] Steven J Koester and Mo Li. Waveguide-coupled graphene optoelectronics. *IEEE Journal of Selected Topics in Quantum Electronics*, 20(1):84–94, 2014.

[184] Ilya Goykhman, Ugo Sassi, Boris Desiatov, Noa Mazurski, Silvia Milana, Domenico de Fazio, Anna Eiden, Jacob Khurgin, Joseph Shappir, Uriel Levy, et al. On-chip integrated, silicon–graphene plasmonic schottky photodetector with high responsivity and avalanche photogain. *Nano letters*, 16(5):3005–3013, 2016.

[185] JR Feth and CL Chang. Metal-clad fiber-optic cutoff polarizer. *Optics letters*, 11(6):386–388, 1986.

[186] Ralph A Bergh, Herbert C Lefevre, and Herbert J Shaw. Single-mode fiber-optic polarizer. *Optics Letters*, 5(11):479–481, 1980.

[187] K Liu, WV Sorin, and HJ Shaw. Single-mode-fiber evanescent polarizer/amplitude modulator using liquid crystals. *Optics letters*, 11(3):180–182, 1986.

[188] Qiaoliang Bao, Han Zhang, Bing Wang, Zhenhua Ni, Candy Haley Yi Xuan Lim, Yu Wang, Ding Yuan Tang, and Kian Ping Loh. Broadband graphene polarizer. *Nature photonics*, 5(7):411, 2011.

[189] Ming Liu, Xiaobo Yin, Erick Ulin-Avila, Baisong Geng, Thomas Zentgraf, Long Ju, Feng Wang, and Xiang Zhang. A graphene-based broadband optical modulator. *Nature*, 474(7349):64, 2011.

[190] Daniel Popa, Z Sun, Tawfique Hasan, Felice Torrisi, F Wang, and Andrea Carlo Ferrari. Graphene Q-switched, tunable fiber laser. *Applied Physics Letters*, 98(7):073106, 2011.

[191] Han Zhang, DY Tang, LM Zhao, QL Bao, and KP Loh. Large energy mode locking of an erbium-doped fiber laser with atomic layer graphene. *Optics Express*, 17(20):17630–17635, 2009.

[192] Han Zhang, Stéphane Virally, Qiaoliang Bao, Loh Kian Ping, Serge Massar, Nicolas Godbout, and Pascal Kockaert. Z-scan measurement of the nonlinear refractive index of graphene. *Optics letters*, 37(11):1856–1858, 2012.

[193] Fengnian Xia, Thomas Mueller, Roksana Golizadeh-Mojarad, Marcus Freitag, Yu-ming Lin, James Tsang, Vasili Perebeinos, and Phaedon Avouris. Photocurrent imaging and efficient photon detection in a graphene transistor. *Nano letters*, 9(3):1039–1044, 2009.

[194] Jin Tae Kim and Choon-Gi Choi. Graphene-based polymer waveguide polarizer. *Optics express*, 20(4):3556–3562, 2012.

[195] Jacek Gosciniak and Dawn TH Tan. Theoretical investigation of graphene-based photonic modulators. *Scientific reports*, 3:1897, 2013.

[196] Jason Horng, Chi-Fan Chen, Baisong Geng, Caglar Girit, Yuanbo Zhang, Zhao Hao, Hans A Bechtel, Michael Martin, Alex Zettl, Michael F Crommie, et al. Drude conductivity of dirac fermions in graphene. *Physical Review B*, 83(16):165113, 2011.

[197] Haojie Zhang, Noel Healy, Li Shen, Chung Che Huang, Daniel W Hewak, and Anna C Peacock. Enhanced all-optical modulation in a graphene-coated fibre with low insertion loss. *Scientific reports*, 6:23512, 2016.

[198] Andrea C Ferrari, JC Meyer, V Scardaci, C Casiraghi, Michele Lazzeri, Francesco Mauri, S Piscanec, Da Jiang, KS Novoselov, S Roth, et al. Raman spectrum of graphene and graphene layers. *Physical review letters*, 97(18): 187401, 2006.

[199] SB Lu, LL Miao, ZN Guo, X Qi, CJ Zhao, H Zhang, SC Wen, DY Tang, and DY Fan. Broadband nonlinear optical response in multi-layer black phosphorus: an emerging infrared and mid-infrared optical material. *Optics express*, 23(9):11183–11194, 2015.